Coordination Chemistry Reviews 367 (2018) 163–216

Contents lists available at ScienceDirect

Coordination Chemistry Reviews

journal homepage: www.elsevier.com/locate/ccr

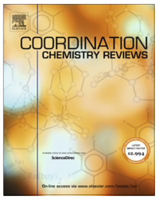

Review

Low-coordinate mononuclear lanthanide complexes as molecular nanomagnets

Arun Kumar Bar [a,*], Pankaj Kalita [a], Mukesh Kumar Singh [b], Gopalan Rajaraman [b,*], Vadapalli Chandrasekhar [c,d,*]

[a] School of Chemical Sciences, National Institute of Science Education and Research, HBNI, Bhubaneswar 752050, India
[b] Department of Chemistry, Indian Institute of Technology Bombay, Powai, Mumbai 400076, India
[c] Department of Chemistry, Indian Institute of Technology Kanpur, Kanpur 208016, India
[d] Tata Institute of Fundamental Research Hyderabad, Gopanpally, Hyderabad 500107, India

ARTICLE INFO

Article history:
Received 21 December 2017
Accepted 28 March 2018
Available online 30 April 2018

ABSTRACT

The discovery that some *bis*-(phthalocyaninato)lanthanide complexes are molecular magnets triggered interest in lanthanide ion complexes. Theoretical and experimental observations have shown that the magnetization dynamics of such complexes can be tailored by tuning the coordination geometry and ligand-field around the metal centres. In particular, low-coordinate Ln(III) complexes seem to be quite attractive as molecular magnets, some of them displaying significantly large energy barriers for magnetization reversal with high blocking temperatures. In this *review article*, a concise but comprehensive introductory section to the basics of the magnetic anisotropy of the lanthanide ions is portrayed along with the conventional classifications and quality-check parameters of the molecular nanomagnets. We have elaborated with examples the magneto-structural correlation in various lanthanide-based molecular complexes with coordination numbers ranging from one to seven, and have highlighted the most promising systems as nanomagnets. We have also reviewed various examples of low-coordinate lanthanide-based molecular nanomagnets that are encapsulated inside fullerene cages of various sizes. A short section dealing with the lanthanide ions-based magnetic systems exhibiting slow relaxation of magnetization is also included. A special attention is also paid to the magneto-structural correlation of the lanthanide-based half-sandwich, pseudo-sandwich and a special class of sandwich complexes.

Contents

1. Introduction 164
  1.1. Definition and classification of molecular nanomagnets 165
    1.1.1. Single-ion magnet nomenclature: a few more remarks 165
  1.2. Electronic states of Ln(III) ions 166
    1.2.1. Additional perturbations 166
  1.3. Crystal-field symmetry and ionic anisotropy 167
  1.4. Determination of crystal-field parameters 168
  1.5. Quality-check parameters of Ln single-molecule magnets 170
    1.5.1. Determination of the effective barrier height (U_{eff}) for magnetization reversal 170
    1.5.2. Determination of magnetization blocking temperature (T_B) 171
  1.6. General mechanisms for magnetization relaxation 172
    1.6.1. Temperature dependence of spin-phonon coupling relaxation 172
2. Overview of the reported literature 173
  2.1. Magnetic sites doped on surfaces 173
  2.2. Hepta-coordinate lanthanide complexes 176
  2.3. Hexa-coordinate lanthanide complexes 185

---

* Corresponding authors at: Tata Institute of Fundamental Research Hyderabad, Gopanpally, Hyderabad 500107, India (V. Chandrasekhar).
E-mail addresses: amiakb@gmail.com (A.K. Bar), rajaraman@chem.iitb.ac.in (G. Rajaraman), vc@iitk.ac.in, vc@niser.ac.in (V. Chandrasekhar).

https://doi.org/10.1016/j.ccr.2018.03.022
0010-8545/

2.4. Penta-coordinate lanthanide complexes 187
2.5. Tetra-coordinate lanthanide complexes. 189
2.6. Tri-coordinate lanthanide complexes. 192
2.7. Bi-coordinate lanthanide complexes 196
2.8. Mono-coordinate lanthanide systems 198
2.9. Pseudo-sandwich and half-sandwich lanthanide (III) complexes. 202
2.9.1. Pseudo-sandwich lanthanide (III) complexes 203
2.9.2. Half-sandwich lanthanide complexes 205
2.9.3. Cycloalkenyl-capped sandwich lanthanide complexes. 207
3. Conclusion and outlook 212
Acknowledgments 213
References 213

1. Introduction

The discovery of slow relaxation of magnetization, at very low temperatures, in a Mn_{12} cluster, by Sessoli et al. [1–3] has triggered an intense flurry of research activity in the field of molecular magnetism, with enthusiastic participation from the physics, chemistry and materials science community [4–15]. The ultimate goal of these research activities is to achieve magnetically bi-stable molecular complexes, also known as single-molecule magnets (SMMs) that can exhibit magnetization-blocking at readily accessible temperatures so that such complexes can be utilized in novel applications such as information storage, spintronics, quantum computing, multiferroics, *etc.* [4,6,7,13–16]. While realizing these goals, in full, appears distant at the moment, the focus of immediate endeavours is to understand the fundamental factors that control SMM behaviour and then to translate the understanding gained to come out with better synthetic methodologies for assembling SMMs with improved properties. Through such work, involving both experimental and theoretical research, it has been realized initially that the effective energy barrier (U_{eff}) for magnetization reversal in transition metal-based magnetically bi-stable molecular complexes depend linearly on the zero-field splitting parameter, D, and quadratically on its ground state spin, S; i.e. $U_{eff} = |D|S^2$ for integer spin and $U_{eff} = |D|(S^2 - ¼)$ for half-integer spin [4–16].

The initial efforts looked at the quadratic dependence on S as the main means to prepare high-performance molecular magnets [9,14,17]. Thus, several polynuclear paramagnetic transition metal complexes were prepared and studied with the aim of achieving very large ground-state spins [4,16]. But, while large ground-state spins have been achieved in many complexes, the overall molecular D parameters of such magnetic clusters, in general, are found to be very low [4,16]. It is worth emphasizing here that for the polynuclear molecular nanomagnets, it is very difficult to enhance concomitantly both the S and D parameters. The dependence of U_{eff} on S is essentially linear instead of quadratic for the cluster molecular nanomagnets that incorporate relatively larger number of magnetic centres (metal ions) [18,19]. The overall molecular D parameter, which is a resultant of all the contributions from each and every local anisotropic metal centre in the cluster, is obviously expected to be low where the ionic magnetic anisotropy axes of the constituent metal centres are randomly orientated, which is more like a general phenomenon rather than an exception. The magnitude of the overall molecular D parameter of the cluster molecular nanomagnets follows inverse proportionality to the ground state spin, S, i.e., $D \propto 1/S$, and the nature of D parameter (*easy-plane* or *easy-axis*) is largely influenced by the nature of the magnetic exchange interactions (ferromagnetic or anti-ferromagnetic) among the metal centres in the clusters [19]. Therefore, assembling very large-sized clusters possessing a gigantic spin ground state does not guarantee, in any way, SMM behaviour [16]. It is worth remembering that the expression of U_{eff} associating D parameter and ground state spin, S, as mentioned above, is valid only for the transition-metal based molecular nanomagnets. It does not hold for the lanthanide based molecular nanomagnets. However, in transition metal complexes the crystal field (CF) splitting is found to be larger compared to spin–orbit coupling ($\sim 10^3$ cm^{-1} and $\sim 10\ cm^{-1}$ respectively for *3d* series) and the orbital angular moment is quenched in most of the cases (except for the low-coordinate complexes). Contrary to this, in lanthanide complexes, the valence *4f* orbitals are deeply buried and almost non-interacting with ligand field, resulting in a small CF splitting compared to the spin-orbital coupling. As a result, lanthanide ions (except La(III), Gd(III), Lu(III)) possess large unquenched orbital angular moment along with a large magnetic moment. Therefore, lanthanide ions have attracted considerable attention in the arena of single-molecular magnetism [20–32]. However, fine tuning the magnetic anisotropy in polymetallic complexes that are usually prepared via serendipitous synthetic strategies is extremely difficult considering the many variables such as the orientation of the magnetic anisotropy axes, chemical environment, crystal-field strength and coordination geometry of the constituent paramagnetic anisotropic ions. On the other hand, tailoring magnetic anisotropy of paramagnetic metal ions in mononuclear complexes via chemical and geometric tuning appears relatively easier [21,22,27,33].

Notably, significant impact of strong magnetic anisotropy of the Ln(III) ions towards the enhancement of coercive field for the magnetization blocking in *3d-4f* three-dimensional coordination frameworks was well documented as early as in 1976 [34]. Slow relaxation of magnetization of single-ion origin was reported by Gao and co-workers for a *3d-4f* two-dimensional coordination polymer $[Nd^{III}Co^{III}(bpym)(CN)_6(H_2O)_4]\cdot 3H_2O$ (where bpym = 2,2′-bipyrimidine) in 2001 [35]. However, observation of slow relaxation of magnetization in Ln(III) based mononuclear sandwich complexes was first reported by Ishikawa and co-workers in 2003 [36], and this report has since triggered interest in complexes containing Ln(III) ions. As low-coordinate high-symmetry complexes are anticipated to possess large magnetic anisotropy [27,33,37], there has been a natural motivation to explore such compounds. Between low-coordinate lanthanide-based and transition metal ion-containing single-ion magnets, the former are more challenging because of the following reasons. First, as Ln(III) ions are bigger in size and contain shielded *4f* orbitals, they prefer large coordination numbers and hence, stabilization of low-coordinate Ln(III) complexes requires appropriate synthetic strategies [38]. Second, prediction and rationalization of magnetic anisotropy in Ln(III) complexes is more difficult than in transition metal complexes because of the complexities involved in the theoretical studies of the former [39]. Nonetheless, there have been successful efforts at assembling low-coordinate Ln(III)-containing molecular magnets and studying them both experimentally and theoretically.

It may be recalled from the tenets of coordination chemistry that Ln(III) ions prefer higher coordination numbers, usually eight to twelve, due to large ionic radii and strong ionic bonding [40–43]. In order to assign the low or high coordination numbers of Ln-based complexes, it is worth citing the extensive survey by Huang [40]. Analysis of 1389 crystal structures of well-defined Ln complexes revealed that the most abundant coordination number is eight and the population steeply decreases upon moving towards either higher or lower coordination numbers (Fig. 1). Coordination numbers of seven and below for Ln(III) ions thus may be considered as low.

Low-coordinate Ln-complexes including pseudo-sandwich, half-sandwich, a special class of sandwich complexes and Ln(III) clusters encapsulated within fullerenes, are the focus of this article [21,22,25,38,39,44–56]. The aim of this article is to present an overview of the most important aspects of the low-coordinate Ln(III)-based single-ion magnets (SIMs). These include their synthetic design and structural features along with their magnetic behaviour. An effort would be made, wherever possible, to focus on a rational understanding of the observed magnetic anisotropy and slow magnetization dynamics of such complexes in terms of the coordination geometry and ligand field. It is also important to note that even though many complexes can be considered as low-coordinate considering only the strongest interactions, many of them show significant short contacts that may play an important role in the observed magnetic behaviour. In most cases, therefore, ideal coordination numbers/geometries are not observed. This reality has to be kept in mind when generalizations of magnetic behaviour and correlating them with structural features are attempted. The conclusions drawn in all such cases have to be tempered with caution because even minor changes can make a major impact on the observed magnetic behaviour. Before embarking on the main subject matter of this article, we begin with a brief introduction to the general area of molecular magnets and the characteristics of the Ln(III) ions that are of relevance to their use in molecular magnets.

1.1. Definition and classification of molecular nanomagnets

Though this review is devoted to monometallic Ln-based nanomagnets, for the comparison purpose, it is worth mentioning different nomenclatures of molecular nanomagnets. Overall, molecular complexes with paramagnetic metal ion(s) that exhibit slow magnetic relaxation and magnetic hysteresis loops are referred broadly as **S**ingle-**M**olecule **M**agnets (SMMs) [2]. Often many compounds do not exhibit hysteresis loops at accessible temperatures of a normal SQUID magnetometer. Thus, non-observation of magnetic hysteresis at the accessible measured temperatures needs to be considered only as negative evidence for lack of SMM behaviour. However, slow relaxation of magnetization is evidenced in the alternating current (ac) magnetic susceptibility measurements. The SMMs exhibiting the slow relaxation in absence of externally applied direct current (dc) magnetic field are generally referred as zero-field SMMs. In some instances, however, a constant dc field is applied to observe the slow relaxation (field-induced SMMs) if no signals are witnessed at zero-field. Notably, these characteristics have to be of purely molecular origin. A further useful sub-division in classification is based on the number of paramagnetic ions present and the structural dimension of the compound: (i) discrete molecules containing more than one paramagnetic metal ions where, if not all, at least, the neighbouring paramagnetic centres are magnetically coupled are still called SMMs [2]; (ii) coordination polymers, typically one-dimensional, containing paramagnetic metal ions in the backbone and where the neighbouring metal ions are involved in magnetic exchange interactions are commonly known as single-chain magnets (SCMs) [11,57–60]; (iii) finally, if a paramagnetic complex contains a single metal ion, yet exhibits the feature of an SMM, it is known as a single-ion magnet (SIM) [36,61,62]. All these three types of molecular magnets exhibit the property that once they are magnetized below certain temperatures, they retain the magnetization even after the field is switched off. In principle, such systems once magnetized can remain magnetized indefinitely, below certain temperatures. However, in practice, particularly above the critical temperatures, the magnetization is lost as a result of multiple relaxation pathways that the system can access. We tabulate herein the characteristics of a few representative molecular nanomagnets of all types: *3d* transition metal-based mono-/polynuclear, *4f* Ln-based mono-/polynuclear and *3d-4f* mixed-metal polynuclear molecular nanomagnets (Table 1).

1.1.1. Single-ion magnet nomenclature: a few more remarks

The term “single-ion magnetic materials” existed in nuclear magnetic resonance (NMR) spectroscopy (lanthanide shift reagents) long before the discovery of today’s single-ion magnets (SIMs) [32]. In NMR spectroscopic techniques, several paramagnetic lanthanide-based mononuclear complexes are used as shift reagents [75,76]. The unpaired electrons of the lanthanide ions are accommodated in the deeply shielded *4f*-orbitals and hence, they are not significantly influenced by the coordinating ligands. This is one of the reasons why such complexes are used as the standard paramagnetic shift reagents for enhancing the resolution of NMR signals via increasing the coupling constants of the neighbouring NMR active nuclei [75,76]. A *single-ion magnet* is now a widely accepted term for any complex that contains one paramagnetic metal ion, and that exhibits slow relaxation of magnetization which is of purely molecular origin. The first discovery of a lanthanide-based mononuclear complex exhibiting slow relaxation of magnetization was reported by Ishikawa et al. in 2003 for Tb(III) and Dy(III) containing double-decker complexes [36]. On the other hand, the first transition-metal based SIM was reported later by Long et al. in 2010 involving a high-spin Fe(II)-based mononuclear complex [62]. It is important to note here that the term single-ion as used in the molecular magnetism literature merely means that the compound in question has a single paramagnetic ion while containing a large non-magnetic organic shell and sometime even diamagnetic transition metal ions.

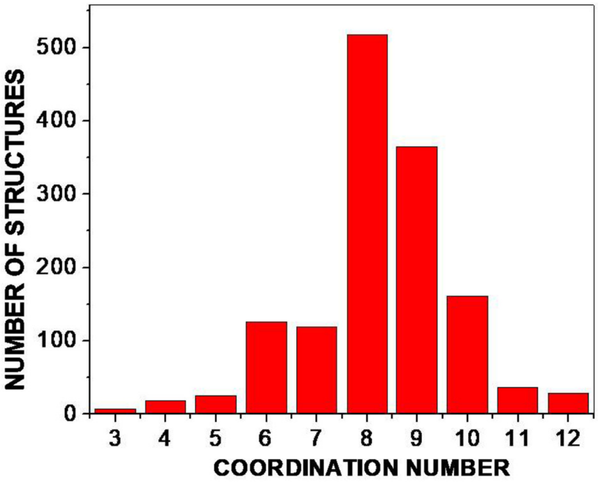

Fig. 1. Abundance of coordination numbers in Ln-complexes (La–Nd, Sm–Lu, Y) based on the analysis of 1389 crystal structures published between 1935 and 1995. The plot is created using the data reported in Ref. [40].

Table 1
Representative single-molecule- and single-ion magnets that display high energy barriers (U_{eff}) and high blocking temperatures (T_B).

Complex	U_{eff} (cm^{-1}) (H_{dc} = 0 Oe)	T_B (K)	Sweep rate (Oe/s)	Refs.
Transition Metal ion based SIMs and SMMs				
[(IPr)CoNDmp]	413	9.5	700	[63]
[K(crypt-222)] [$Fe(C(SiMe_3)_3)_2$]	226	4.5	50	[64]
[$Mn^{III}_6O_2$(Et-sao)$_6$($O_2CPh(Me)_2)_2(EtOH)_6$]	60	4.5	1400	[65]
[$Mn_{12}O_{12}(O_2CCH_2Br)_{16}(H_2O)_4$]	52	3.6	20	[66]
Ln(III -based SIMs and SMMs				
[$Cp^{ttt})_2Dy][B(C_6F_5)_4$]	1277	60	39	[67,68]
[Dy(OtBu)$_2$(py)$_5$][BPh_4]	1261	14[‡]	–	[69]
$Dy(Cy_3PO)_2(H_2O)_5]Br_3\cdot 2(Cy_3PO)\cdot 2H_2O\cdot 2EtOH$	377	20	200	[48]
[Dy(bbpen)Br]	712	14	200	[46]
[Tb((O-(C_6H_4)-p-tBu)$_8$ Pc)(Pc)]	652	2	[†]	[70]
[K(18-crown-6)][Er(COT)$_2$]	199	11	35	[71]
[$Dy_4K_2O(OtBu)_{12}]\cdot C_6H_{14}$	481	5	1400	[56]
[$Dy_5O(O^iPr)_{13}$]	368	1.85	[†]	[72]
[K(18-crown-6)(THF)$_2$][{[($Me_3Si)_2N]_2$(THF)Ln}$_2$(μ-η^2:η^2-N_2)]	227	14	9	[53]
[$Dy_4(\mu_3-OH)_2$(bmh)$_2$(msh)$_4Cl_2$]	118	7	1400	[73]
Heterometallic 3d-4f SMMs				
[$Fe_2Dy(L^1)_2(H_2O)]ClO_4\cdot 2H_2O$	319	–	–	[74]
[$Zn_2Dy(L^2)_2(MeOH)]NO_3\cdot 3MeOH\cdot H_2O$	305	11	200	[54]

Ligand abbreviation: Cy = cyclohexyl; bbpen = N′-bis(2-hydroxybenzyl)-N,N′-bis(2-methylpyridyl)ethylediamine;crypt = cryptand; py = pyridine; pc = phthalocyanine; dmp = 2,6-dimesitylphenyl; IPr = N, N′-bis(2,6-diisopropylphenyl) carbine; sao = salicylaldoxime; COT = cyclooctatetraene; THF = Tetrahydrofuran; H_2bmh = 1,2-bis(2-hydroxy-3-methoxybenzylidene) hydrazone; msh = 3-methoxysalicylaldehyde hydrazine; L^1 = 2,2′,2″-(((nitrilotris(ethane-2,1-diyl))tris(azanediyl))tris(methylene)) tris(4-chlorophenol); L^2 = 2,2′,2″-(((nitrilotris(ethane-2,1-diyl))tris(azanediyl))tris(methylene))tris-(4-bromophenol); Cp^{ttt} = 1,2,4-tri(tert-butyl)cyclopentadienide.

[†] Field sweep rate is unknown.

[‡] obtained from zero-field cooling experiment.

1.2. Electronic states of Ln(III) ions

Since this review deals with molecular magnets based on lanthanide complexes, it is pertinent to give a brief overview about the magnetic properties of Ln(III) ions. For greater details the reader is referred to authoritative review articles [31]. Compared to the first row transition metal ions, Ln(III) ions possess large spin ground states and an inherently stronger magnetic anisotropy [9]. Notably, Gd(III) ($4f^7$) is magnetically almost isotropic in nature. Eu (III) ($4f^6$) inherits a non-magnetic ground state (total angular momentum quantum number $J = 0$). Apart from these two ions, all the remaining Ln(III) ions could be potential candidates for molecular nanomagnetism. However, Dy(III) ion is endowed with a unique characteristic of the largest free-ion magnetic moment among its congeners resulting from the combination of a high total angular momentum ($J = 15/2$) and large *g*-factor ($g_j = 4/3$) [9]. Consequently, the central ion in the arena of Ln(III)-based molecular nanomagnets is Dy(III) and a vast number of Dy(III)-based complexes are found to exhibit fascinating SMM behaviour. However, as mentioned before, since the unpaired electrons of the Ln(III) ions reside in the significantly shielded *4f* orbitals, the orbital angular momentum remains mostly unquenched by crystal fields resulting in a significantly strong first order spin-orbit coupling (SOC) [9]. This is one of the important reasons, from the magnetism point of view, for the interest in Ln(III) complexes [10]. In order to have at least a qualitative understanding of the electronic states of the Ln(III) ions, a representative energy spectrum of the electronic states and the commonly involved perturbations for Dy(III) ion is depicted in Fig. 2. The electron-electron repulsions within the *4f* orbitals results in several possible electronic states according to the Russel-Saunders coupling scheme (Fig. 2) [9]. In the case of Ln(III) ions, the effect of SOC is much larger than crystal field effects on the splitting of the electronic states. Hence, the effect of the latter can be considered as a perturbation to the electronic states generated by the former. With this brief background, let us examine the electronic energy levels of Dy(III). The ground state term symbol can be determined by Hund's rules [77] which for Dy(III) is $^6H_{15/2}$ (Table 2). The degeneracy of the magnetic eigen states present in the term symbols is lifted due to SOC. For the Ln(III) ions possessing oblate electrostatic potential surfaces corresponding to the eigen states of the ground *J* manifold, the eigen state with the larger total quantum number (M_J value) will be more stable for strong axial crystal-field environments (Fig. 2). Each of these eigen states corresponds to a defined magnetic moment oriented along a particular direction with respect to ionic local coordinates. Because of this, the measurement of a magnetic property such as magnetic susceptibility will sense different magnitudes for different polar and azimuthal angles which are described as magnetic anisotropy. The various energy levels of the eigen states lead to preferential population distribution, particularly below a certain temperature. Hence, the macroscopic magnetization moment and its orientation are dictated by the most-populated eigen state.

1.2.1. Additional perturbations

In addition to the description given above, each of the magnetic eigen states of the free ion will again split into several ($2J + 1$) possible electronic states (spectroscopic terms) if the Ln(III) ion is under the influence of a non-spherical ligand field. From the coordination chemistry of lanthanide ions, it can be readily seen that most of them prefer large coordination numbers in the range of eight to eleven with generally distorted coordination geometry and hence possess low symmetry. Therefore, in most of the cases, the degeneracy of these spectroscopic terms is completely lost, what remains is the so-called time-reversal symmetric degeneracy. As the electronic spins constitute time-reversal symmetric quantum eigen states, each of the electronic states is at least doubly degenerate except under few conditions. For the systems with an integer value of *J*, the *non-Kramers ions*, this double degeneracy of M_J level is lifted in low symmetric environment by crystal field of the ligands. On the other hand, for the systems with a half-integer value of *J*, the *Kramers ions*, these factors cannot remove the degeneracy according to the Kramers double degeneracy theorem [9]. However, irrespective of the nature of *J*, this double degeneracy is lost in the presence of an external magnetic field, which is the Zeeman effect [9]. Each of the Zeeman lines can again be split into a set of very closely spaced (Fig. 2) electronic states owing to coupling with nuclear spins (hyperfine splitting); however, this

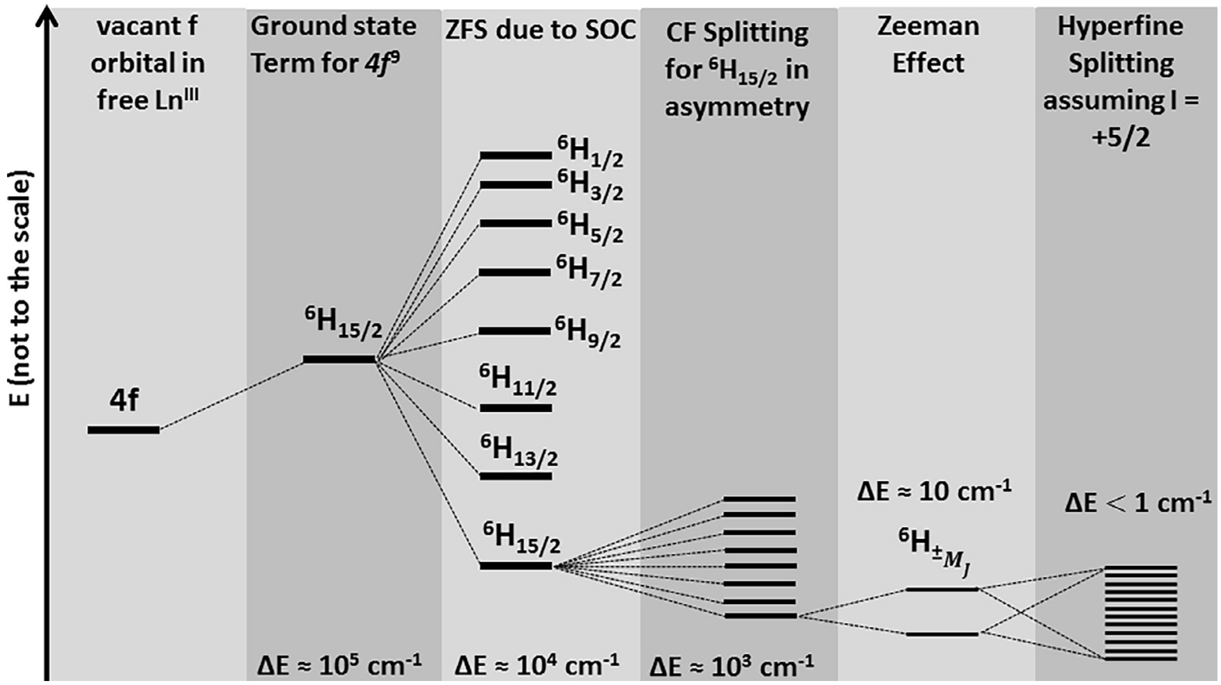

Fig. 2. A schematic relative energy spectrum (*not to the scale*) of electronic states originated from *4f* orbital of the Dy(III) ion (*4f*^{9}) *via* perturbations through (from left to right) electron-electron repulsion (only the ground state term symbol, $^6H_{15/2}$, is shown), SOC, CF interactions, Zeeman effect (under $\sim$ 1 T dc field) and electron-spin-nuclear-spin coupling (hyperfine coupling), respectively. ΔE refers to the approximate energy separation between the ground and excited states of the respective perturbation domain. It is important to note here that there are seven stable isotopes for Dy, among which the ^{161}Dy (I = +5/2) and ^{163}Dy (I = −5/2) are the only two nuclear spin active isotopes. The natural abundances of these two isotopes are 18.9% and 24.9%, respectively. For simplicity, only one isotope of Dy(III) is considered here.

Table 2
Spin-orbit ground term symbols for Ln(III) ions.

Ln(III)	Ce	Pr	Nd	Pm	Sm	Eu	Gd	Tb	Dy	Ho	Er	Tm	Yb
f^n	f^1	f^2	f^3	f^4	f^5	f^6	f^7	f^8	f^9	f^{10}	f^{11}	f^{12}	f^{13}
Term symbol	$^2F_{5/2}$	$^3H_4$	$^4I_{9/2}$	$^5I_4$	$^6H_{5/2}$	$^7F_0$	$^8S_{7/2}$	$^7F_6$	$^6H_{15/2}$	$^5I_8$	$^4I_{15/2}$	$^3H_6$	$^2F_{7/2}$
Free ion g-value	6/7	4/5	8/11	3/5	2/7	0	2	3/2	4/3	5/4	6/5	7/6	8/7

perturbation is usually weak. In situations where crystal-field perturbation is significant, hyperfine splitting influences the macroscopic magnetic properties prominently [78–82]. This influence is particularly manifested in magnetization relaxation of such systems through the mechanism of quantum tunnelling (*vide infra*). Finally, it may be mentioned that since the electronic energy levels are influenced by SOC in conjunction with CF, the macroscopic magnetic properties of the Ln(III) ions become complicated and hence, the temperature dependence of the magnetic susceptibility of these systems does not follow the phenomenological Curie-Weiss law [9,10].

1.3. Crystal-field symmetry and ionic anisotropy

From the chemists' viewpoint, it is immensely important to know what kinds of chemical and geometric environments around the metal ions are to be targeted in order to induce desired magnetic properties. It is worth recalling here, at least qualitatively, the impact of crystal-field symmetry on the magnetic properties of the Ln(III) ions. As mentioned in the preceding section, any low-symmetry ligand field around the Ln(III) sites lifts the $2J +$ 1degeneracy of the free-ion eigen states (Fig. 2) [83]. For an electron, i, such perturbation can be described by a one-electron operator, $u_{CF}(i)$, accounting for the potential generated by a charge distribution $\rho(\mathbf{R})$ as a function of radial distance, r_j, as expressed in Eq. (1).

$$u_{CF}(i) = -e\int \frac{\rho(\boldsymbol{R})}{|\boldsymbol{R}-r_j|}dv \qquad (1)$$

The overall perturbation (U_{CF}) on an ion constitutes the sum of these one-electron operators acting on all the electrons. One can thus determine the CF perturbation from the solution of a secular determinant with matrix elements of the genre $<\Psi_k|U_{CF}|\Psi_k>$, where Ψ corresponds to the many-electron eigen function [83]. It is worth noting that Ψ_k can be expressed by spherical harmonics. Thus, there is complete freedom to analyse all the possible symmetries of perturbations around metal ion sites. In reality, according to Stevens, the product of a radial function and of Legendre polynomials can describe satisfactorily the electrostatic potential around the Ln(III) ions satisfying all the possible symmetry conditions [84]. Thus, one can express the potential in terms of an irreducible representation of a sub-group of the rotation group. Following this, an operator equivalent approach, where the overall potential is a sum of equivalent angular momentum operators, enables one to express the above mentioned matrix elements via choosing an appropriate constant element. Under this circumstance, the Hamiltonian, $\hat{H}_{CF}$, describing the overall CF perturbation can be then expressed through a phenomenological relation according to the Wybourne formalism [85] as in Eq. (2).

$$\hat{H}_{CF} = \sum_{i,k,q} \tilde{B}_k^q C(i)_k^q \qquad (2)$$

Where $\tilde{B}_k^q$ corresponds to crystal-field (CF) coefficients, $C(i)_k^q$ stands for a one-electron operator equivalent acting on ith electron and it can be defined by spherical harmonics, $P(i)_k^q$, as defined by Eq. (3):

$$C(i)_k^q = \sqrt{\frac{4\pi}{2q+1}} P(i)_k^q \tag{3}$$

It is important to note that the Eq. (2) stands meaningful only for well-defined coefficients. For example, for the Ln(III) ions, it is limited to $k \leqslant 7$ and $-k \leqslant q \leqslant k$. The parts associated with even k (0, 2, 4, 6) determine the CF splitting and the parts associated with odd k (1, 3, 5, 7) determines the electronic dipole transition probability in optical spectroscopies [86,87]. In view of magnetic properties of the Ln(III) ions, it is quite reasonable to consider only the ground state eigen functions of the ions, i.e. considering only even k. Again at the same time, where the SOC renders much more energy splitting than the CF splitting, as in Dy(III) complexes, one can assume negligible mixing between different *J* multiplets. Thus, in the cases of Ln(III) ions, the CF Hamiltonian can be simplified according to Stevens formalism [84] as in Eq. (4), where the one-electron operator equivalent P_k^q can be expressed as a function of total quantum number *J*.

$$\hat{H}_{CF(J)} = \sum_{k,q} B_k^q P_k^q = \sum_{k,q} a_k (1 - \sigma k) A_k^q < r^k > P_k^q \tag{4}$$

where k is the operator order; $<r^k>$ is the expectation value of r^k; a_k corresponds to the Stevens equivalent coefficients α, β, γ for k = 2, 4 and 6, respectively; σ_k represents the shielding parameters of the *4f* shells of the Ln(III) ion. Notably, both A_k^q and B_k^q correspond to the ground state CF parameters. The non-zero q terms must be consistent with the point group symmetry around the Ln(III) ion sites. The non-vanishing CF parameters associated with the Ln(III) ion sites under commonly observed symmetries are well-described [88,89]. The negative q values correspond to the complex operators, but all the Stevens coefficients are real [90]. The detailed expressions of the operator equivalents and the corresponding matrix elements are described [89,90]. It is worth emphasizing that one can establish a correlation between the CF parameters $\tilde{B}_k^q$ and B_k^q, where the former is associated with both the ground and excited states and the latter with only the ground states, in terms of α, β and γ by using Eqs. (2) and (4). The subtraction transformation $\tilde{B}_k^q - B_k^q$ can be used for the assessment of the nature of magnetic anisotropy. Notably, in an identical ligand environment, drastically different magnetic anisotropy can result for different Ln(III) ions [33,91]. Using these parameters, one can speculate whether a particular Ln(III) ion in the ligand environment will be an *easy-plane* or an *easy-axis* (*vide infra*) anisotropic system [92,93].

Rinehart and Long have given a qualitative picture to assist in maximizing the single–ion anisotropies of Ln(III) ions in a particular crystal field environment [33]. The strong angular dependence of *4f* orbitals leads to different *4f* electron charge densities in the Ln(III) ions. The basic shapes of the charge density distributions corresponding to various eigen states in the ground *J* manifold for various Ln ions are calculated mathematically by a quadrupole approximation [33]. For the same purpose, with more rigorous mathematical calculations considering higher ranking terms, Jiang et al. have employed an electrostatic model with an effective point charge displacement consideration [94]. However, the shapes are found to be prolate (axially elongated), oblate (equatorially expanded), or isotropic (spherical) in a given frame of reference. The shapes of the electrostatic potential surfaces corresponding to the eigen states with the maximum M_J values of ground *J* manifolds for different Ln(III) ions, as evaluated by Jiang et al. [94], are shown in Fig. 3 (top). On the other hand, Fig. 3 (bottom) also displays the variations of the shapes of the electrostatic potential surfaces corresponding to the eigen states of different M_J values of the ground *J* manifolds for different Ln(III) ions, as calculated by Long et al. [33].

Obviously, the eigenstate(s) (with pure M_J or mixed state) associated with the minimized electron-electron repulsive contacts between ligand and *4f* electron charge cloud will be the most stable. Naturally for best SIM characteristics, one needs the largest M_J value as a ground state and the gap between the ground and the excited states has to be as large as possible. Ideally, relaxation via the highest lying M_J energy level would render the highest possible energy barrier for magnetization reversal. To achieve this, the orientation of the anisotropic axes of the excited M_J levels must be co-linear with the ground state anisotropy axis. This condition is difficult to meet in an asymmetric ligand field environment. However, if desired symmetry/pseudo symmetry is maintained, this is certainly achievable and in this regard low-coordinate lanthanide complexes have a better chance of being *good* molecular magnets than other classes of compounds.

1.4. Determination of crystal-field parameters

Complete understanding and analysis of magnetic behaviour of SIMs require accurate determination of CF parameters (the Stevens coefficients). According to the Stevens formalism (Eq. (4)), if we ignore hyperfine splitting (Fig. 2), the magnetic behaviour of a Ln (III) ion is characterized by as high as 27 independent coefficients if the Ln(III) ion is under a non-spherical field. Therefore, reliable determination of magnetic properties of such systems through model-fitting is nearly impossible due to over-parameterization issues. However, higher symmetry reduces the number of Stevens coefficients and therefore makes it easier to simulate magnetic data. The allowed Stevens coefficients for different ligand-field symmetries are described in literature [95,96]. It is also worth noting here that the angular overlap model [97–99] can also be employed alternatively for describing CF perturbation where the parameters are chosen intuitively based on the chemical models. However, the recommended ways of accurate determination of the crystal-field parameters are spectroscopic techniques in conjunction with the magnetization measurements. In principle, the eigen function corresponding to each electronic sub-multiplet can be scrutinized and the associated eigen values can be probed by appropriate spectroscopic techniques subject to the practical limitations. The useful spectroscopic techniques are electron paramagnetic resonance (EPR), [100] inelastic neutron scattering (INS), [101,102] nuclear magnetic resonance (NMR), [103–106] low-energy X-ray absorption (X-ray absorption spectroscopy (XAS) and X-ray magnetic circular dichroism (XMCD), [107–109] and optical absorption and luminescence [110–112]. A qualitative diagram depicting the energies involved in various spectroscopic measurements is portrayed in Fig. 4.

Considering the vast possibilities of coordination geometries and chemical environments around various metal centres, theoretical prediction of model complexes for potential SIMs bears immense importance. In this regard, considerable attention has been paid to formulate reliable methodologies for accurate determination of CF parameters using first principle methods. This is difficult and computationally highly expensive. Nevertheless, several approaches are now in use. For example, the magnetic properties of Ln(III) ions are well reproduced via *ab initio* calculations using multi-configurational self-consistent field methods (eg. CASSCF) [113–115]. Simulation of the magnetic property of Ln (III) ions considering full Hilbert space of all possible microstates of the 4f shell can be satisfactorily performed by the CONDON program [116–118]. The SIMPRE program [119], which is coded with the Stevens coefficients considering effective point-charge models, is attracting attention recently for computing magnetic properties

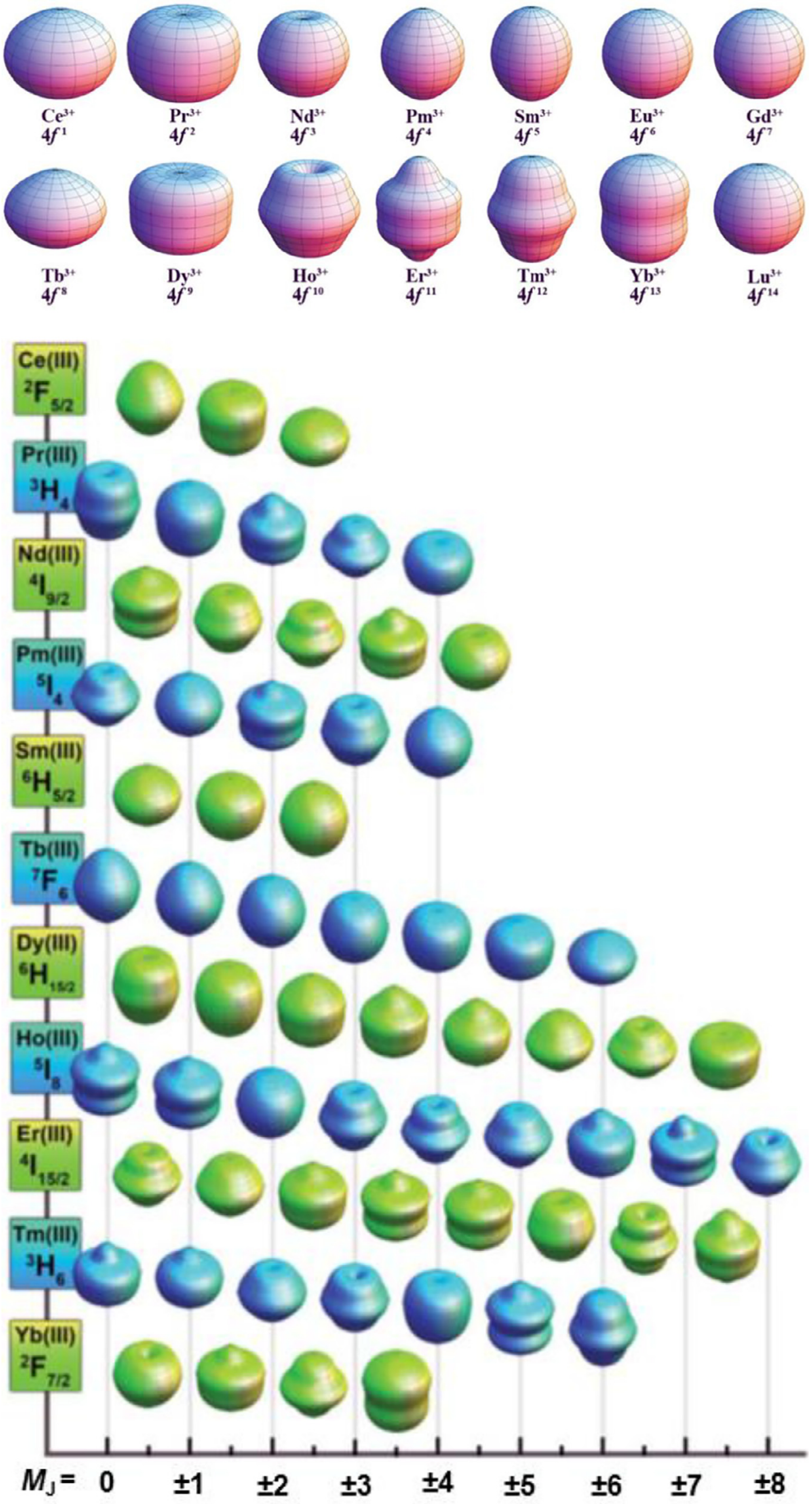

Fig. 3. Electrostatic potential surfaces corresponding to the eigen states with different M_J values for each Ln(III) ion. In absence of crystal-field, all the eigen states with different M_J values are degenerate for a particular Ln(III) ion. The shapes are evaluated with respect to the local reference frame for the electrostatic potential surfaces corresponding to the eigen states with the maximum M_J values (top) [94] and with different M_J values (bottom) [33] for the ground J manifolds of the Ln(III) ions. Figure and captions are reprinted from the Ref. [33], and the Ref. [94] with permission from Royal Society of Chemistry.

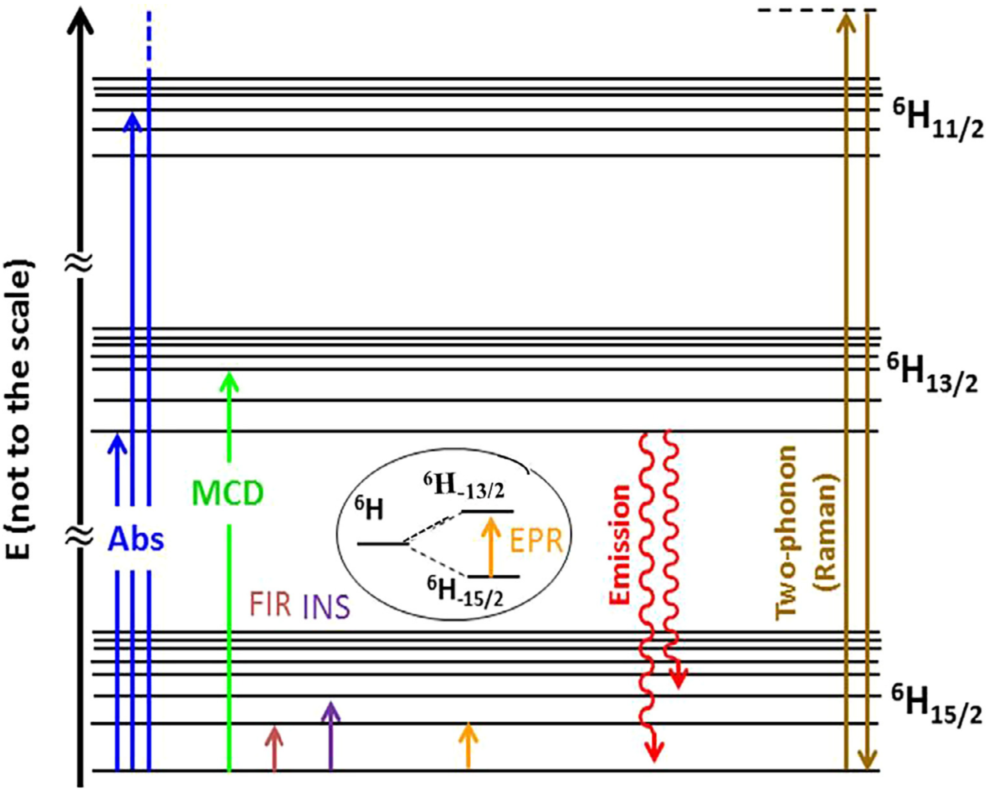

Fig. 4. The eigen states landscape (*not to the scale*) of Dy(III) ion portraying the energy levels associated in optical absorption (Abs), magnetic circular dichroism (DCM), far infra-red (FIR), inelastic neutron scattering (INS), electron paramagnetic resonance (EPR), emission and Raman spectroscopic phenomena. Zeeman effect in general and hyper-fine splitting are omitted for clarity.

of Ln(III) SIMs [119–123,119,120,122–124]. The orientation of the magnetic anisotropy axes and the energy level structures of Dy (III) complexes can be determined by MAGELLAN program which uses electrostatic optimization of the aspherical electron density distribution [120]. But, it is worth pointing out that such evaluation by MAGELLAN program requires the ground doublet to be $M_J = \pm 15/2$ state and no mixing of the ground M_J with excited M_J is expected. For a complex having low-symmetry environment, with strong equatorial ligation, this program cannot be employed.

1.5. Quality-check parameters of Ln single-molecule magnets

For a paramagnetic metal ion possessing magnetic anisotropy that originates from spin-orbit coupling (SOC), the total angular momentum vector, $\hat{J}$, is a linear combination of the total ground state spin vector, $\hat{S}$, and orbital angular momentum vector, $\hat{L}$. The total quantum number is given by either $J = L - S$ if the open shell is less than half-filled, or $J = L + S$ if the open shell is more than half-filled. It is worth remembering that, for the 3*d*-transition metal ions, the CF perturbation is much stronger than SOC perturbation. Therefore, the magnetic microstates (M_S) can be defined by the total ground spin (S) and the energy landscapes of these magnetic microstates is governed by the uniaxial magnetic anisotropy parameter [9]. In contrast, for the lanthanide ions, the SOC perturbation is far stronger than the CF perturbation. Therefore, the magnetic microstates (M_J) can be represented by the total quantum number, J, essentially resulting in a total number of $(2J + 1)$ number of magnetic microstates for a particular $^{2S+1}L_J$ term symbol [9]. However, in the majority of the Ln-based SIMs/SMMs, there exists significant mixing of the eigenstates in the J manifold, which leads to complicated energy landscapes. As mentioned earlier, different Ln(III) ions experience different CF perturbations even in the same coordination geometry and ligand environments, and thus different energy landscapes are expected. To have an insight into this, it is worth citing here the detailed calculations by Ishikawa et al. for the energies of the sub-states of the J manifolds for a series of bis(phthalocyaninato)lanthanide complexes where the Ln(III) ions are sandwiched between two phthalocyaninato ligands (Fig. 5) [93,125]. Effectively, the Ln(III) ions are octa-coordinated and in distorted square-antiprism symmetry. From Fig. 5, it is evident that the eigen states are not necessarily organized following the decreasing/increasing order of either the M_J quantum number or the energy spacing between two adjacent eigen states. Moreover, the direction of the magnetic anisotropy axis may also be different for the eigen states with different M_J quantum numbers [126].

1.5.1. Determination of the effective barrier height (U_{eff}) for magnetization reversal

For an *Ising-type* system with ground $J = 15/2$ (ca. Dy(III) single-ion magnet) under extremely axial CF, the energy landscape of the magnetic microstates could resemble the time-reversal symmetric double-well potential as depicted in Fig. 6. It is also worth mentioning the difference between the height of the double-well potential and the effective energy barrier (U_{eff}) for magnetization reversal. Provided all but Orbach mechanisms of relaxation (*vide infra*, Fig. 6) are prohibited, the molecules in principle can revert their magnetization moment (i.e. jumping from one potential well to other in the double-well potential) via climbing through all the possible M_J states as depicted by dashed-green arrows in Fig. 6. Thus, the energy required for such magnetization reversal equals to the height of the double-well potential ($U = U_{\text{eff}}$; for the definition of U_{eff} see below.). But, in practice, spin-lattice relaxations (direct/Raman) and quantum tunnelling of magnetization accompany the Orbach process. The former processes are more prone in the excited states. Therefore, it is not necessary for the system to *climb all* the possible M_J states for magnetization reversal.

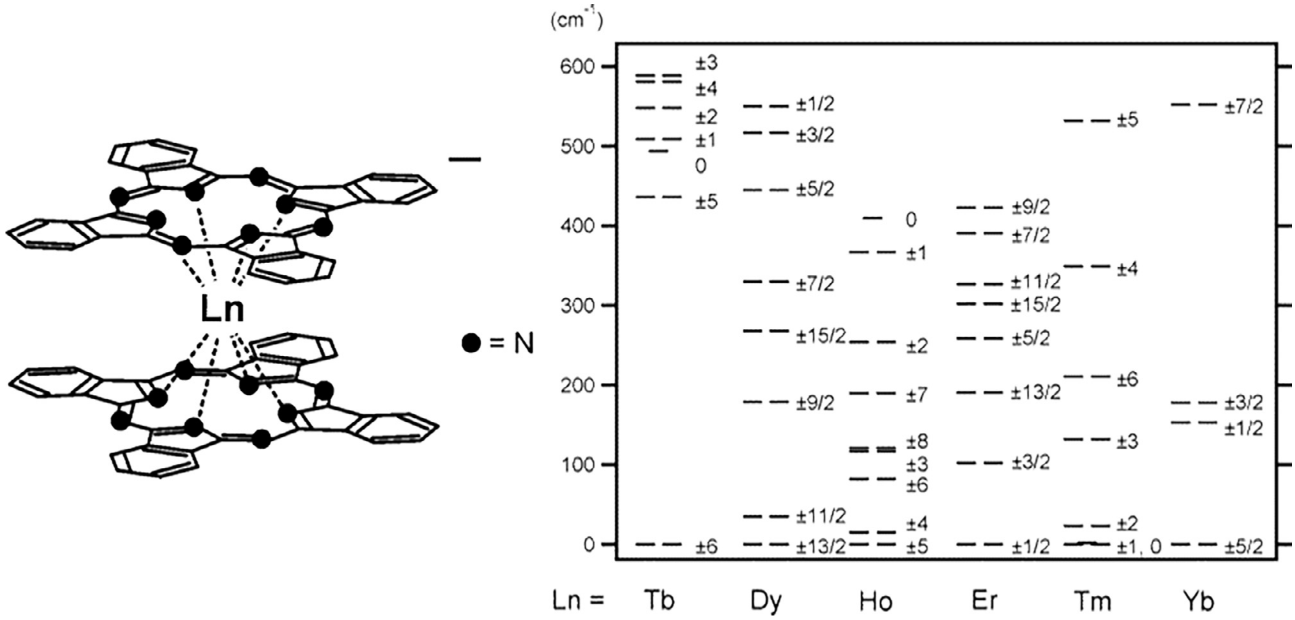

Fig. 5. *Left*: the structure of bis(phthalocyaninato)lanthanide complex anions; *Right:* energy landscapes of the sub-states of the ground *J* manifolds of [Pc$_2$Ln]$^-$TBA$^+$(**1**) (Ln = Tb, Dy, Ho, Er, Tm, or Tb; TBA = tertiary butyl ammonium). The M_J value of each sub-state is indicated to the right hand side of the corresponding energy level. Figure and captions are reprinted with permission from the Ref. [93]; Copyright @ 2003, American Chemical Society, and the Ref. [125]; Copyright @ 2004, American Chemical Society.

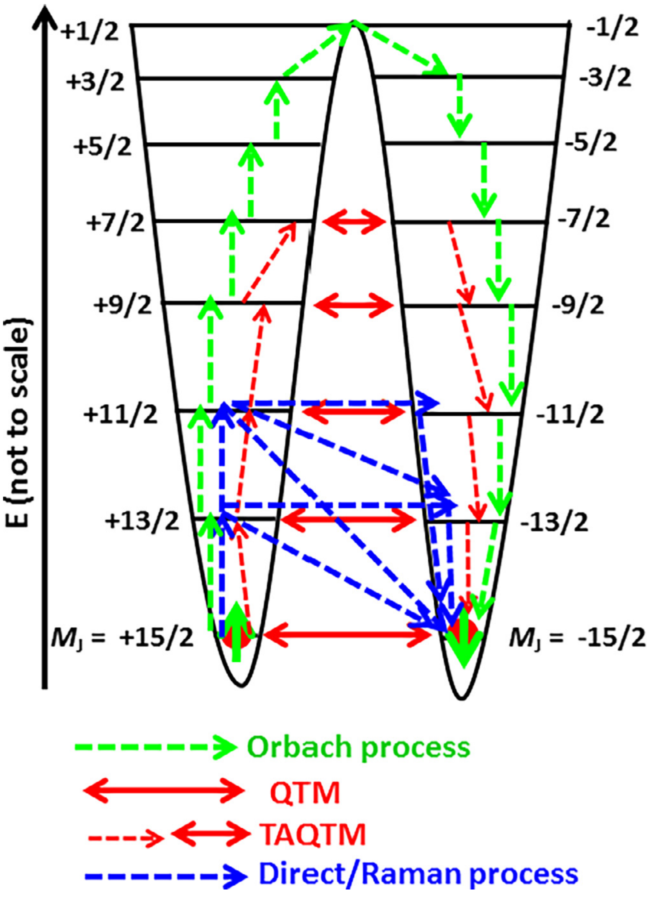

Fig. 6. The most common mechanisms involved in the magnetization relaxation of magnetically bi-stable systems. Colour codes: green = thermally activated (Orbach) process; red = quantum tunnelling of magnetization (QTM) or thermally assisted (TA) QTM; blue = phonon-triggered direct (Raman) spin-lattice relaxation. Generated based on the Ref. [6].

In the majority of Ln(III) based SIMs/SMMs, magnetization reversal takes place through first (eg. $M_J = +15/2 \rightarrow M_J = +13/2 \rightarrow M_J = -13/2 \rightarrow M_J = -15/2$; Fig. 6) or second (eg. $M_J = +15/2 \rightarrow M_J = +13/2 \rightarrow M_J = +11/2 \rightarrow M_J = -11/2 \rightarrow M_J = -13/2 \rightarrow M_J = -15/2$; Fig. 6) excited state [20–33]. Therefore, the effective energy (U_{eff}) required for the magnetization reversal is the energy spacing between the ground state ($M_J = +15/2$) and the first excited state ($M_J = +13/2$) or the ground state ($M_J = +15/2$) and the second excited state ($M_J = +11/2$), respectively in the above both cases. It is worth emphasizing further here that, as mentioned earlier, the eigen states are not necessarily organized following the decreasing/increasing order of the M_J values. As portrayed in Fig. 5, the ground, the first- and second excited states for Tb analogue associate with $M_J = \pm6$, ±5 and 0, respectively. On the other hand, those states for Dy analogue correspond to $M_J = \pm13/2$, ±11/2 and ±9/2, respectively.

However, the quality of an SIM/SMM is certified with the magnitude of the U_{eff} and the threshold temperature (T_B, known as blocking temperature, *vide infra*) below which the slow relaxation of magnetization or magnetic hysteresis loop is exhibited. In other words, the larger the U_{eff} and T_B values are, the better the SIM/SMM is. Experimentally the value of effective energy barrier for magnetization reversal can be determined by the relaxation times (τ) which itself can be extracted from out of phase components (χ'') of the alternating current (ac) magnetic susceptibility, which is elaborated in Section 1.6.1. Several transition metal and lanthanide metal complexes with very large U_{eff} values are reported in the last two decades. Some of the reported lanthanide-based SIMs possess U_{eff} values which are much larger than many of the transition metal SMMs such as {Mn$_{12}$} (See Table 1). However these large values are not directly translated into magnetization blockade in lanthanide complexes as the other relaxation processes are often prominent, rendering U_{eff} value not so useful parameter in the assessment of the efficacy of lanthanide-based SMMs.

1.5.2. Determination of magnetization blocking temperature (T_B)

In order to quickly ascertain the viability of a molecular magnet for any potential utility one of the first criteria that need to be assessed is the blocking temperature, T_B, below which the magnetization is blocked and the system continues to be magnetized even after the field is switched off. However, the magnitude of T_B is subject to the methods that are employed to determine it. Though various schools prefer to express T_B in various ways, there are three basic methods for determining it. The old-fashioned text book definition for T_B is the particular temperature where the zero-field cooled (ZFC) χ_M *vs T* plot exhibits a maximum, but field-cooled (FC) χ_M *vs T* plot does not (χ_M = the molar magnetic susceptibility and T = the temperature in absolute scale). It is to be noted that the value of T_B in this method depends on the applied dc magnetic field and the temperature sweep rate. A higher T_B value is expected for weaker applied dc magnetic field and for faster temperature sweep rate. The blocking temperatures measured by this method for two isostructural SIMs, $[Dy(Cy_3PO)_2(H_2O)_5]Cl_3\cdot(Cy_3PO)\cdot H_2O\cdot EtOH$ (**2**) and $[Dy(Cy_3PO)_2(H_2O)_5]Br_3\cdot 2(Cy_3PO)\cdot 2H_2O\cdot 2EtOH$ (**3**) (Cy_3PO = tricyclohexylphosphine oxide) are 8 K and 11 K, respectively, under 1 kOe dc field at 2 K/min temperature sweep rate [127]. The second method is associated with the field-dependent magnetization measurements where T_B is defined by the maximum temperature (in absolute scale) above which no hysteresis loop is observed at a reference field-sweep rate. Faster field-sweep rates render higher T_B values [127]. For the above two isostructural SIMs, the blocking temperatures measured by this method are 11 K and 20 K, respectively, at a field-sweep rate of 200 Oe/s [127]. The most common method for expressing T_B includes investigation of slow-magnetic dynamics via ac magnetic susceptibility studies. The thermally activated slow-relaxation of magnetization follows first order kinetics [9]. Provided this process is dominant over other processes (*vide infra*), the magnetization blocking is characterized by the maximum observed in the frequency-dependent or temperature dependent *out-of-phase* (χ''_M) ac magnetic susceptibility [4,53,128]. The blocking temperature determined in this method corresponds to the highest temperature at which the average life-time of the magnetization moment is a given period of macroscopic time [7]. A characteristic blocking temperature is observed for a particular ac frequency under a given applied dc magnetic field for a molecular magnet. T_B = 2.5 K for the first discovered SMM, $Mn_{12}ac$, under a minimal applied dc magnetic field that is required to suppress quantum tunnelling of magnetization (QTM) [2].

In order for the blocking temperature to be a universal quality check parameter a universal set of measurements need to be followed. For example, in the case of the Tb(III) SIM, $[([(Me_3Si)_2N]_2(THF)Tb)_2(\mu\text{-}\eta^2:\eta^2\text{-}N_2)]^-$ (**4**) [53], magnetization blocking has been investigated by all the above described three methods. The ZFC χ_M *vs T* plot revealed $T_B \approx 15$ K under an applied dc field of 1 T. Magnetic hysteresis loops are observed up to 15 K for a field-sweep rate of 9 Oe/s. The magnetization blocking is observed up to 34 K within 1.5 kHz ac frequency under zero-applied field. Hence, the T_B could be set to 15 K irrespective of the determination methods provided a specific set of parameters (e.g. applied dc field and temperature sweep rate for ZFC-FC susceptibility study; dc field-sweep rate for hysteresis loop study; and applied dc field and ac frequency for ac susceptibility study) are set for a specific method. If one uses such specific parameters as the reference parameters for expressing T_B, the relative quality of molecule-based magnets could be judged universally.

1.6. General mechanisms for magnetization relaxation

The physical significance of the double well potentials depicted in Fig. 6 is that, if the molecules in a potential well have all the spins up, then the molecules in the other potential well will have all the spins down. For the *Ising-type* systems, the deepest portions of the potential wells are ground states. Movement from one well to the other well is accompanied by spin-flipping i.e., the magnetization is reversed. If the system is kept below a certain threshold temperature (referred as the magnetization blocking temperature; T_B), the molecules cannot shuttle between the potential wells *via* the kinetic energy. Under this circumstance, once magnetized, the magnetization moment will remain oriented along the anisotropy axis for a macroscopic time period before it relaxes back to the ground state. However, such magnetization relaxation of molecule-based magnets can well resemble with the longitudinal relaxation of an angular momentum characterized with the time-scale, τ, which takes place through exchange energy with crystal lattice in a phonon bath. In some of the SIMs, the effective magnetization reversal occurs between the lowest energy eigen states (*Ising*-doublet states) involving with a third excited eigen state. The lowest energy *Ising* doublet states are mutually correlated with the time-reversal symmetry and they incorporate hyperfine splitting (for the systems with non-zero nuclear spins). Therefore, quantum tunnelling of magnetization (QTM), a mechanism for magnetization reversal which does not require any energy barrier, is inevitable in SIMs. QTM is highly efficient in the low-temperature domain and is further promoted by inter-molecular spin-dipolar interactions. Though the ground state QTM is temperature independent, it can also take place between excited *Ising* doublet states being assisted by temperature (as depicted by red dashed lines in Fig. 6). The QTM phenomena in SIMs/SMMs have been extensively studied and elaborated in several reviews and books [7,129,130]. However, it is worth pointing out here that QTM limits the magnetization relaxation times at the lowest temperatures and it decreases the U_{eff} by depleting the ground state magnetization strength [7]. But, QTM can be suppressed significantly by lifting the degeneracy of the *Ising* doublet states by means of applied dc magnetic field and/or strong magnetic exchange bias [4,6]. Moreover, symmetry of the coordination geometry and the CF strength of the ligand environment around the metal ions also play crucial roles in influencing the QTM. As mentioned earlier, the Stevens-Wybourne formalism could enable one to assess the nature of anisotropy of a molecular complex. Employing this knowledge, one can design appropriate ligand environments to stabilize the highest anisotropic ground states and can suppress QTM. For example, the perturbation leading to QTM between any *Ising* doublet states can well be described by the pseudo-half spin two-state Hamiltonian for the *Ising* doublet states [7]. Any CF environment which stabilizes the axial anisotropy suppresses QTM by preventing the depletion of the magnetization moment. On the other hand, any CF perturbation (even though very small, which is the case for Ln(III) ions), which leads to off-diagonal elements in the matrix representation of the Hamiltonian, renders QTM. In addition to these, hyperfine interactions [82] and spin-dipolar interactions [131] promote QTM. Therefore, in most of the cases, in order to exclude intermolecular contribution and in order to judge the slow dynamics of magnetization of purely molecular origin, investigation on magnetically diluted sample is mandatory [132].

On the other hand, magnetization relaxation through spin-phonon coupling is temperature dependent and it can occur through several modes. The most common modes are (1) one-phonon (direct) process [133,134], (2) two-phonon Orbach process [135] and (3) two-phonon Raman process [100,133]. The temperature dependence of these processes is briefly described in the following section.

1.6.1. Temperature dependence of spin-phonon coupling relaxation

The relaxation through spin-phonon coupling involves the Zeeman-split doublet states. The one phonon (direct) relaxation is the least energetic process and is associated with the Zeeman-split doublets of *Ising* double states without involving any third excited state (blue dashed lines, Fig. 6) [133,134]. It can be proved that the rate (Λ) for the dynamics of magnetization relaxation (in other words, the inverse of the relaxation time constant, $1/\tau$) through such a process is subject to the applied magnetic field (B), temperature (T) of the system and the number of electrons (n) in the open shell of the ion [100]. For the SIMs with n = odd (*Kramers ions*), the rate can be expressed as $\Lambda(\mathrm{DK}) = 1/\tau = \tau_0 B^5\coth(\mu_0\mu_B gB/2k_BT) \approx B^4T$; and the rate for the systems with n = even *(non-Kramers ions)* is $\Lambda(\mathrm{DK}') = 1/\tau = \tau_0 B^3\coth(\mu_0\mu_B gB/2k_BT) \approx B^2T$, where τ_0 = proportionality constant; μ_B = Bohr magneton; g = g-factor of the ion; k_B = Boltzmann constant. Notably, the above final approximations for both the cases hold only when the Zeeman splitting energy ($\mu_0\mu_B gB$) is negligibly smaller than the kinetic energy ($2k_BT$). In such a circumstance, the effective phonon density of states is very small and hence, the direct process for the magnetization relaxation is inefficient. Therefore, systems tend to revert their magnetization through two-phonon relaxations.

If a system relaxes between the *Ising* doublet states (with energy E_1) via a third excited state (with energy E_2) by means of two-phonon Orbach process, the rate can be expressed as $\Lambda(\mathrm{O}) = 1/\tau = \tau'_0(U_{\mathrm{eff}})^3\exp\{-U_{\mathrm{eff}}/(k_BT)\}$. Where τ'_0 = proportionality constant; k_B = Boltzmann constant; T = temperature in absolute scale and U_{eff} = energy barrier for the magnetization reversal = $E_2 - E_1$ [135]. The Orbach process is more prone in relatively higher temperature domains, but holding the condition $E_2 - E_1 \gg k_BT$. It is evident that the above relation resembles with the Arrhenius law for the temperature dependence of rate constant, $k = A_0\exp(-\Delta E/k_BT)$ where A_0 = pre-exponential factor, ΔE = activation energy, k_B = Boltzmann constant and T = temperature in absolute scale. The ln(τ) value is linearly dependent on the inverse of temperature (1/T). The slope of such a linear plot reveals U_{eff} for the process. The temperature dependence of τ can be determined from the real (χ'_M) and imaginary (χ''_M) components of the alternating current (ac) magnetic susceptibility with the help of generalized Debye equation [136]. The magnitude of U_{eff} can be estimated from the linear regime of the ln(τ) *vs 1/T* plot by fitting with the Arrhenius equation [56]. The constant term $\tau'_0(U_{\mathrm{eff}})^3$ refers to the pre-exponential time constant and it is represented by τ_0. Smaller magnitude of τ_0 implies low rate constant, i.e. slower relaxation of magnetization.

The magnetization relaxation through a two-phonon process may also be dependent on the applied magnetic field in conjunction with the temperature (Raman process). Similar to the one-phonon direct process, the field and temperature dependence of the Raman process are subject to the number of electrons in the open shell of the ions [100,133]. The Raman process rate for the *Kramers ions* is expressed as $\Lambda(\mathrm{RK}) = 1/\tau = R_rT^9 + \alpha_B R'_r T^7B^2$ and for the *non-Kramers ion*, it is expressed as $\Lambda(\mathrm{RK}') = 1/\tau = R_rT^7$, where R_r and R'_r are the parameters dependent on the chemical systems, and α_B is a constant. However, it is noteworthy that if there are low-lying energy states in the proximity of the ground state, the powers of the temperature terms decrease and thus, markedly different magnetic dynamics are observed [137–139].

2. Overview of the reported literature

As discussed thus far, Ln(III) complexes have promise in the field of molecular magnets because of the strong SOC which arises due to the fact that the orbital angular momenta are not quenched even in the complexes. Since the regular Ln(III) complexes possess high (8–12) coordination numbers and the possibility of increasing the magnetic anisotropy is quite large in low-symmetry low-coordinate complexes there have been efforts to realize such complexes. However, stabilizing Ln(III) complexes with low coordination is a challenge in view of the large ionic radii of the Ln(III) ions. Recent research is focusing on overcoming these synthetic challenges. The status of this subject is reviewed herein. We describe complexes with coordination numbers ranging from 0 to 7. Even though the extremely low coordination compounds are not often molecular complexes they are included for the sake of completion.

2.1. Magnetic sites doped on surfaces

The maximum degree of unquenched orbital angular momentum is associated with the non-coordinated ions/atoms. Ideally, such a scenario can be possible for a free gaseous ion/atom, which, however, is of no relevance to practical applications. Moreover, in a gaseous ion/atom in the absence of external magnetic field, all the ($2J + 1$) magnetic microstates are degenerate. Even if the ion/atom is brought into a specific magnetic state, it would be extremely subtle. The total angular momentum, **J**, would interact with the environment (such as the thermal bath of electrons, nuclear spin, *etc.*) leading to the transition to the other possible magnetic states almost without requiring any energy barriers [51]. Obviously, such a system appears to be unsuitable even for investigation using the real world experimental conditions. However, doping an anisotropic paramagnetic atom/ion on a metallic surface could be an excellent approximation to such an ideal scenario. The dopant (the doped ion/atom) will interact with the surrounding atoms of the substrate (on which the atom/ion is doped) through a variety of interactions. It may be mentioned that strong orbital overlap between the dopant and the substrate atoms can render the electronic ground states of the dopant to mix with the conduction bands of the substrate, which in general leads to spontaneous electron spin relaxation [140]. Nonetheless, a proper selection of the dopant and the substrate surface can enable decoupling of the magnetization moment of the dopant atom from the conduction electrons of the substrate, and thus endowing the system with slow relaxation of magnetization [51,141]. It is also important to mention that a good orbital hybridization between the dopant and substrate atoms can lead to shorter average life-time for the magnetization relaxation [142,143]. As the lanthanides possess highly shielded *4f* valence electrons, their interactions with the transition metal atoms are very weak. Therefore, lanthanide-doped transition metal surfaces could lead to promising systems. Although these systems are not molecular, which is the theme of this article, in view of their interest and also for the sake of completion these are dealt herein.

Miyamachi et al. have recently described a system containing a Ho-doped on Pt(111) surface [51]. The Ho atoms are adsorbed on the Pt(111) surface at *fcc* and *hcp* sites with a C_{3v} local symmetry (Fig. 7). Theoretical investigation employing first-order perturbation [144] methods reveal the stabilization of the Ho ($4f^{10}$) atoms with $J = 8$. The splitting patterns and the relative energies of the magnetic eigen states (characterized by the total quantum number, J) of the Ho atoms under such an environment are portrayed in Fig. 7. Under C_{3v} symmetry, each of the doublets associated with $M_J = \pm 6$ and ± 3 undergo strong mixing and thereby leading to zero-magnetization doublet (Fig. 7). The magnetization relaxation is therefore expected to occur through the second excited state (i.e. magnetization relaxation taking place at the *Ising* doublet eigen states with $M_J = \pm 8$ *via* transition through admixed doublet eigen states with $M_J = \pm 6$) and the estimated energy barrier ΔE = 62.1 cm^{-1} (89.4 K) for *fcc* adsorption sites. The experimentally observed U_{eff} values are found to be 65 cm^{-1} (93 K) and 48 cm^{-1} (70 K) for *fcc* and *hcp* adsorption sites, respectively. More interestingly, the experimental average life-time of the magnetization moment, which is subject to the excitation energy, is found to be up to several minutes (≈12 min). However, X-ray absorption and magnetic dichroism studies in combination with CF multiplet cal-

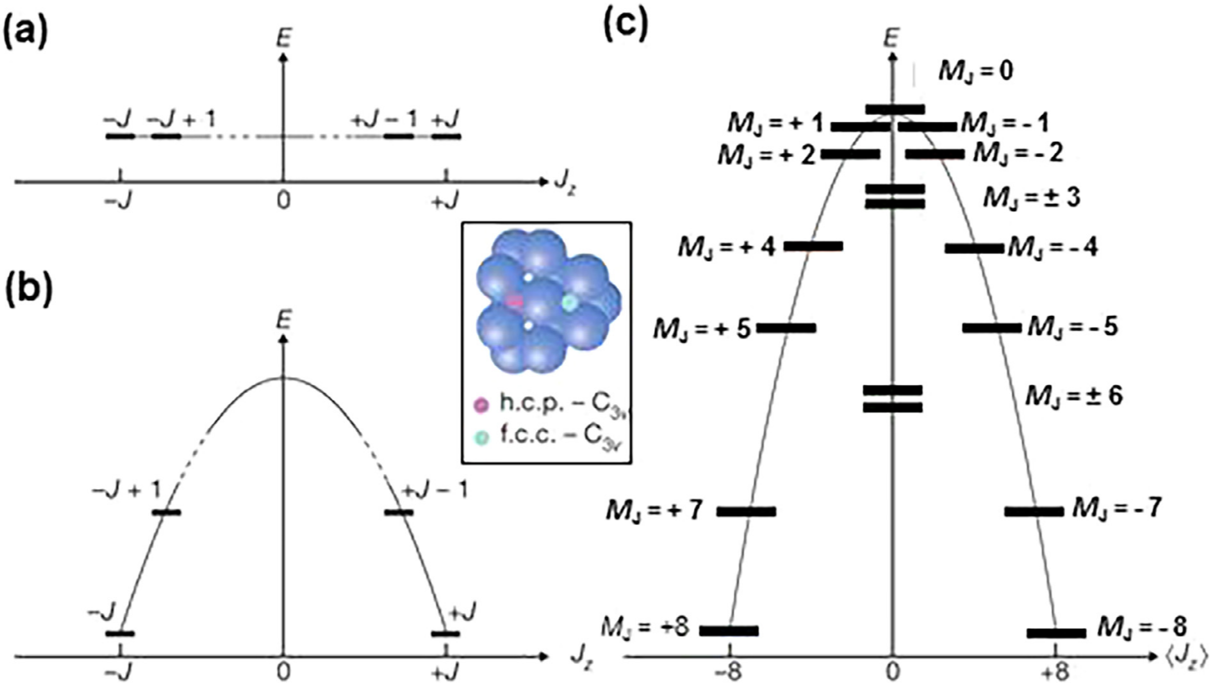

Fig. 7. Magnetic eigen states of Ln atoms characterized by well-defined total quantum number *J*. (a) Degenerate eigen states of a free atom; (b) Lifting of degeneracy of the eigen states due to uniaxial anisotropy; (c) The energy landscape of the *Ising* doublet eigen states for a system with $J = 8$ under C_{3v} point group symmetry. The inset depicts the *fcc* and *hcp* adsorption sites. Figure and captions are reprinted from the Ref. [51] with permission from Nature Publishing Group.

culations carried out by Donati et al. indicate that such a long average time for the system is unlikely [145–148].

In a related study it was shown that very interesting magnetic behaviour was exhibited by the Ho atoms when adsorbed on a MgO(100) surface that is grown on Ag(100) [145,146]. In this case, the Ho atoms experience a C_{4v} point group symmetric CF perturbation and there exists a very weak orbital overlap between Ho and substrate atoms. This leads to admixing of the *Ising* doublet eigen states with odd M_J values ($M_J = \pm7, \pm3, \mp1$ and ∓5; arranged energetically in an ascending order) resulting in a degenerate ground doublet. The first excited state was found for $M_J = 0$ which is separated by around 36 cm^{-1} from the ground doublet (Fig. 8). Due to such a large energy gap, the Zeeman-split eigen states do not mix with the higher energy states up to as high as 10 T magnetic fields. Therefore, the ground state magnetization is protected from QTM within such a large window of magnetic fields. The magnetic hysteresis loop was studied after saturation of ground state population under an external magnetic field of 6.8 T. Further investigations revealed a step-less hysteresis loop (Fig. 8) with large coercive field at 10 K at a field sweep rate of 80 Oe/s. The average lifetime of the magnetization remnance is remarkable (around 25 min). Interestingly, the magnetization relaxation is found to be temperature-independent within the 10–2.5 K window. The relaxation is found to be temperature dependent above 10 K and the magnetization hysteresis loops were observed up to 30 K at the same field sweep rate. It is worth pointing that, the slow dynamics of magnetization was dependent on the thickness of the substrate MgO layers. Dy atoms adsorbed on graphene deposited over Ir(111) surfaces,

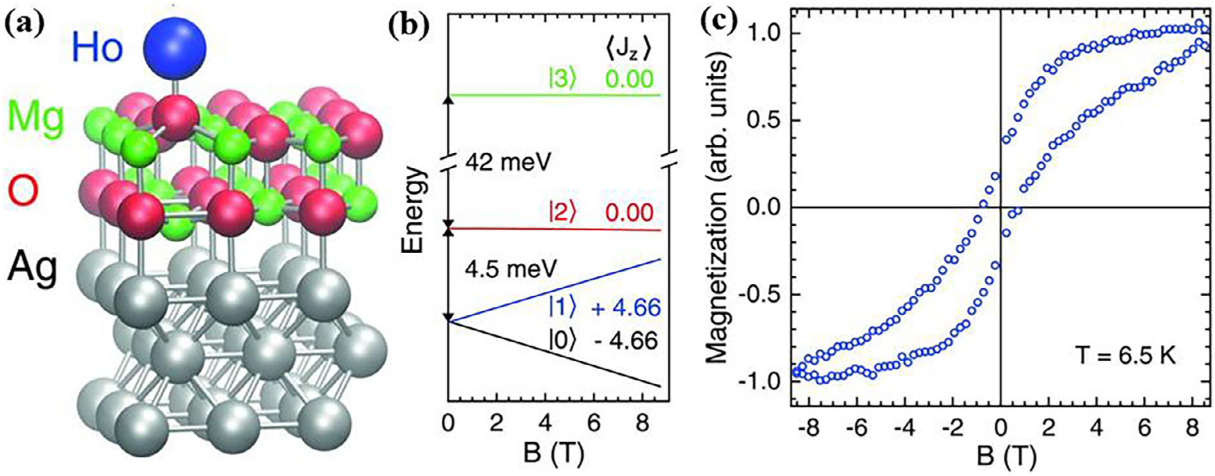

Fig. 8. (a) The DFT simulated geometry of the adsorption sites of the Ho atoms on top of O on 2-mono layer (ML) MgO/Ag(100); (b) The relative energy of the low-lying electronic states in combination with Zeeman splitting; (c) The magnetic hysteresis loop at 6.5 K with a field sweep rate of 80 Oe/s. Figure and captions are reprinted from the Ref. [145] with permission from The American Association for the Advancement of Science.

Table 3
Magnetic parameters of the doped atoms/ions on substrate surface.

Ln(*J*)	Substrate	Symmetry*	ΔE(theo) (cm^{-1})†	Hysteresis	Sweep rate (Oe/s)	τ (m) (Temp; K)	Refs.
Ho(*J* = 8)	Pt(111)	C_{3v}	62.1 (*fcc*)	–	–	≈12 (2.5–10)	[51]
Ho(*J* = 8)	MgO(100)/Ag(100) (2-ML)	C_{4v}	36	Yes	80	25 (10)	[145]
Dy (*J* = 8)	Graphene/Ir(111)	C_{6v}	45.2(H_{dc}=0) 172.6($H_{dc}\neq$0)	Yes	33	≈16 (2.5)	[148]
Dy (*J* = 8)	Ir(111) Graphene/Ru(0001)	–	–	No No	–	–	[148]
Dy (*J* = 8)	*h*-BN(111)/Ir(111)	C_{3v}	Ground J_z = 0	No	–	–	[148]
Dy(III) (J = 15/2)	SiO_2	C_1	–	Yes	16	–	[149]

[*] The point group symmetry around the doped atoms.
[†] The most probable excitation energy for magnetisation reversal.

where the Dy atoms experience C_{6v} CF point group symmetry, also exhibit promising magnetic hysteresis loops but with relatively lower average life-time (Table 3) [148]. Although limited, these examples reveal that such approaches can be a way forward to realize practical applications. Table 3 summarizes the magnetic properties of systems involving lanthanide atoms doped on a surface.

Another way of stabilizing the low-coordinate Ln atom/ion is to trap them in the interior of fullerenes [150–152]. Though, it is difficult to generalize the coordination number for these endohedral metallo-fullerenes (EMFs), the nature of fullerene(C)-Ln(III) interactions are found to be very weak. Therefore, for the sake of simplicity, we are considering only the atoms which are coordinated to the Ln(III) ions, neglecting the coordination contribution from the fullerene ring.

Based on this assumption, trapping the Ln ion(s) inside the cages can be considered a way to achieve the zero-coordinate condition around Ln ion. It is also worth mentioning that in these EMFs, it is possible to avoid atoms possessing nuclear spin (such N and H for example) and therefore the hyperfine relaxation due to the ligands can be avoided. Besides, the cages are often rigid, which leads to larger vibrations and reduces the possibility of other non-Orbach relaxation channels. As the synthesis of EMFs are often challenging, *ab initio* calculations coupled with DFT methods can be a useful tool to predict target molecules of potential interest. In this regard, it is worth to mention here that theoretical studies

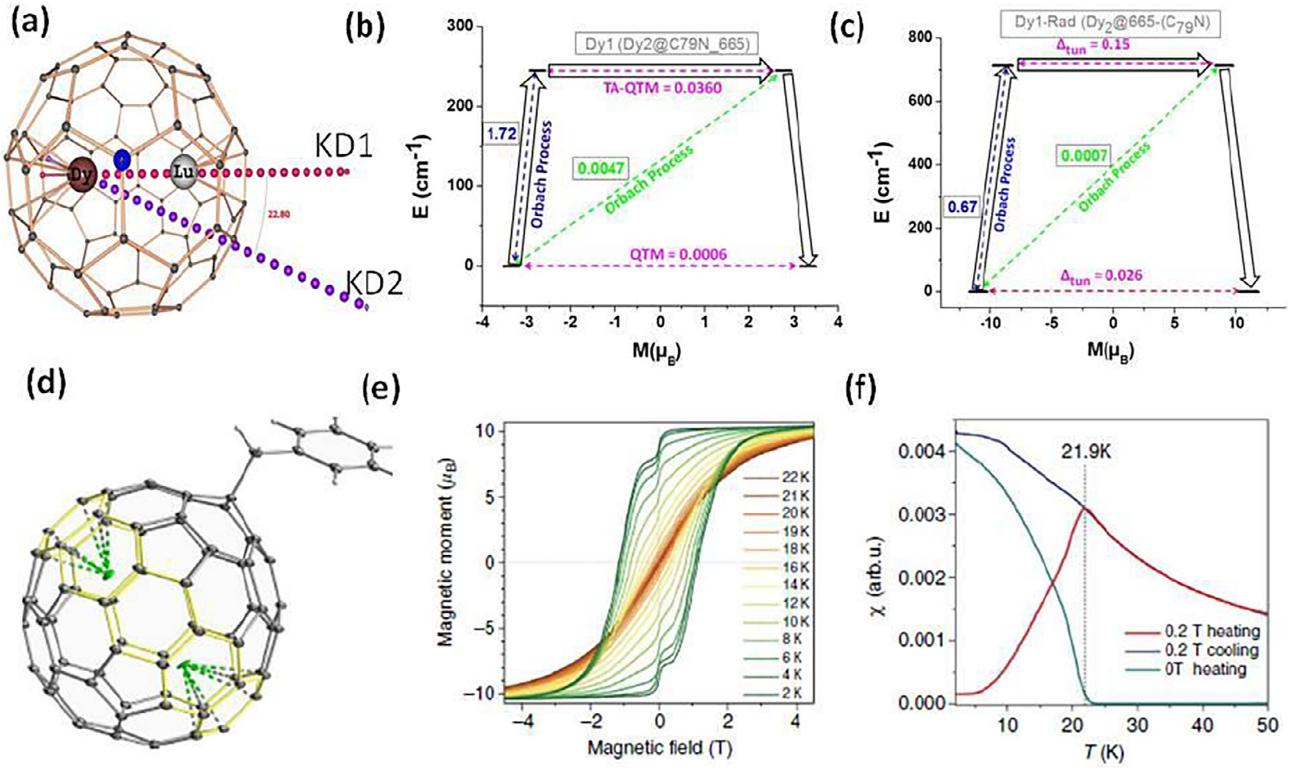

Fig. 9. (a) Molecular structure of DyLu@C_{79}N along with their ground and first excited KD magnetic axis. (b) *ab initio* SINGLE_ANISO computed magnetization blockade barrier for the Dy1 ion; (c) *ab initio* POLY_ANISO computed magnetization blockade barrier for Dy1–radical exchange coupled systems for the DyLu@665-(C79N) model; (d) X-ray structure of $Dy_2@C_{80}(CH_2Ph)$ reported by Popov and co-workers; (e) magnetization curves measured at various temperatures with the field sweep rate of 2.9 mT s^{-1} and (f) plot showing blocking temperature measurement. In (b–c) the x-axis indicates the magnetic moment of each state along the main magnetic axis while the y-axis denotes the energy of the respective states. The thick black lines imply Kramer's doublet as a function of magnetic moment. The dotted green and blue lines indicate the possible pathway of the Orbach/Raman contribution of magnetic relaxation. The hollow black arrows indicate the most probable relaxation pathway for the magnetization reorientation. The dotted red lines correspond to the QTM/TA-QTM/tunnelling relaxation contributions between the connecting pairs. The numbers provided at each arrow are the mean value for the corresponding matrix element of the magnetic moment. Figure (a–c) and captions are reprinted from the Ref. [153] with permission from Royal Society of Chemistry. Figure (d–f) and captions are reprinted from the Ref. [154] with permission from Nature Publishing Group.

performed on {DyLu@C$_{79}$N}$^+$ suggest relaxation via first excited state with a calculated effective energy barrier (U_{cal}) of 244 cm^{-1} (Fig. 9a-b) [153]. However for a radical fullerene cage such as {DyLu@C$_{79}$N}, very large magnetic exchange coupling (286 cm^{-1}) between Dy-radical(hetero-fullerene) are found boosting the U_{cal} value to 711 cm^{-1} (Fig. 9c). Recently, Popov and co-workers have synthesized Dy$_2$@C$_{80}$(CH$_2$Ph) EMF possessing very strong exchange coupling between Dy(III) and radical fullerene cage leading to a U_{eff} value as high as 426 cm^{-1} and a reported blocking temperature of 18 K [154]. Hetero-fullerenes are expected to have larger magnetic exchange constant value because of localization of the unpaired cage- electron between lanthanide ions and are expected to show even higher U_{eff} values.

Notably, doping/grafting of the Ln atoms/ions on non-magnetic surfaces provides not only the opportunity of exploiting the magnetic behaviour of the magnetic sites under very weak CF environments, but it also renders complete isolation (magnetic dilution, in other words) of the magnetic sites. Recently, Coperét and co-workers investigated the magnetic behaviour of Dy(III) ion grafted on the surface of SiO$_2$ nanoparticles [149]. The Dy(III) ions were grafted on SiO$_2$ surfaces through two-step process starting from the molecular complex [Dy(OSi(O^{t}Bu)$_3$)$_3$(κ^2-HOSi(O^{t}Bu)$_3$] (**[L′L$_3$-Dy]**; Fig. 10) where the ligands are kinetically labile. EXAFS studies revealed that the Dy(III) ions in both **[L′L$_2$Dy]/SiO$_2$** and **Dy@SiO$_2$** incorporate pentacoordination with non-centrosymmetric coordination geometry (Fig. 10) [149].

Interestingly, the molecular complex **[L′L$_3$Dy]** does not exhibit slow relaxation of magnetization. On the other hand, **[L′L$_2$Dy]/SiO$_2$** and **Dy@SiO$_2$** are found to exhibit slow relaxation of magnetization. While, **Dy@SiO$_2$** displays distinct openings in the magnetization hysteresis loops at zero-field up to 5 K, the magnetization hysteresis loop for **[L′L$_2$Dy]/SiO$_2$** remains closed at zero-field even at the lowest temperature (Fig. 10). Slow relaxation of magnetization in **[L′L$_2$Dy]/SiO$_2$** and **Dy@SiO$_2$** in contrast to **[L′L$_3$Dy]** certainly stems from magnetic dilution (magnetic site isolation upon grafting on SiO$_2$ surface). Observation of the openings in the magnetization hysteresis loops at zero-field for **Dy@SiO$_2$** in contrast to **[L′L$_2$Dy]/SiO$_2$** could be attributed to the distortion in coordination geometry and the change in CF symmetry.

2.2. Hepta-coordinate lanthanide complexes

The most commonly observed coordination geometries for the hepta-coordinate Ln(III) complexes are the pentagonal bipyramid (PBP) [46–48,54,155] and the capped-octahedron [45,50,156–158]. In view of point charge of the ligating sites, several point group symmetries may associate with a given coordination geometry (*eg.* D_{5h}, C_{2v}, C_{5v} *etc.* for PBP). However, D_{5h} is the highest possible CF point group symmetry for the PBP coordination geometries. As depicted in Fig. 11(*top*) for the hypothetical [DyF$_7$]$^{4-}$ species, the energy landscape of J = 15/2 manifold for the Dy^{3+} ion under D_{5h} CF point group symmetry incorporates well-isolated

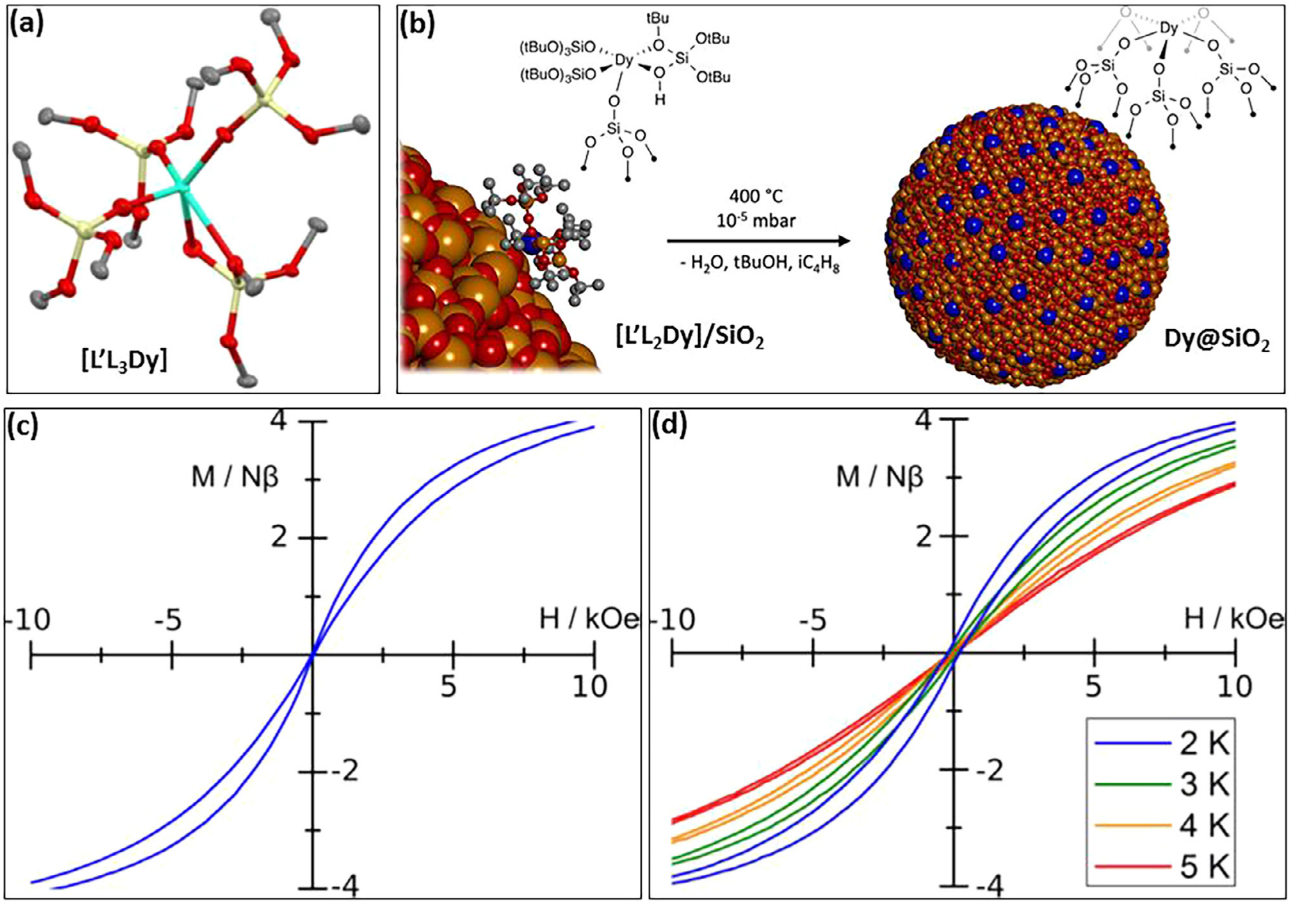

Fig. 10. (a) Molecular structure of **[L′L$_3$Dy]**. H atoms are omitted for clarity. Colour codes: grey: C; red: O; yellow: Si; and cyan: Dy. (b) Schematic representations for **[L′L$_2$Dy]/SiO$_2$** and **Dy@SiO$_2$** along with the synthetic scheme of the later starting from the former. (c) Magnetization hysteresis loop for **[L′L$_2$Dy]/SiO$_2$** at dc field sweep rate = 16 Oe/S at 2 K. (d) Magnetization hysteresis loops for **Dy@SiO$_2$** at dc field sweep rate = 16 Oe/S in 2–5 K temperature range. The figures and captions are reprinted from the Ref. [149] with permissions from the American Chemical Society 2017 copyright Act.

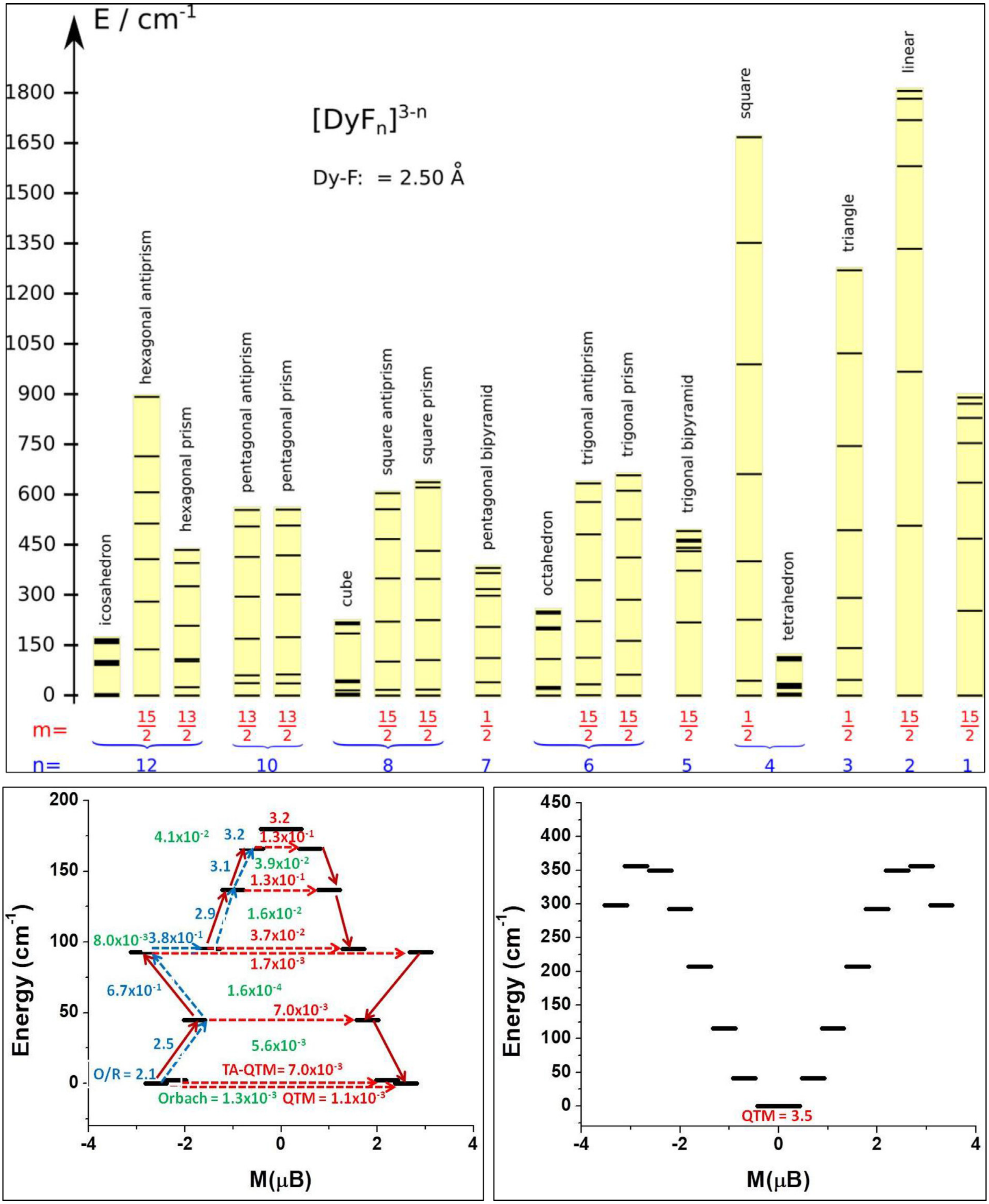

Fig. 11. *Top:* Relative eigen values of the *Ising* double eigenstates of the ground state $J = 15/2$ manifolds for Dy(III) ion in hypothetical $[DyF_n]^{3-n}$ species under different possible coordination geometries, where n stands the coordination numbers ranging from 1 to 12. M_J corresponds to the projection of the total angular momentum $J = 15/2$ on the magnetic anisotropy axis associated with the lowest energy *Ising* doublet eigen state. The eigen values were obtained from *ab initio* calculations for arbitrarily fixed Dy-F distance = 2.50 Å. Figure and captions are reprinted with permission from the Ref. [21]. Copyright @ 2016, American Chemical Society. *Bottom: Ab initio* SINGLE-ANISO computed magnetization blockade barrier for PBP $\{Er(OH)_7\}^{4-}$ (left) and $\{Dy(OH)_7\}^{4-}$ (right) models. Plotted from the data given in Ref. [115].

doublets and all the doublet eigen states are almost uniaxial for the Kramers ions [21,159]. Therefore, U_{eff} is expected to be almost equal to the height of the energy landscapes. *Ab initio* calculations performed by some of us on pentagonal bipyramidal $\{Er(OH)_7\}^{4-}$ and $\{Dy(OH)_7\}^{4-}$ models with equal Dy-O bond distances (2.35 Å) [115] suggest relaxation via sixth excited KD for the former with U_{cal} value 166 cm^{-1}. Whereas, extensive QTM for the latter is seen in the ground state (Fig. 11). $\{Er(OH)_7\}^{4-}$ model has strong transverse ligand field. Because of the two axial components of the ligand field, relaxation is not occurring via highest excited state but through sixth excited state, QTM has been suppressed up to higher excited state. Orbach relaxation representing off-diagonal elements are also found to be very small up to highest possible excited state.

The first four KDs are purely Ising in nature and next two KDs are strongly axial in nature suggesting relaxation via sixth excited state through TA-QTM. In $\{Dy(OH)_7\}^{4-}$ model, the transverse ligand field is large enough to cause relaxation via ground state. To overcome this in pentagonal bipyramidal complexes, weak transverse ligand field in conjunction with strong axial ligand field strength is needed to minimize the electronic repulsion between the f-orbital electrons and ligand field electrons. Kazin and co-workers have isolated $\{DyO\}^+$ ions in an apatite matrix with the nominal composition $M_{10-x}Dy_x(PO_4)_6(OH_{1-x/2})_2$, where M = Ca, x = 0.5 (**5**), x = 1 (**6**), M = Sr, x = 0.1 (**7**), x = 0.2 (**8**) [160]. Although here $\{DyO\}^+$ is incorporated in the lattice, the Dy(III) ion also interacts with the lattice oxygen forming a seven coordinated Dy(III) complex. Experimental U_{eff} values for these systems are found to be 792 cm^{-1}, 784 cm^{-1}, 1025 cm^{-1} and 1043 cm^{-1} for **5**–**8**, respectively, with blocking barriers up to 11 K for **7**. SHAPE analysis suggests a distorted pentagonal bipyramidal geometry for Dy(III) centre. One of the Dy-O bonds is found to be very short compared to other Dy-O bonds, providing strong axial ligand field and causing the relaxation to occur via fourth excited state (Fig. 12).

Notably, unlike transition metal ions, chelating ligands are not a prerequisite for the stabilization of Ln(III) ions in the PBP geometry. Even, seven mono-dentate ligands can render PBP geometries around Ln(III) ions (Fig. 13). Considering all the coordinating oxygen atoms around the Ln(III) ions point-charge-wise identical in $[Dy(Cy_3PO)_2(H_2O)_5]Cl_3{\cdot}(Cy_3PO){\cdot}H_2O{\cdot}EtOH$ (**2**) [48], $[Dy(Cy_3PO)_2(H_2O)_5]Br_3{\cdot}2(Cy_3PO){\cdot}2H_2O{\cdot}2EtOH$ (**3**) [48], $[Zn_2DyL_2(MeOH)]$ (**9**) [54] and $[L_2Nd(H_2O)_5][I]_3{\cdot}2L{\cdot}H_2O$ (L = $^tBuPO(NH^iPr)_2$; **10**) [47], the CF point group symmetry around these metal ions can be considered as D_{5h} (Fig. 13).

The energy landscapes of *J* manifold for Dy(III) in **2** and **3** are depicted in Fig. 14. The difference in topology of the energy landscapes in **2** and **3** compared to $[DyF_7]^{4-}$ species stems from the CF asymmetry induced by the presence of H-bonded Cy_3PO moieties in the second coordination sphere of the former. However, in the case of **2**, the Zeeman eigen states corresponding to the ground and first excited doublets are well separated. But the admixing of the second excited doublet eigen states is so strong that it leads to almost zero-magnetization doublet and in turn opening the gate here for the magnetization reversal. But in the case of **3**, such strong admixing is noticed for the first excited states which are energetically at close proximity to the second excited doublet.

Interestingly, the transition matrix element for the ground and second excited doublet (1.7) is much larger than the ground and first excited doublet (0.3). Therefore, for both the cases, the magnetization reversal is expected to occur effectively through the second excited state (ΔE = 368 and 278 cm^{-1} for **2** and **3**, respectively) which supports the experimentally observed effective energy barriers for magnetization reversal (U_{eff} = 328 and 377.4

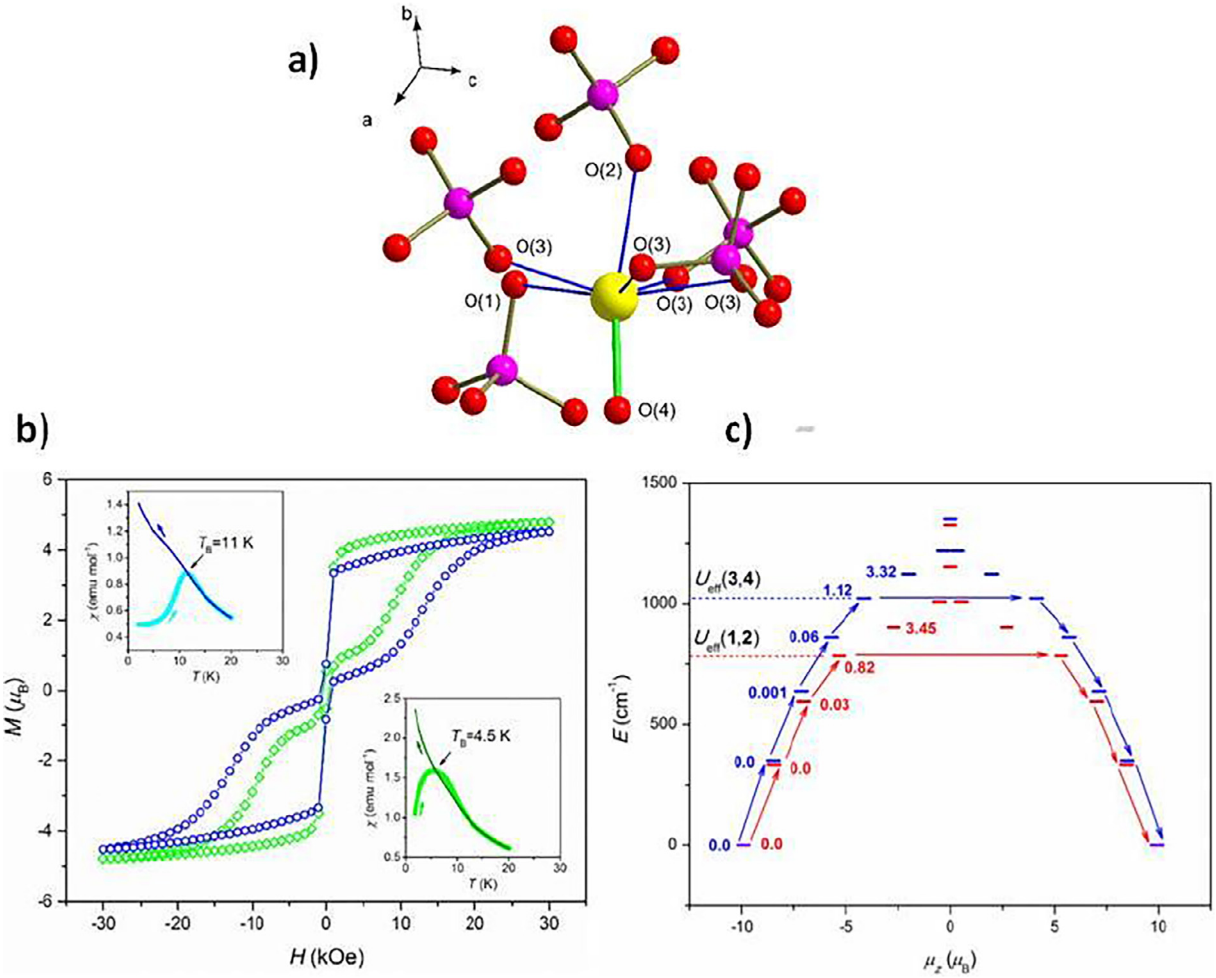

Fig. 12. (a) X-ray structure the fragment of the molecule; (b) Magnetization *vs.* magnetic field at 1.8 K and (c) modelled magnetization blockade diagram. Figure and captions are reprinted from the Ref. [160] with permission from John Wiley and sons.

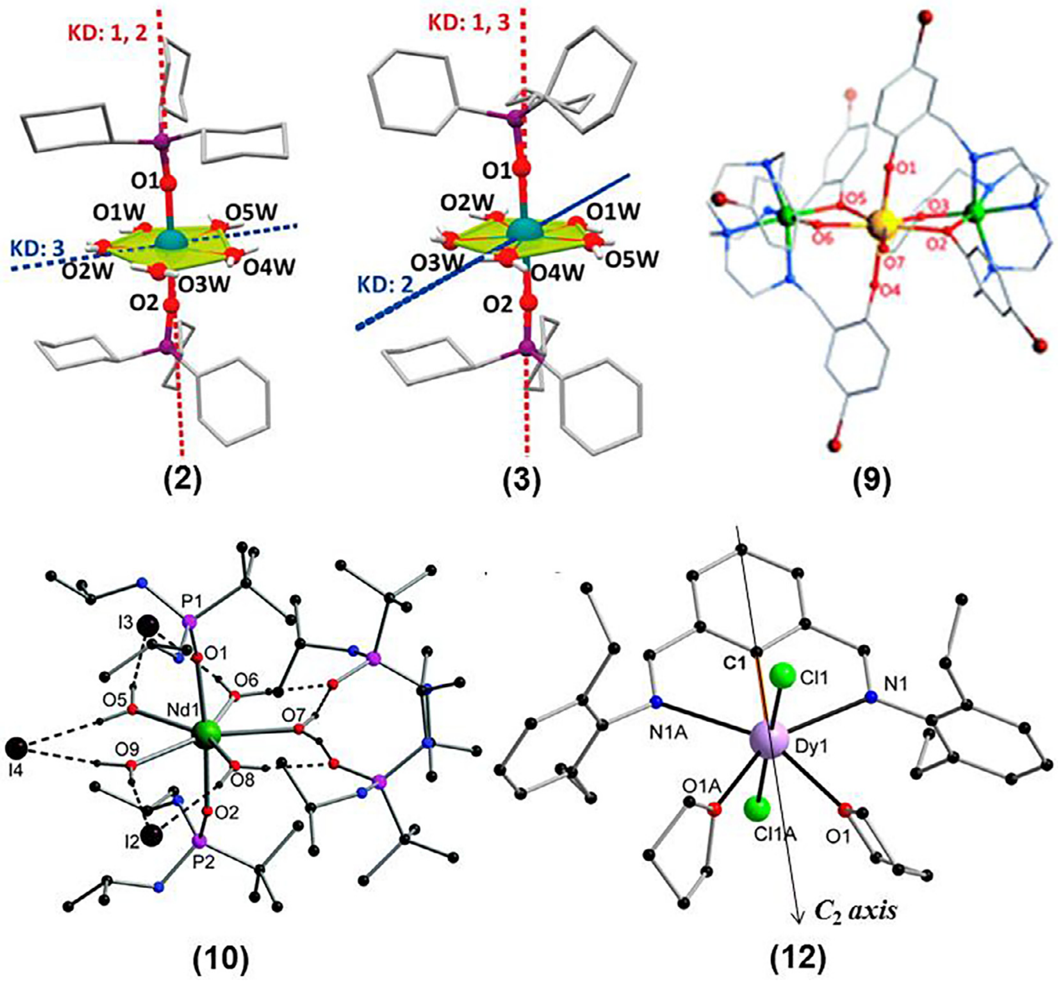

Fig. 13. Single-crystal X-ray structures of **2**, **3**, **9**, **10**, **12**. Only the first coordination spheres are shown for **2** and **3**. H atoms are omitted for clarity. The red and blue dotted lines in **2** and **3** indicate anisotropy axes of the labelled Kramers doublets (KD). The black solid arrow in **12** represents the C_2 axis. Figure and captions are reprinted from the Refs. [47,54] with permission from Royal Society of Chemistry, the Ref. [48]; Copyright @ 2016, American Chemical Society, and the Ref. [155] with permission from Nature Publishing Group.

cm^{-1}, respectively). In the case of **9**, the U_{eff} determined from ac magnetic susceptibility studies is found to be 305 cm^{-1}, which agrees reasonably well with the theoretical energy barriers for the magnetization reversal occurring through the second excited states (ΔE = 303.3 cm^{-1} calculated for **9** and 302.6 cm^{-1} calculated for a hypothetical $[Dy(H_2O)_7]^{3+}$ (**11**) species in D_{5h} CF point group symmetry). Overestimation of theoretical effective energy barrier owing to ignoring the second coordination sphere can be realized by considering the magnetic data for **10** (Fig. 13). *Ab initio* calculations for **10** considering D_{5h} CF point group symmetry predicts magnetization reversal to occur through the first excited state situated above 209.9 cm^{-1} from the ground state. But, the ac magnetic susceptibility studies revealed U_{eff} = 17.2 cm^{-1} under zero-field and 27.2 cm^{-1} under an applied magnetic field 2 kOe. It is worth remembering that, in addition to such symmetry omission, theoretical calculations also put aside the intermolecular spin-dipole interactions, nuclear-spin coupling, crystallographic temperature for generating geometric parameters, *etc.* which sometimes render the theoretical predictions noticeably different. Exhibition of markedly higher effective energy barrier for magnetization reversal by Dy(III) ion in D_{5h} coordination CF compared to its Nd(III) analogue could be attributed to the difference in the angular charge distributions of the *4f*-electrons. In comparison to Dy(III) ion, Nd(III) ion bears more diffused *4f*-electronic charge on the equatorial plane of the oblate-like electrostatic potential surface corresponding to the *Ising*-limit eigenstates ($M_J = \pm 9/2$) [33,94]. Therefore, stronger CF strengths operating on the equatorial plane of the coordination geometry with D_{5h} symmetry is expected to render destabilization of *Ising*-limit eigenstates for the Nd(III) ion.

The pentagonal bipyramidal coordination geometry of [DyNCN] [155] (NCN = $[2,6\text{-}(2,6\text{-}C_6H_3R_2N{=}CH)_2\text{-}C_6H_3]^-$; a pincer ligand) (**12**) belongs to the C_{2v} CF point group symmetry and the theoretical energy landscape of the *J* manifold is as portrayed in Fig. 14. The magnetization reversal is expected to occur through the second excited state requiring an energy barrier of 262 cm^{-1}. The experimentally observed zero-field U_{eff} values (233 cm^{-1} for the net polycrystalline solid samples and 270 cm^{-1} for magnetically diluted samples (Dy/Lu = 1/19 by population)) agree very well with the theoretical prediction. However, it is noteworthy that ground state electron distribution around Dy(III) is oblate in nature and hence, it prefers strong axial and weak equatorial ligand fields [33]. The evidence of such a preference can be demonstrated with the PBP complexes [Dy(bbpen)X] (X = Cl; **13** and Br; **14**) [46]. The coordination environments around Dy(III) ion in both the complexes associate with C_{2v} point group symmetry (Fig. 15). The experimentally determined zero-field U_{eff} values are found to be 492 cm^{-1} for **13** and 712 cm^{-1} (828 cm^{-1} for magnetically diluted samples; Dy/Y $\approx$ 1/20) for **14**. Such a remarkable difference in comparison to **12** can be attributed to weak-field halides on the equatorial planes and strong-field alkoxy oxygens in the axial positions

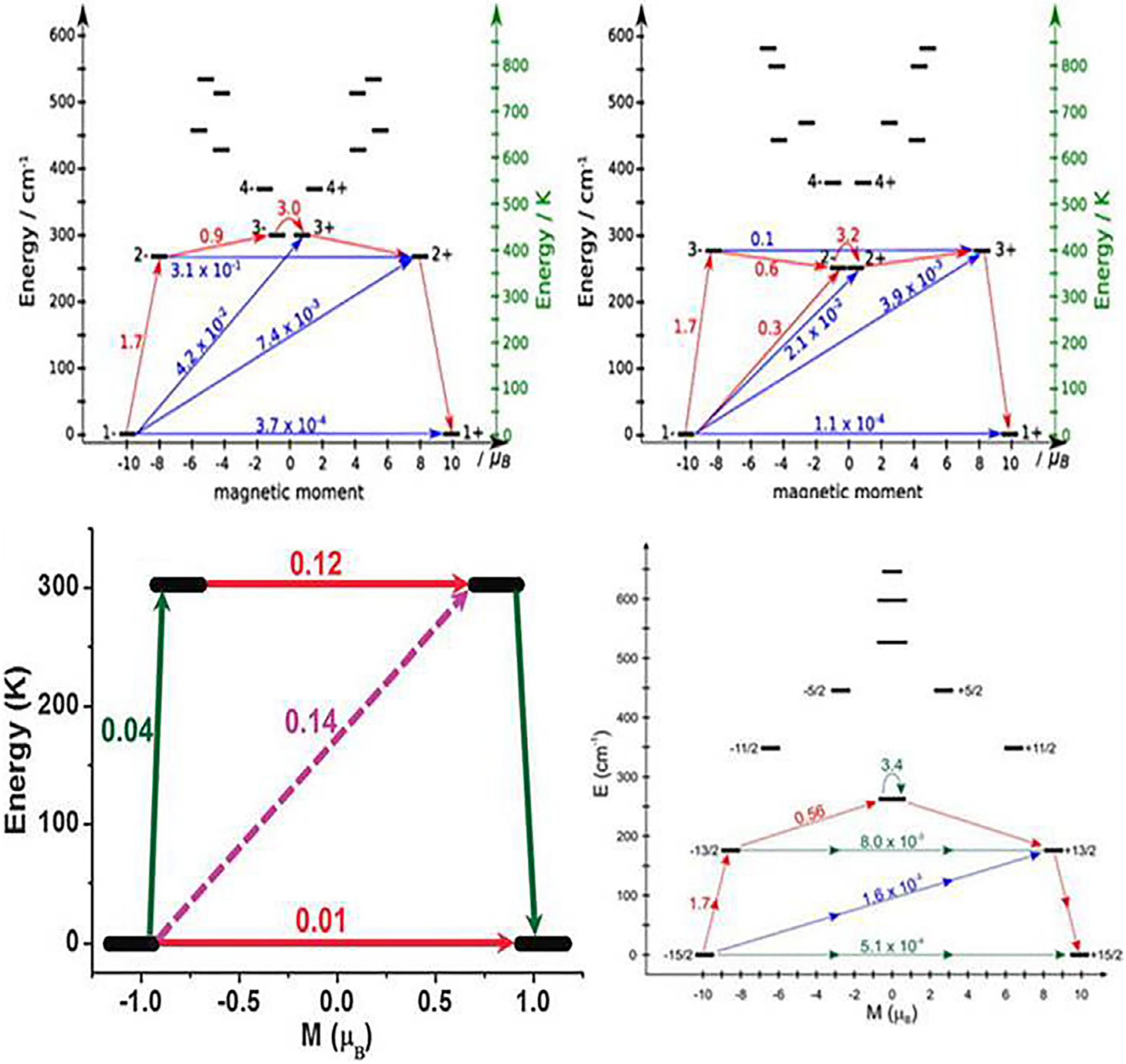

Fig. 14. The *ab inito* calculated low-lying energy levels for **2** (upper left), **3** (upper right), **10** (lower left) and **12** (lower right). The bold horizontal black lines depict the relative energy of the eigen states of the ground *J* manifolds. The values indicated on the arrows are the transition matrix elements associated with the connected eigen states. Magnetization reversals via Orbach mechanism involves the paths marked by the red arrows. Figure and captions are reprinted with permissions from the Ref. [48]; Copyright @ 2016, American Chemical Society, the Ref. [47] with permission from Royal Society of Chemistry, and the Ref. [155] with permission from Nature Publishing Group.

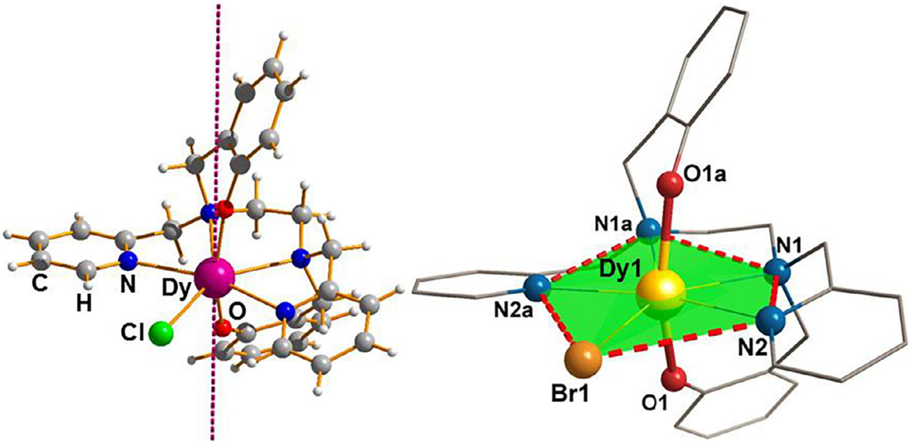

Fig. 15. The single crystal X-ray structures of the complexes **13** (left) and **14** (right). The purple dotted line represents the anisotropy axis. The equatorial plane around the Dy atoms is indicated by the green plane. Figure and captions are reprinted with permission from the Ref. [46]. Copyright @ 2016, American Chemical Society.

Table 4
Magnetic parameters of the hexa- and hepta-coordinate Ln(III) SIMs.

Complex (No.)	U_{cal}(theo) (cm^{-1})†	U_{eff} (cm^{-1}) (H_{dc}; Oe)*	Hysteresis	T_B(K)‡	Refs.
$[Dy(Cy_3PO)_2(H_2O)_5]Cl_3{\cdot}(Cy_3PO){\cdot}H_2O{\cdot}EtOH$ (**2**)	368	328 (0)321.1 (1000)	Yes	11 (200 Oe/s)	[48]
$[Dy(Cy_3PO)_2(H_2O)_5]Br_3{\cdot}2(Cy_3PO){\cdot}2H_2O{\cdot}2EtOH$ (**3**)	378	377.4(0)	Yes	20 (200 Oe/s)	[48]
$[Zn_2DyL_2(MeOH)]$ (**9**)	289.9	305 (0)	Yes	11 (20 Oe/s)	[54]
$[L_2Nd(H_2O)_5][I]_3{\cdot}2L{\cdot}H_2O$ (**10**)	209.9	17.2 (0)27.2 (2000)	–	–	[47]
(DyNCN) (**12**)	262	233270 (0; dil.)	Yes	–	[155]
[Dy(bbpen)Cl] (**13**)	586	492 (0)	Yes	7.5 (1 kOe)8 (20 Oe/s)10 (20 Oe/s; dil.)	[46]
[Dy(bbpen)Br] (**14**)	721	712 (0)828 (0; dil.)	Yes	9.5 (1 kOe)14 (20 Oe/s)	[46]
$[Dy(O^tBu)_2(py)_5][BPh_4]$ (**15**)	1220	1261 (0)	Yes	14 (2 kOe)8.8 (12 Oe/s)	[69]
$(Et_3NH)[(H_2LDyCl_2]$ (**16**)	–	48.6 (500; dil)	–	–	[161]
[Dy(trensal)] (**17**)	50	7 (900)	No	–	[50]
[Er(trensal)] (**18**)	54	22 (800)	No	–	[50]
$[Dy(EIFD)(H_2O)]{\cdot}CH_2Cl_2$ (**19**)	–	39.4 (0)	Yes	–	[158]
$[Dy(BIPM^{TMS})_2][K(18C6)(THF)_2]$ (**23**)	515.7 562.9	501.1 (0)565 (0)	Yes	10 (1 kOe)10 (35 Oe/s)12 (100 s)	[55]
$[Zn_2DyL_2]$ (**24**)	294.8	–	Yes	–	[54]
$[Yb(H_3L)_2]Cl_3{\cdot}5CH_3OH{\cdot}2H_2O$ (**25**)	~160		No		[164]

† The most probable theoretical excitation energy for magnetisation reversal.
* Experimentally observed energy barrier for magnetization reversal.
‡ The blocking temperature expressed through ZFC susceptibility at H_{dc} (kOe), or/and hysteresis at ΔH (Oe/s) or/and average life-timeτ (s) study.

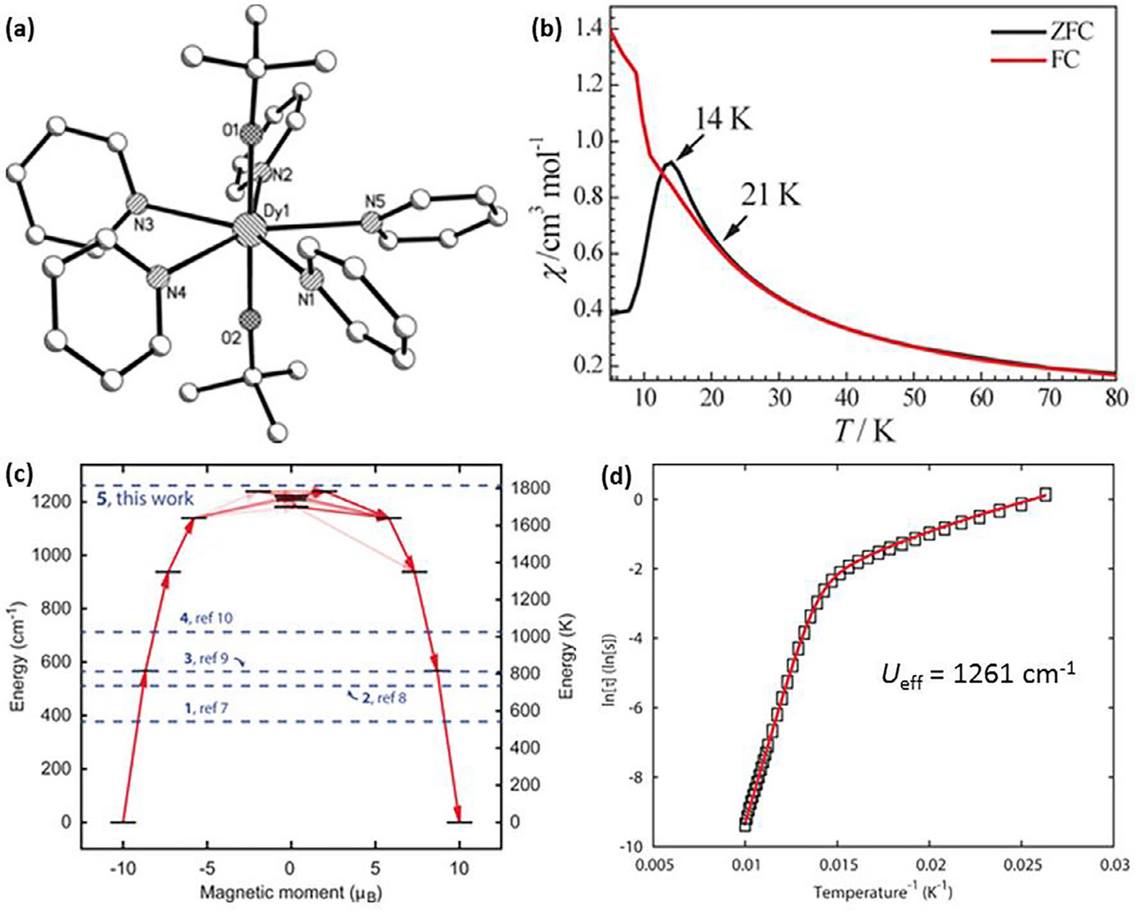

Fig. 16. The single crystal X-ray structure (a), (b), *ab initio* calculated energy landscape for the ground *J* manifold (c) and the temperature dependent relaxation time constants (τ; open black squares) with the best fit (solid red line) under zero dc field (d) of the complex **15.** Figure and captions are reprinted from the Ref. [69] with permission from John Wiley and sons.

for **13** and **14**. Moreover, Br causes weaker CF in the equatorial plane than Cl and thus, larger U_{eff} is expected for the former analogue. It is worth pointing out that all the above complexes with PBP geometry exhibit magnetic hysteresis loops with low-to-moderate coercive field (Table 4).

As the Dy(III) ion possesses oblate electrostatic potential surfaces in the ground eigen states, the seven coordinated complexes with PBP coordination geometry that render weaker equatorial and stronger axial CF are expected to exhibit better magnetization dynamics. Zheng, Winpenny, Chilton and co-workers investigated in detail the magnetic property of $[Dy(O^tBu)_2(py)_5][BPh_4]$ (**15**) where the heptacoordinated Dy(III) ion associates with five pyridyl N atoms in the pentagonal equatorial plane and with two alkoxy O atoms in the axial coordination sites (Fig. 16) [69]. The dc magnetic susceptibility measurement revealed room temperature $\chi_M T$ product to be 14.10 $cm^3\,K\,mol^{-1}$, as expected (14.17 $cm^3\,K\,mol^{-1}$) for a magnetically exchange-free Dy(III) ion [69]. The ZFC-FC susceptibility study (under 2 kOe dc field) indicated the magnetization blocking temperature (T_B) around 14 K (Fig. 16). Detailed *ab initio* (CASSCF-SO) calculations predicted that the low-lying KDs with relative energies 0, 564, 940 and 1141 cm^{-1} are constituted by the eigen doublets with almost pure $M_J = \pm15/2$, $\pm13/2$, $\pm11/2$ and $\pm 9/2$, respectively. The subsequent states are admixed to form a bunch of narrowly spaced energy states above around 1183–1237 cm^{-1} (Fig. 16) and the most probable relaxation of the magnetization is predicted to occur through theses bunch of energy states ($U_{eff} \approx 1220\ cm^{-1}$). Detailed ac magnetic susceptibility studies on the polycrystalline solid samples of **15** displayed out-of-phase ac susceptibility maximum up to 100 K at 1.5 kHz ac frequency under zero dc field. Analysis of the temperature dependent relaxation time constants ($\ln\tau$ *vs* $1/T$) showed a linear regime within 67–100 K (Fig. 16). The best fit to the whole temperature domains resulted out U_{eff} = 1261 cm^{-1} with $\tau_0 = 1.17(6) \times 10^{-12}$ s, which agrees well with the theoretical prediction. Notably, in spite of such a high U_{eff}, the openings in the magnetic hysteresis loops at zero-field are found only up to around 8.8 K for **15** [69]. The alkoxy O is moderately strong CF donor. Employment of stronger CF donors, such as cyanide, phosphine oxides, *etc.* could suppress QTM more and thereby could result in higher blocking temperature.

So far we have come across pentagonal bipyramid (PBP) complexes with various ligand environments. The complexes with

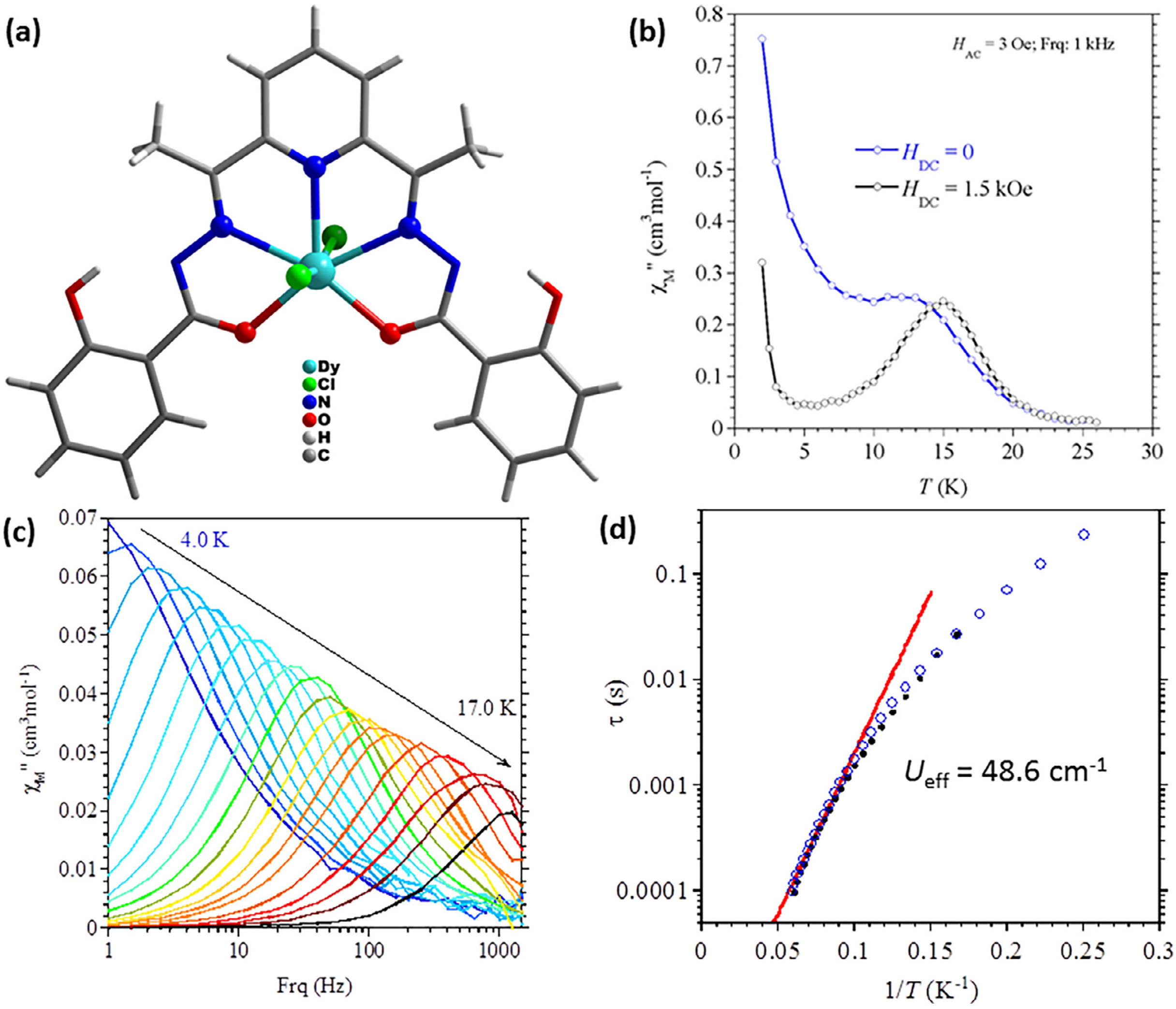

Fig. 17. (a) The single crystal X-ray structure of the **16**. (b) The temperature dependent *out-of-phase* ac susceptibilities (open circles) of the polycrystalline neat sample of **16** under H_{dc} = zero (blue) and 1.5 kOe at 1 kHz ac frequency. The solid lines are eye-guides only. (c) The variable temperature frequency dependent *out-of-phase* ac susceptibilities (χ''_M, solid dots) for the magnetically diluted samples of the Y(III) analogue with 5% Dy(III) site populations under H_{dc} = 500 Oe. The solid lines are eye-guides only. (d) The temperature dependent relaxation time constants (τ; open blue circles: magnetically diluted sample; solid black circles: neat sample) with the best fit (solid red line) under dc fields (H_{dc} = 1.5 kOe for the neat sample and 500 Oe for the diluted sample). Figure and captions are reprinted from the Ref. [161] with permissions. Copyright @ 2018, American Chemical Society.

weaker equatorial and stronger axial CF are found to exhibit better SIM behaviour. Therefore, rational tuning of ligand environment, extremely strong axial CF in comparison to the equatorial CF, can result in very high magnetization blocking temperatures. It is worth pointing out that rational design and synthesis of Ln based PBP complexes are rare in literature. The PBP coordination geometry in all the above described complexes is achieved through a serendipitous manner. Moreover, the coordination sphere in these complexes is fulfilled by either kinetically labile monodentate ligands (ca. **3**) or multidentate chelating ligands (ca. **9**) in such a manner that further chemical modification within the coordination spheres does not guarantee the preservation of PBP coordination geometry.

Therefore, strengthening the axial CF via employing stronger CF donors at the axial coordination sites in these complexes appears extremely difficult. Recently, we have reported a synthetic strategy for a series of Ln(III) based PBP complexes ($(Et_3NH)[(H_2LLnCl_2]$; H_4L = 2,6-diacetylpyridine bis-(salicylhydrazone)) where the coordinating sites in the pentagonal equatorial plane are provided by a pentadentate chelating ligand (H_2L^{2-}) and the axial coordinating sites are occupied by chloride atoms (Fig. 17). The axially coordinated chlorides are found to be kinetically labile, while the chelating ligand in the equatorial plane is kinetically rigid. Therefore, such a complex provides an excellent opportunity to tune the axial CF strength via employing various ligands in order to tailor magnetic behaviour of Ln(III) ions in PBP coordination geometry. However, the magnetic properties of the Dy (**16**) and the Tb analogues with simple chloride atoms in the axial coordination sites are investigated and SIM behaviour is observed for the Dy analogue. The room temperature $\chi_M T$ products for both the Dy(III) (14.5 $cm^3\,K\,mol^{-1}$) and Tb(III) (12.2 $cm^3\,K\,mol^{-1}$) analogues are as expected (14.17 and 11.82 $cm^3\,K\,mol^{-1}$, respectively) for the magnetically exchange free ions. The ac magnetic susceptibility studies revealed that the Tb analogue does not exhibit any *out-of-phase* ac signals even under applied dc fields [161]. On the other hand, the Dy(III) analogue (**16**) displays distinct maxima in the variable temperature frequency dependent *out-of-phase* ac susceptibility (χ''_M) plots even under zero dc field. However, the QTM is significantly large under zero dc field and it is suppressed significantly upon application of dc fields (Fig. 17b). Detailed ac magnetic susceptibility studies are carried out under H_{dc} = 1500 and 500 Oe for the neat and magnetically diluted samples, respectively. Notably, the magnetization dynamics for both the neat and magnetically diluted samples are found similar, with $U_{eff} \approx 48.6\ cm^{-1}$ and $\tau_0 = 1.91 \times 10^{-6}$ s. High QTM and consequently low U_{eff} in **16** can be attributed to the stronger equatorial CF and weaker axial CF in this PBP coordination geometry.

Hepta-coordinate Ln(III)-based mononuclear complexes with principal C_3 symmetry axis are in general stabilized by the tripodal H_3trensal/H_3trenovan encapsulating ligands or by β-diketone-based chelating ligands (Fig. 18) [45,50,157,158]. However, Lucaccini et al. have performed extensive investigations both theoretically (using angular overlap model [162]) and experimentally (EPR spectroscopy) to determine the magnetic parameters for two C_3 symmetric hepta-coordinate complexes [Dy(trensal)] (**17**) and [Er(trensal)] (**18**) (where H_3trensal = 2,2′,2″-Tris-(salicylideneimino)triethylamine); Figs. 18 and 19) [50]. Theoretical calculations predict that each of the eight Kramers doublets are energetically well separated and the energy separations between the ground and first excited states are 50 and 54 cm^{-1} for **17** and **18**, respectively [50]. The theoretical effective *g*-factors for these two complexes are found to be $g_\perp = 9.6$; $g = 2.6$ and $g_\perp = 1.2$; $g = 13$, respectively. It is worth pointing out that the complex **17** represents an *easy-plane* anisotropic model, while the complex **18** represents an *easy-axis* anisotropic model though the Ln(III) ions are in chemically and crystallographically identical environment (Fig. 19). The EPR spectroscopic studies also confirm such behaviour ($g_\perp = 9.4 \pm 0.5$; $g = 1.8 \pm 0.1$ and $g_\perp = 3.6 \pm 0.1$; $g = 11.8 \pm 0.4$, respectively). Interestingly, both the complexes are predicted to exhibit slow relaxation of magnetization (Fig. 19). Ac magnetic susceptibility studies indeed revealed slow relaxation of magnetization with effective energy barriers $U_{eff} = 7\ cm^{-1}$ under H_{dc} = 900 Oe and 22 cm^{-1} under H_{dc} = 800 for the complexes **17** and **18**, respectively. The experimental U_{eff} values differ noticeably from the theoretical predictions because the relaxation of magnetization in these cases does not occur through the anisotropy barrier; instead it occurs through multi-relaxation pathways (direct, Raman and QTM), which is evidenced by detailed investigations on magnetically diluted samples [50,163]. However, though neither **17** and **18** exhibits a magnetic hysteresis loop, **17** deposited on graphene/Ru(0001) or graphene/Ir(111) exhibits distinct magnetic hysteresis loops [156].

Using the same approach, magnetic properties of another series of complexes with the general formula [Ln(trenovan)] (H_3trenovan = 2,2′,2″-tris(((3-methoxysaliclidene)amino)ethyl)-amine; Ln = Ce, Pr, Nd, Sm, Eu, Gd, Tb, Dy, Ho, Er, Tm, and Yb; Fig. 19) have been investigated. In this case, the Ln(III) centres have a local C_3 point group CF symmetry [157]. Interestingly it is observed that the Nd(III), Er(III) and Yb(III) analogues possess an *easy-axis* type magnetic anisotropy, while the Ce(III), Gd(III) and Dy(III) analogues possess an *easy-plane* type magnetic anisotropy. Both the classes exhibit SIM behaviour. Dong et al. have performed magneto-structural investigations for a series of hepta-coordinated Dy(III) complexes with the general formula {[Dy(EIFD)X]·Y} (where EIFD

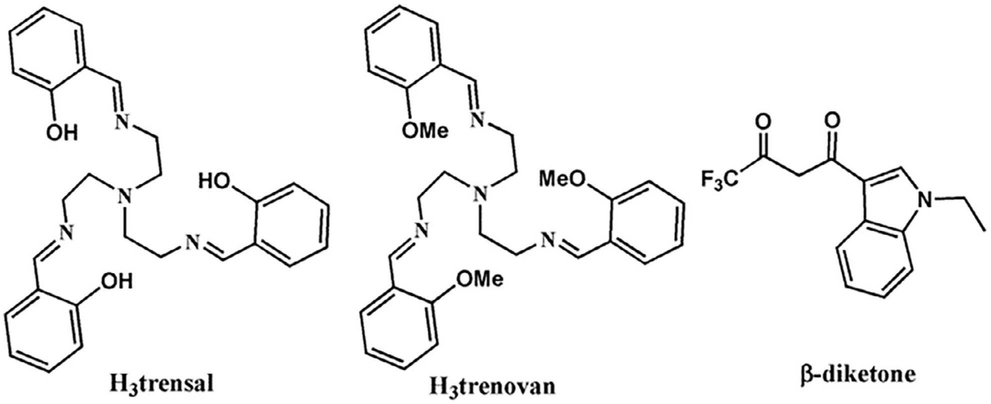

Fig. 18. Schematic drawings for the ligands.

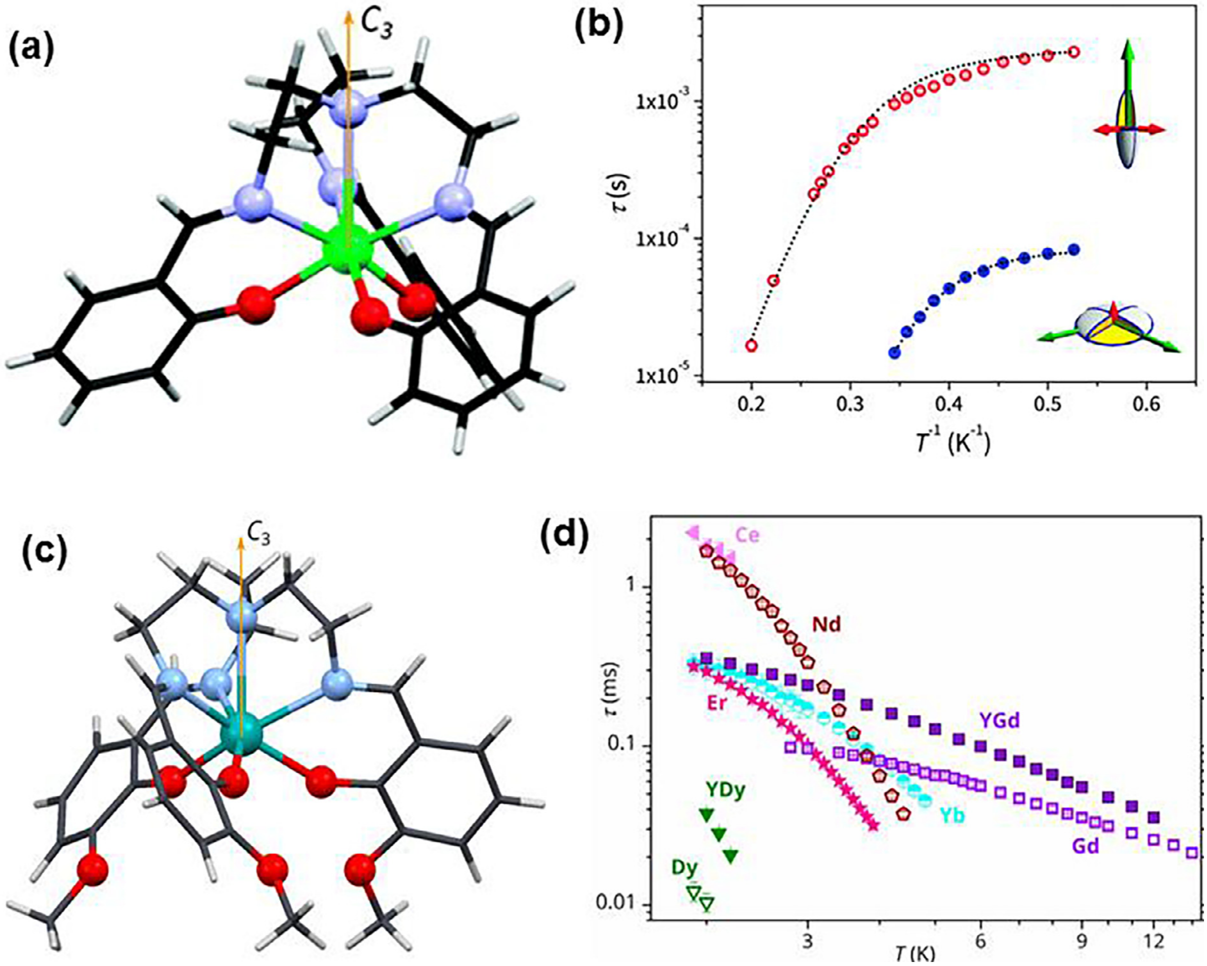

Fig. 19. The representative single crystal X-ray structures of the complexes [Ln(trensal] (Ln = Dy (**17**) and Er (**18**); (a)) and [Ln(trenovan)] (Ln = Ce, Pr, Nd, Sm, Eu, Gd, Tb, Dy, Ho, Er, Tm, andYb; (c)). Colour codes: fluorescent green/magenta = Ln; red = O; light blue = N; grey = C and light grey = H. (b): Temperature dependence of magnetization relaxation time constant (τ) for **17** (blue) and **18** (red). The inset ellipsoids depict the nature of magnetic anisotropy associated with the ground doublets of **17** (*easy-axis* type; below) and **18** (*easy-plane* type; above). (d): Temperature dependence of magnetization relaxation time constant (τ) for [Ln(trenovan)] (Ln = as labelled). Figure and captions are reprinted from the Ref. [50] with permission from Royal Society of Chemistry, and the Ref. [187]; Copyright @ 2017, American Chemical Society.

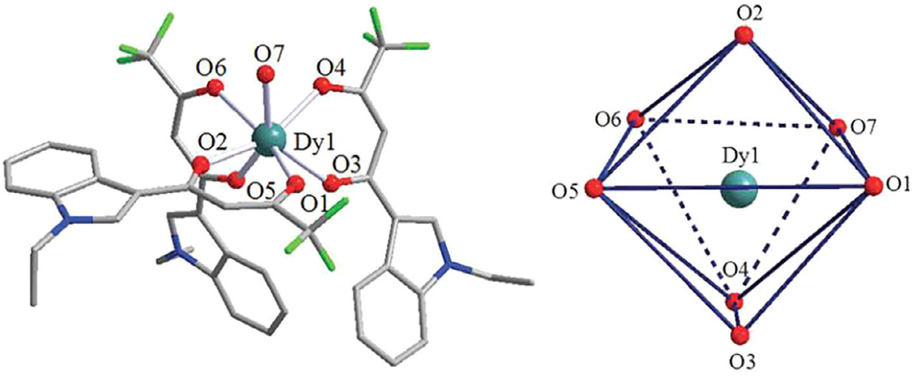

Fig. 20. Single crystal X-ray structure (left) and coordination geometry around the Dy ion (right) of **19**. Colour codes: Magenta = Dy; green = F, red = O; blue = N and grey = C. H atoms are omitted for clarity. Figure and captions are reprinted from the Ref. [158] with permission from the Royal Society of Chemistry.

= 1-(1-ethyl-1H-indol-3-yl)-4,4,4-trifluorobutane-1,3-dione, X = ancillary ligands such as H_2O (**19**)/DMF (**20**)/DMSO (**21**)/TPPO (TPPO = triphenylphosphine oxide; **22**), Y = interstitial solvent = DCM for **19** and **20** and no solvent at all for **21** and **22**; Figs. 18 and 20) [158]. The coordination geometry around Dy(III) in these complexes is distorted capped-octahedron with approximate C_{3v} CF point group symmetry (Fig. 20). The geometric distortion from ideal capped-octahedron is the least for **19** and the most (almost to the capped-trigonal antiprism) for **22**, while moderate distortion is observed for **20** and **21**. Detailed ac magnetic susceptibility investigations revealed that **19** exhibits zero-field magnetization blocking in the temperature domain 2–12 K ($U_{\mathrm{eff}} = 39.4\ \mathrm{cm}^{-1}$).

Weak magnetization blocking was detected for **20** and **21** towards lower temperature only upon employing external dc magnetic fields and with relatively low U_{eff} values (19.9 and 19.2 cm^{-1} under H_{dc} = 2 kOe for **20** and **21**, respectively). But, no magnetization *out-of-phase* ac signal was detected for **22** even under dc fields. Moreover, except **22**, rest of the complexes **19**–**21** display magnetic hysteresis loops with low coercive fields, where wider loop-opening is noticed for **19** compared to **20** and **21**. Such a scenario can be accounted by the suggestion that QTM is more important for larger geometric distortions. Among these complexes, **19** experiences strong axial ligand field and thereby stabilizing the oblate electronic distribution of the ground doublet.

2.3. Hexa-coordinate lanthanide complexes

Hexa-coordinate Ln(III) complexes are far less common unlike transition metal complexes, where *hexa*-coordination is usually the norm. The most frequent *hexa*-coordination is noticed for the solvent-free acetylacetonate (acac) or acac-derivative-based Ln (III) complexes. Even such complexes in the presence of suitable donor solvents or additional ligands quickly transform to higher coordination situations [30]. Although examples of *hexa*-coordinated Ln(III) complexes that function as SIMs are sparse, there are several multinuclear SMMs/SCMs incorporating *hexa*-coordinate Ln(III) ions [22,56,165–167]. However, as predicted from theoretical investigations for the hypothetical $[\mathrm{DyF_6}]^{3-}$ species, trigonal prism and trigonally distorted octahedron coordination geometries stabilize the *Ising* doublet eigen states with M_J = 15/2 as the ground states and all of the *Ising* doublets are quite well-isolated (Fig. 11). The height of their energy landscapes is also significantly large (over 600 cm^{-1}). Therefore, Dy(III)-based *hexa*-coordinated trigonal prism/trigonally distorted octahedron geometric complexes are worth attempting experimentally. On the other hand, octahedral geometry leads to well-isolated first and third *Ising* doublets, but admixing of the other eigen states (Fig. 11). Moreover, its U_{eff} is expected to be quite low compared to its prism/ trigonally distorted octahedron geometric analogues.

Ab initio calculations performed by some of us on $\{\mathrm{Er(OH)_6}\}^{3-}$ and $\{\mathrm{Dy(OH)_6}\}^{3-}$ models possessing ideal octahedral geometry are worth mentioning here [115]. Calculations performed on these models suggest relaxation via ground state for both Er(III) and Dy (III) models because of the cubic ligand field around Ln(III) ion (Fig. 21). Thus a perfect octahedral geometry is unlikely to exhibit any interesting SMM characteristics. However there are ways to improve the properties of octahedral Dy(III) or Er(III) molecules. For oblate ions (such as Dy(III)) strong axial ligand field is needed which can be achievable in these octahedral complexes if four ligands in the equatorial positions are weakly interacting while two ligands in the axial position are strongly interacting, this would then stabilize large M_{J} levels as the ground state leading to moderate to weak SMM characteristics. On the other hand for prolate Ln(III) ions (such as Er(III)), strong equatorial ligation and weaker axial ligation is desired.

Gregson et al. have studied extensively the magnetic behaviour of $[\mathrm{Dy(BIPM^{TMS})_2}]$ $[\mathrm{K(18C6)(THF)_2}]$ (**23**, $\mathrm{BIPM^{TMS}} = \{\mathrm{C(PPh_2\text{-}NSiMe_3)_2}\}^{2-}$, 18C6 = 18-crown-6 ether) [55]. The Dy^{3+} ion in **23** is *hexa*-coordinate and it adopts a distorted octahedral (O_{h}) geometry (Fig. 22). CF multiplets calculation for **23** revealed that the lowest three doublets are anisotropically uniaxial. The ground doublet is purely isolated, the first and second excited doublets are slightly admixed and a strong admixing takes place for both the third and fourth excited doublets with proximate eigen states (Fig. 22). Interestingly, the second excited doublet is essentially axial (g_{xx} = 0.09, g_{yy} = 0.14 and g_{zz} = 14.27) and hence, QTM is not efficient in spite of admixing. Such a scenario suggests the probability of magnetization reversal through the third excited doublet (g_{xx} = 2.09, g_{yy} = 5.61 and g_{zz} = 14.11) and consequently, two relaxation barriers are expected. Theoretical prediction for the existence of two relaxation barriers (ΔE = 515.7 and 562.9 cm^{-1}) is confirmed (U_{eff} = 501.1 and 565 cm^{-1}). The complex exhibits magnetic hysteresis loops with relatively weak coercive fields. Magnetization blocking temperature (T_{B}) for the complex was expressed through all the three methods discussed in Section 1.5.1 and the values with corresponding parameters are summarized in Table 4.

A*b initio* calculations have been performed on $[\mathrm{Zn_3Dy\{(py)_2C(H)O\}_6](ClO_4)_3}$ model complex by some of us [165]. This model has been obtained from diamagnetic substitution of Ni(II) ion with Zn(II) ion from a previously reported molecule [165]. This molecule has a distorted octahedral ligand field around Dy(III) ion and relaxes at the ground state due to strong tunnelling with a possible barrier of 16.6 cm^{-1} in applied field condition (Fig. 23). The local symmetry of the *hexa*-coordinate Ln(III) ion in the complex $[\mathrm{Zn_2DyL_2}]$ (**24**; where L = 2,2′,2″-(((nitrilotris(ethane-2,1-iyl)tris(azanediyl))tris(methylene))tris-(4-bromophenol))) [54] and $[\mathrm{Yb(H_3L)_2}]\mathrm{Cl_3{\cdot}5CH_3OH{\cdot}2H_2O}$ (**25**; where $\mathrm{H_3L}$ = tris(((2-hydroxy-3-methoxybenzyl)amino)ethyl)-amine) [164] is distorted O_{h} (Fig. 24). Though

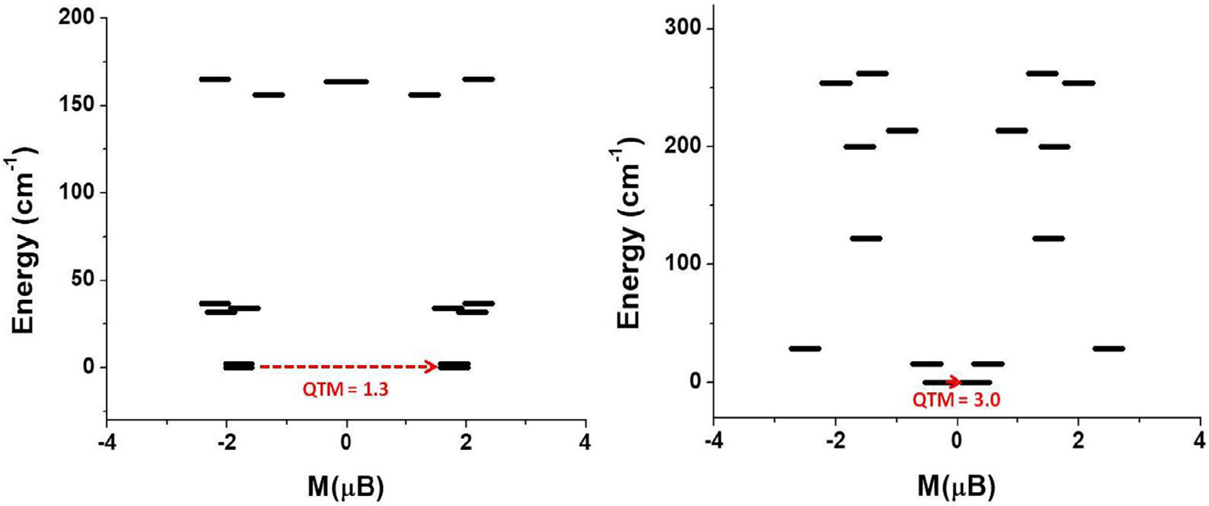

Fig. 21. *Ab initio* SINGLE-ANISO computed magnetization blockade barrier for octahedral $\{\mathrm{Er(OH)_6}\}^{3-}$ and $\{\mathrm{Dy(OH)_6}\}^{3-}$ models (left and right respectively). For more information, see Fig. 46. Plotted from the data given in Ref. [115].

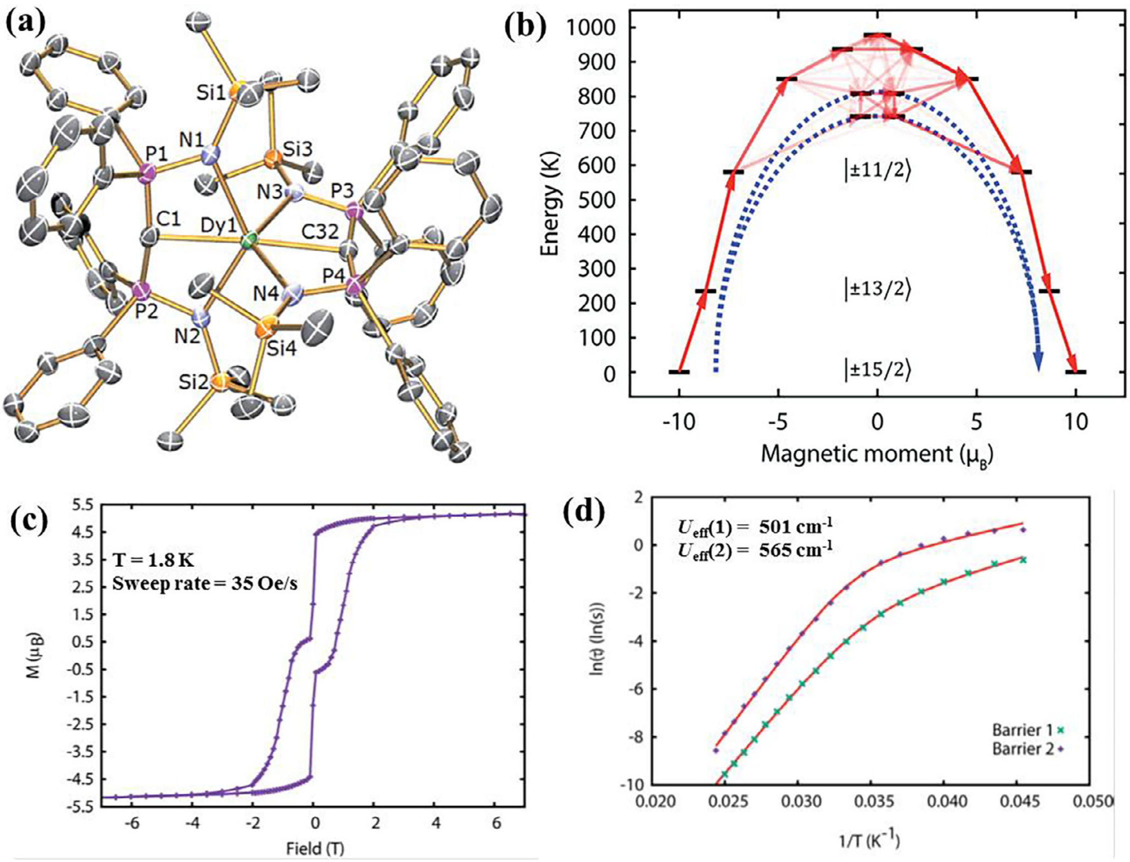

Fig. 22. (a) Single crystal X-ray structure of the anionic part of **23**. H atoms are omitted for clarity; (b) low-lying energy landscapes for **23** from CF multiplet calculations; (c) magnetic hysteresis loop of 1 at 2.8 K with 35 Oe/s field sweep rate and (d) temperature dependence of relaxation times (stars) and the best fits (solid lines). Figure and captions are reprinted from the Ref. [55] with permission from Royal Society of Chemistry.

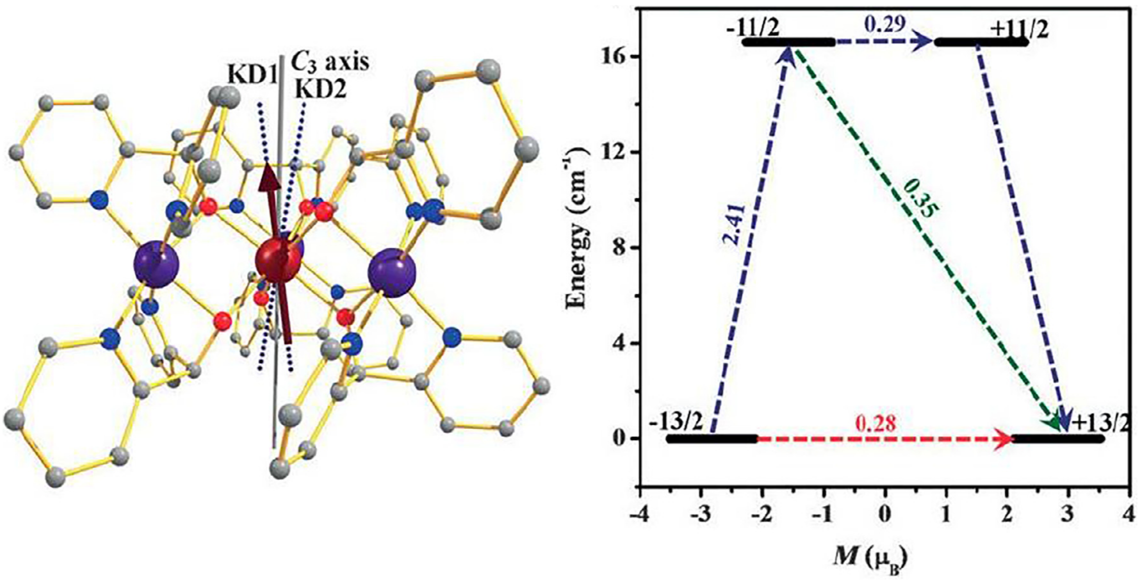

Fig. 23. *Ab initio* computed orientation of the principal magnetization axes of the ground and first excited KDs along with pseudo C_3 axis (left). *Ab initio* computed magnetization blocking barrier for single-ion Dy(III) (right). Thick black line indicates KDs as a function of magnetic moment. Dotted green lines show the possible pathway of the Orbach process. Dotted blue lines show the most probable relaxation pathways for magnetization reversal. Dotted red lines represent the presence of QTM between the connecting pairs. The numbers provided at each arrow are the mean absolute values for the corresponding matrix element of the transition magnetic moment. Figure and captions are reprinted from the Ref. [165] with permission from John Wiley and Sons.

the complex **24** is trinuclear, it can be termed as SIM as the Dy(III) is the sole paramagnetic centre in the complex. However, none of these two complexes (**24** and **25**) exhibit zero-field magnetization blocking though the first excited state is situated at a considerably high energy (Table 4). It is quite surprising especially for **24**, where *ab initio* calculations revealed the ground doublet to be anisotropic

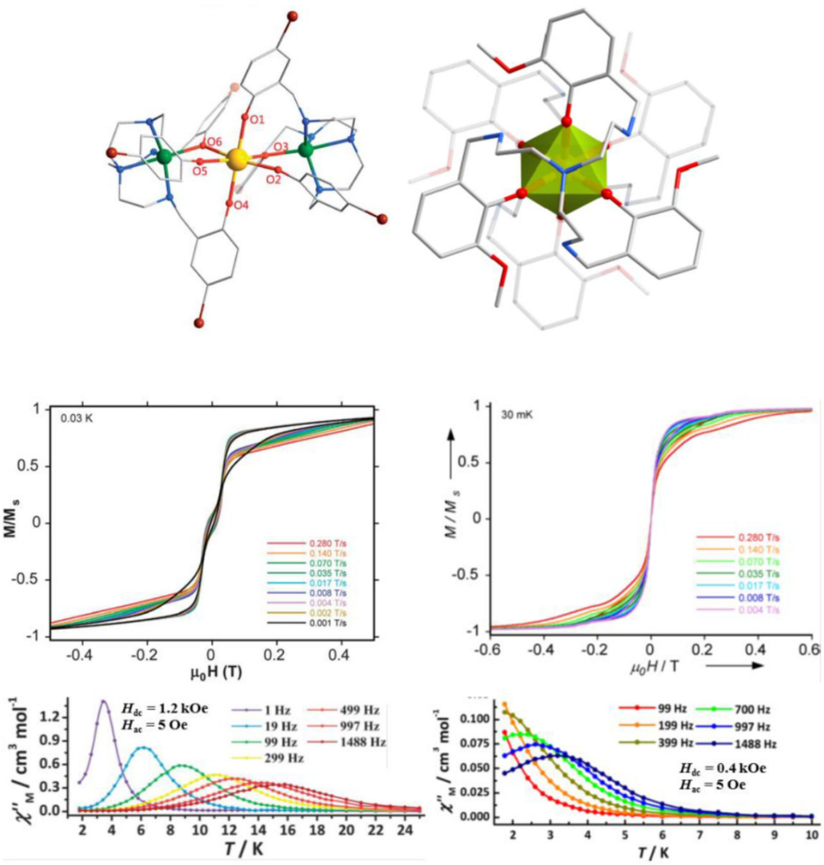

Fig. 24. Single crystal X-ray structures of the complexes **24** (left) and **25** (right), their field-dependent magnetizations (middle) at indicated temperatures and dc field sweep rates and variable temperature variable frequency *out-of-phase* ac susceptibility (χ''_M; bottom) under indicated ac and dc fields. The color codes: yellow = Dy (**24**); yellow (highlighted with octahedron) = Yb (**25**); green = Zn; brown = Br; red = O; blue = N and grey = C. The H atoms are omitted for clarity. Figure and captions are reprinted from the Ref. [54] with permission from Royal Society of Chemistry, and the Ref. [164]; Copyright @ 2012, American Chemical Society.

and almost uniaxial ($g_{xx} = g_{yy} = 0.01$ and $g_{zz} = 19.76$). But, in the case of **25**, strong QTM is expected due to a large rhombic CF perturbation ($g_{xx} = 3.76$, $g_{yy} = 2.71$ and $g_{zz} = 0.72$). However, external dc fields induced non-Orbach slow relaxations but magnetic hysteresis loops could not be detected for any of them (Fig. 24). To have an insight of magnetic behaviour for Dy(III) ion in an ideal O_h geometry with oxygen coordination sites, Liu et al. have performed *ab initio* calculations for a hypothetical species, $[Dy(H_2O)_6]^{3+}$ (**26**). They found that the ground Kramers doublet is completely isotropic ($g_x = g_y = g_z = 6.582$) and the first excited state is situated only above 23.3 cm^{-1} from ground state [54]. Therefore, the presence of weak slow relaxation in **24** induced by external fields can be attributed to geometric distortion. On the other hand, significantly large energy barriers and magnetic hysteresis loops in **23** stem from the strong axial-(C-Dy-C) and weak equatorial (Dy-N) ligand fields which stabilize the *oblate* electronic distribution of the ground state doublet.

2.4. Penta-coordinate lanthanide complexes

Mononuclear penta-coordinate Ln(III) complexes are well known in the literature [168–173]. The common coordination geometries observed in such complexes are distorted trigonal bipyramidal geometry and distorted square pyramidal [174–179]. The trivalent five-coordinate lanthanide complexes find considerable interest in the field of catalysis for cross coupling and polymerization reactions [180–183]. Interesting magnetic properties are also observed in multinuclear five-coordinate Ln(III) complexes [53,184] Here our focus is only on the magnetic features of the mononuclear analogues.

Ab initio calculations on two different penta-coordinated geometries, square pyramidal and trigonal bipyramidal models with molecular formula $\{Er(OH)_5\}^{2-}$ and $\{Dy(OH)_5\}^{2-}$ have been reported by some of us earlier (Fig. 25) [115]. In the square pyramidal model of Er(III) ion, the first three states are strongly axial in nature (0.002–0.047). Orbach relaxation representing off-diagonal elements is found to be small up to the third excited state and QTM probability is also found to be small for the first three KDs. Thermally assisted QTM is found to be very dominant between the third excited state KDs (1.0). This causes relaxation via third excited state with U_{cal} value 157 cm^{-1}. On the other hand in the square pyramidal model of Dy(III) ion, ground state QTM is found to be very large (1.1) and cause relaxation via ground state KD.

In the trigonal bipyramidal model, the axial ligand field is expected to be stronger compared to the square pyramidal model. Because of the stronger axial ligand field in Er(III) trigonal bipyramidal model, ground state QTM is found to be significant (0.3) and first excited state thermally assisted QTM is also found to be extremely large enough (2.2) to cause relaxation through it. However, in the Dy analogues of the same, QTM has been suppressed up to second excited state. Orbach relaxation representing off-diagonal elements are also found to be very small up to third excited state. Ground and first excited KDs are purely Ising in nature and second excited KD is strongly axial in nature. TA-QTM between third excited state is found to be large (3.5) suggesting relaxation via third excited state through TA-QTM with U_{cal} value 475 cm^{-1}.

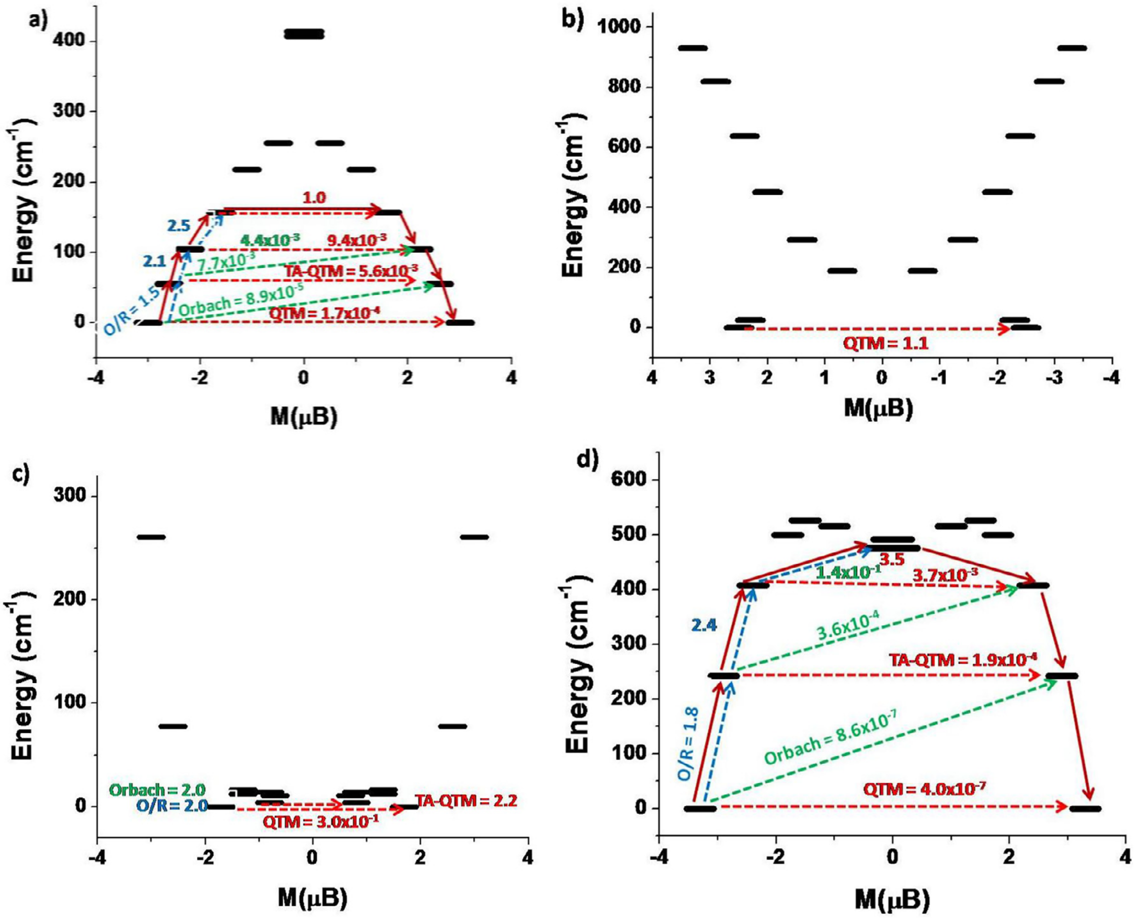

Fig. 25. *Ab initio* SINGLE-ANISO computed magnetization blockade barrier for (a) square pyramidal $\{Er(OH)_5\}^{2-}$; (b) square pyramidal $\{Dy(OH)_5\}^{2-}$; (c) square bipyramidal $\{Er(OH)_5\}^{2-}$ and (d) square bipyramidal $\{Dy(OH)_5\}^{2-}$ models. For more information see Fig. 46. Plotted from the data given in Ref. [115].

Five-coordinate $Dy(NHPh^{i}Pr_2)_3(THF)_2$ (**27**) and $Er(NHPh^{i}Pr_2)_3(THF)_2$ (**28**) complexes were synthesized and characterized by Tang and co-workers. These complexes contain three sterically hindered amide ligands (2,6-$^{i}Pr_2$-C_6H_3NH) in the equatorial plane and two THF ligands in the axial plane (Fig. 26 (a) and (b)) [49]. The Dy(III) complex has been shown to be a zero-field SIM while the Er(III) analogue is a field- induced SIM.

The coordination of THF molecules in the axial positions of the complexes breaks the equatorial crystal field around Dy(III) ions which stabilizes a high M_J state imposing a large magnetic moment into the ground states. Dynamic magnetization studies show that at high temperatures (T > 11 K), the relaxation follows an Arrhenius-like behaviour affording a barrier U_{eff} = 34 K and $\tau_0 = 2.07 \times 10^{-5}$ s. A very narrow distribution of relaxation times is observed in the Cole-Cole plots with α parameter below 0.25. It should be mentioned that Cole-Cole plots are a common method of representation of dispersion statistics. In the current instance plots of χ'' and χ' are used to obtain the multiplicity and distribution of relaxation times. On the other hand, an effective barrier of 25 K was observed for **28** with $\tau_0 = 6.44 \times 10^{-8}$ s (400 Oe). For complex **28**, the axially coordinated THF molecules increases the transverse components of magnetic anisotropy leading to fast quantum tunnelling and consequently the zero field SIM behaviour is lost. Further insight into the magnetic relaxation and magnetization dynamics was obtained by the *ab initio* calculations [185]. The *ab initio* computed orientations of the g-tensors for the ground state KDs are shown in Fig. 27(a).

The *ab initio* computed g-tensors for complexes **27** and **28** (Fig. 27) in the ground state KDs, shows a higher degree of axiality in **27** (g_{xx} = 0.0074, g_{yy} = 0.0128 and g_{zz} = 19.6742) compared to **28** (g_{xx} = 0.0383, g_{yy} = 0.6381 and g_{zz} = 16.1980). Due to the presence of higher axiality, the first excited KDs of complex **27** are found lying quite high in energy (199 cm^{-1}) from the ground state in comparison to complex **28** (76 cm^{-1}). In both the complexes, presence of significant transverse anisotropy components in the first excited state leads to relaxation of magnetization through this route via Orbach/TA-QTM processes (Fig. 27). The computed transversal magnetic moments in the ground state KDs of complex **28** and the presence of non-axial crystal field B_2^2 term suggests that a significant QTM (0.11 μ_B) is expected for this complex and therefore it behaves as a field-induced SIM. However, a comparatively small calculated ground state transversal magnetic moment and weak axial crystal field terms present in complex **27** obscures the QTM process leading to zero field SMM behaviour in complex **27** (Fig. 28).

Recently, Murugesu and co-workers reported a SIM behaviour in a five-coordinate mononuclear lanthanide complex utilizing a rigid ferrocene diamide ligand (^{NN}TBS),(^{NN}TBS)DyI(THF)$_2$, (^{NN}TBS = fc$(NHSitBuMe_2)_2$, fc = 1,1′-ferrocenediyl (**29**) [186]. The coordination sphere of complex **29** is composed of a near linear arrangement of *N*-donor atoms of the diamide, two molecules of THF, and an iodide atom in a trigonal bipyramidal geometry. A dominant electrostatic interaction between the *N* atoms of the ^{NN}TBS ligand and the Dy(III) ion is noted in complex **29** (Fig. 29). The presence of magnetic blocking was confirmed by magnetic hysteresis openings at H = 0 Oe up to 5 K, and at H ≠ 0 Oe up to 14 K. Dynamic susceptibility measurements under zero applied dc field, shows a single peak in the out-of-phase (χ'') susceptibility between 1.9 and 60 K, with shifting peak maxima towards lower frequency.

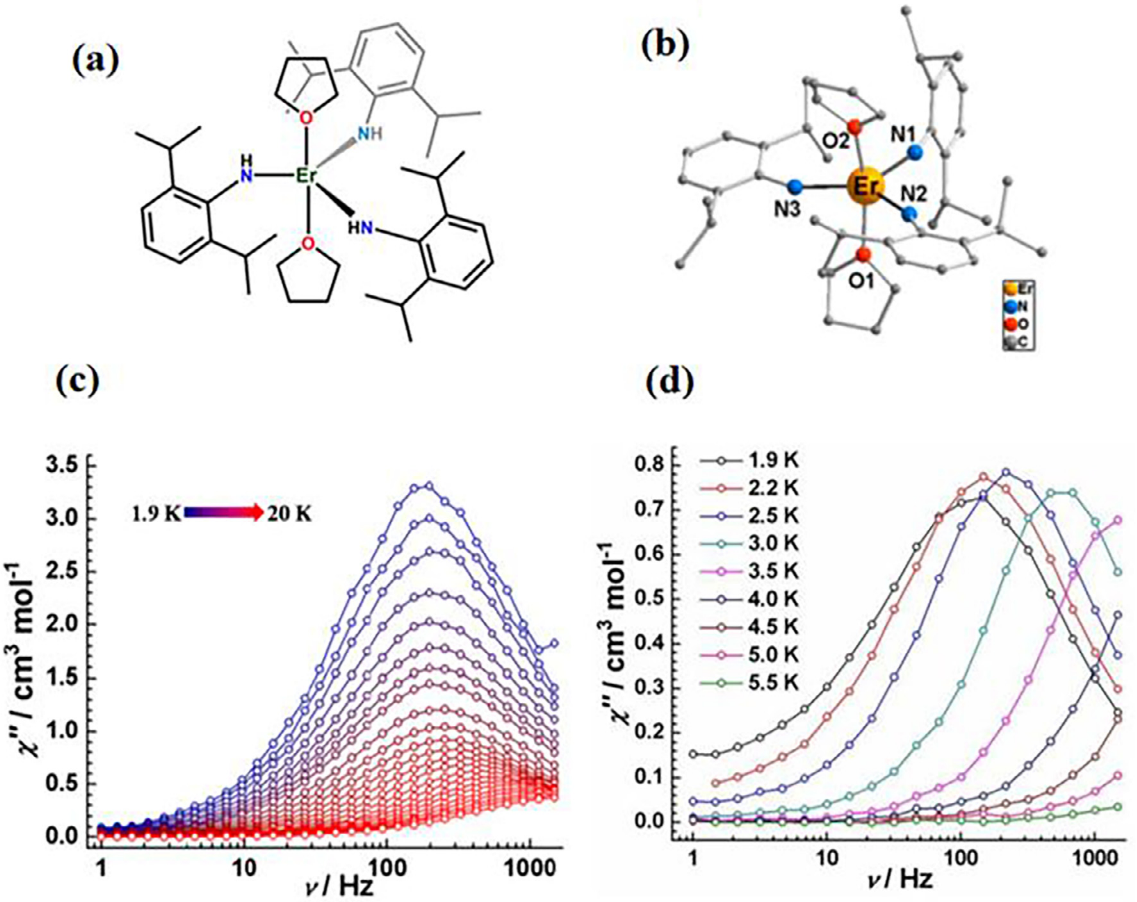

Fig. 26. (a) Molecular structure of Er(NHPh^{i}Pr$_2$)$_3$(THF)$_2$. (b) Crystal structure of Er(NHPh^{i}Pr$_2$)$_3$(THF)$_2$. (c) Temperature dependence of χ'' for **27** under a zero applied dc field, with an ac field of 3 Oe. (d) Frequency dependence under 400Oe-dc field of the out-of-phase (χ'') ac susceptibility component at temperatures between 1.9 and 6 K for **28**. Figure and captions are reprinted with permission from the Ref. [49]. Copyright @ 2014, American Chemical Society.

Fitting the χ'' data to the Arrhenius law gives $U_{eff} = 535.7$ cm^{-1} and $\tau_0 = 8.20 \times 10^{-11}$ s (inset Fig. 29(b)). A narrow distribution of relaxation times was found in the Cole-Cole plots with α parameters ≤ 0.17. In order to gain additional insight of the observed magnetic properties and to analyse the factors governing the magnetization blocking barrier, *ab initio* calculations were performed on **29**. These reveal that the most probable pathway for magnetic relaxation encompasses the third and fourth KDs, while the U_{eff} lies only marginally below the third KD.

These calculations also reveal that the zero-field SIM behaviour is due to a small transverse magnetic moment in the ground state resulting in reduced QTM. The observed lowering of U_{eff} from the anticipated energy of third KD could be due to the presence of mixed relaxation mechanisms or a competitive Orbach relaxation into the higher excited states (Fig. 29(a)). In order to see the effects of the coordinating THF and iodide ligands, *ab initio* calculations were performed on model complexes by sequential removal of the ligands. It is observed that in the absence of transverse ligands, a 33.3% increase in the energy splitting of the first KDs is observed, with $g_{zz} \gg g_{xx}$, g_{yy}, even in the fourth KD. A nearly 3-fold improved value of U_{eff} was obtained for the model complex (**43**) without THF and iodide ligands. The magnetic properties of the five-coordinate lanthanide complexes are summarized in Table 5.

2.5. Tetra-coordinate lanthanide complexes

Mononuclear tetra-coordinate Ln(III) complexes with a variety of sterically bulky ligands are known in the literature [188–190]. Solid-state structures reveal that most of these complexes possess a distorted tetrahedral geometry around the metal centre [189,191–193]. Although such complexes are well studied in the field of catalysis for cross coupling [194] and polymerization [183,195] reactions, there has been a growing interest only in the recent years to study their magnetic properties particularly those containing anisotropic Ln(III) ions. Table 6 summarizes the magnetic properties of the tetra-coordinate trivalent lanthanide complexes.

Yamashita and co-workers in 2010 first studied the SMM/Kondo effect in mononuclear tetra-coordinate LnPc complexes (Ln(III) = Tb, Dy, and Y; Pc = phthalocyanine) that were anchored on Au (111) surface [197]. The Kondo effect refers to a phenomenon of anomalous enhancement in the electrical resistance of an atom when temperature approaches absolute zero [198,199]. While attempting to deposit [LnPc$_2$]$^{n+}$ on an Au(111) surface it was found that in addition to the deposition of the parent molecule, [LnPc]$^{n+}$ fragments (formal coordination number = 4) are formed which also are deposited on the Au(111) surface. A Kondo peak was observed only for the [TbPc]$^{n+}$ molecules at 4.8 K with a Kondo temperature (TK) of ~250 K near the Fermi level (V = 0 V). In contrast, DyPc, and YPc showed no Kondo peak (Fig. 30 (i)). The authors indicate that such [TbPc] $^{n+}$ systems could be of interest in futuristic spintronic applications.

Dunbar and co-workers synthesized a 4-coordinate trigonal pyramidal complex, [Li(THF)$_4$[Er{N(SiMe$_3$)$_2$}$_3$Cl]·2THF (**30**), and studied its magnetic properties [52]. Ac susceptibility measurements reveal that the complex is a zero-field SMM with an effec-

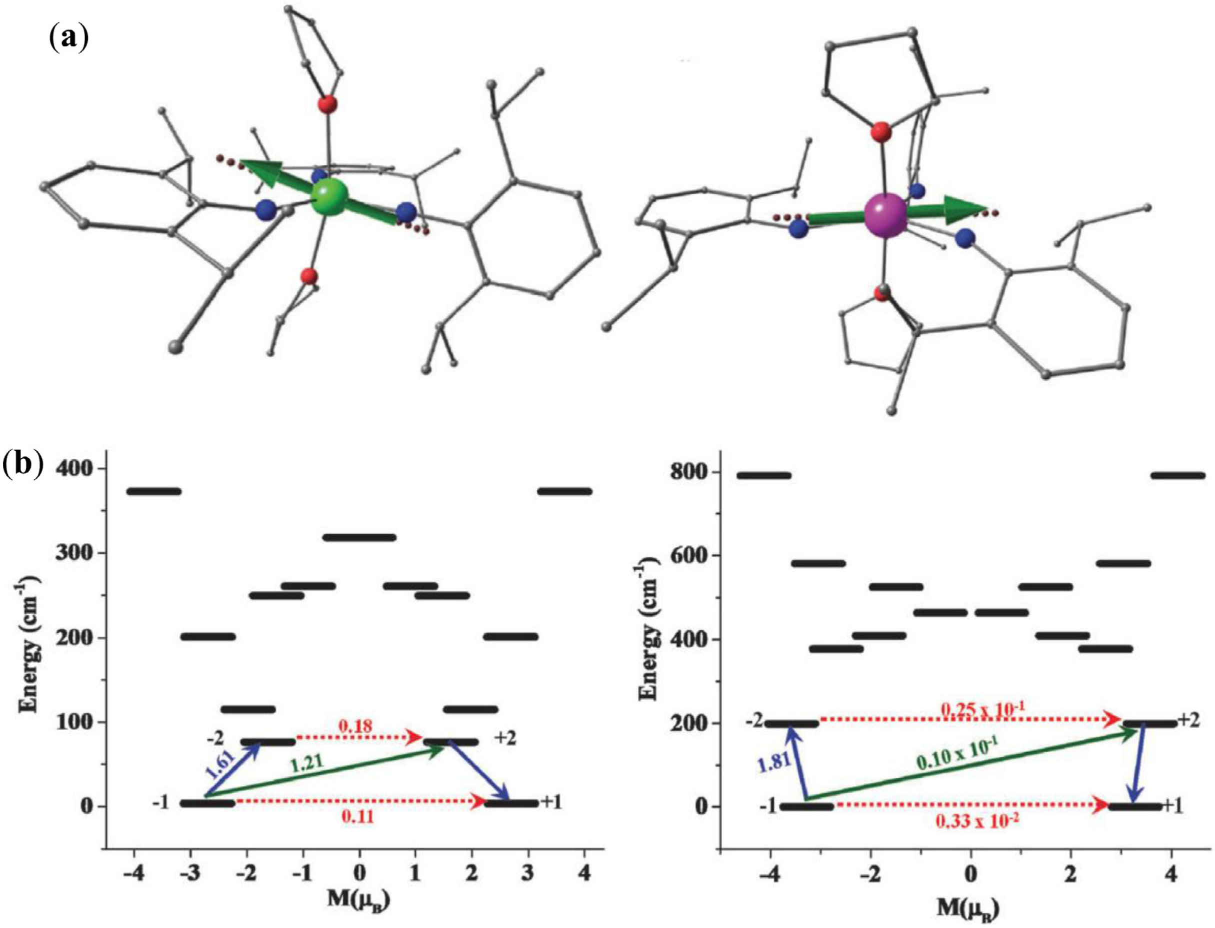

Fig. 27. (a) *Ab initio* computed orientation of the principal magnetization axis of the ground state KDs for complexes Ln(NHPh^{i}Pr$_2$)$_3$(THF)$_2$ on top of the X-ray structure. Colour code: green (Er), pink (Dy), blue (N), red (O), orange (Si) and grey (C). (b) The *ab initio* computed magnetization blocking barrier for Er(NHPh^{i}Pr$_2$)$_3$(THF)$_2$ complex (left) and Dy (NHPh^{i}Pr$_2$)$_3$(THF)$_2$ complex (right). The thick black line indicates the Kramers doublets (KDs) as a function of magnetic moment. The green lines show the possible pathway of the Orbach process. The blue lines show the most probable relaxation pathways for magnetization reversal. The dotted red lines represent the presence of QTM/TA-QTM between the connecting pairs. The numbers provided on each arrow are the mean absolute values for the corresponding matrix elements of the transition magnetic moment. Figure and captions are printed from the Ref. [185] with permission from Royal Society of Chemistry.

tive barrier to the reversal of magnetization U_{eff} = 44 cm^{-1} and τ_0 = 1.07 × 10^{-7} s. The observed butterfly-like hysteresis loop at 1.8 K for **30** further confirms its SIM behaviour (Fig. 31).

Magnetization dynamics studied with the diluted analogue of **31** reveals retention of the out-of-phase signal with partial suppression of the quantum tunnelling regime and a sharper hysteresis up to 3 K [52]. Such complexes with axial chloride ligands could be considered as convenient precursors for the preparation of a family of derivatives and even the possibility of device applications by attaching the molecules to surfaces.

Extensive theoretical exploration on **30** and **31** has been performed by some of us recently to probe the role of Cl$^-$ ion in the estimation of U_{cal} values [200]. Calculations reveal zero-field SMM characteristic of **30**, which is attributed to local symmetry, strength of donor atoms and geometrical distortions around the Er(III) ion. The wave function decomposition analysis indicates that the highest magnetization state (|±15/2⟩) contributes dominantly to the ground state KD in **30** with a slight mixing with the excited states |±9/2⟩, (0.87|±15/2⟩ + 0.10|±9/2⟩), the values indicate the coefficients of the M_J probabilities). Such a mixing of states can be attributed to the close proximity (within ~100 cm^{-1} of energy window) between the ground and excited states. On the other hand, the first three excited KDs are predicted to be dominantly |±13/2⟩, |±11/2⟩, and |±9/2⟩, however, the extent of mixing is significantly larger for these excited KDs compared to the ground KD. *Ab initio* blockade barrier indicates a strong TA-QTM is operative via the 3rd excited KD. Moreover, the Orbach relaxation representing off-diagonal elements between the |+9/2⟩ and |−11/2⟩ are also very significant (0.11μB). Thus, the thermally-assisted magnetic relaxation is expected to occur via the 3rd excited state which places the U_{cal} value as 118 cm^{-1} (Fig. 32a).

Magneto-structural correlations by changing the *out-of-plane* shift parameter (τ) and Er–Cl bond distance suggest τ parameter as the most significant parameter to fine-tune the U_{cal} values as it brings Er(III) ion in the plane of the equatorial ligand (Fig. 32b-c). Moving from the tetrahedral geometry (**30**$_{\text{TD}}$) to trigonal pyramidal geometry (**30**$_{\text{TP}}$) suggest a systematic increase in the barrier height (Fig. 32d-e). Both the computed and experimental barrier height follows the same trends. Replacing Cl ion with other halogens suggests a near linear increase in the barrier height as we move down the halogen group (Fig. 32f). Atom in molecule (AIM) analysis suggests Er-N and Er-X interactions as electrostatic in nature. Equatorial ligand field is found to be stronger than axial ligand field in **30**. This rationalizes the reason for the observed SMM behaviour in **30**.

Detailed theoretical and experimental investigation of the magnetic relaxation and anisotropy of similar four-coordinate Ln (III) complexes with a trigonal-pyramidal geometry, Ln[N(SiMe$_3$)$_2$]$_3$ClLi(THF)$_3$ (Ln = Dy (**32**) and Er (**33**) was also carried out by Tang and co-workers [196]. In both these complexes,

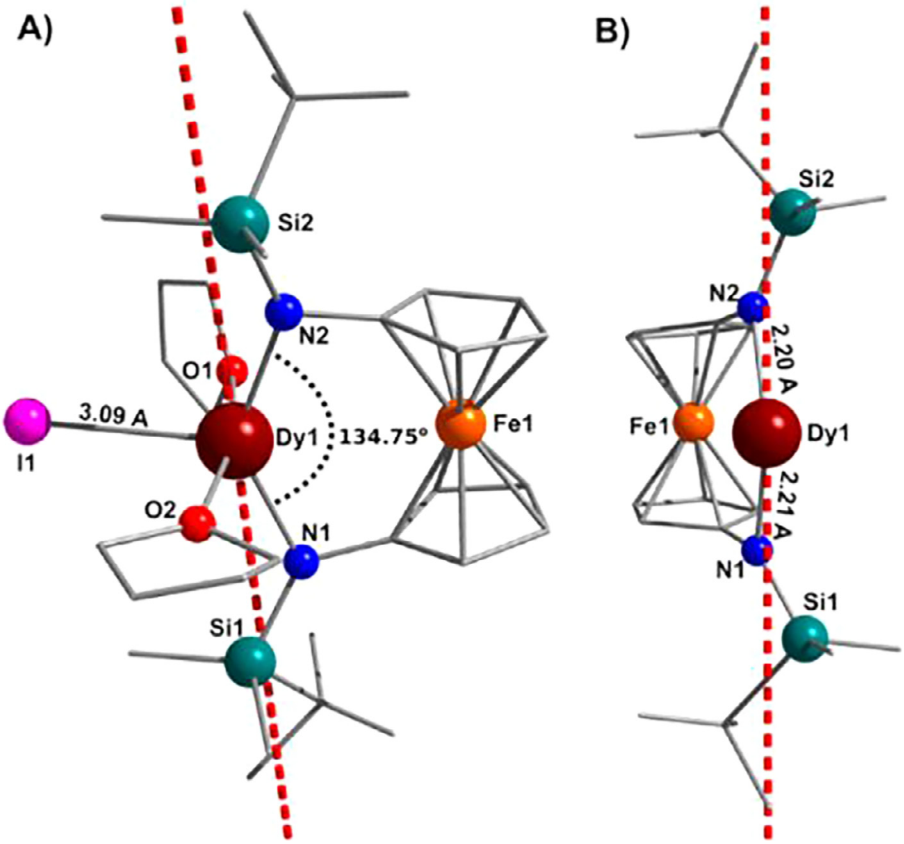

Fig. 28. Structural representation of (A) **29** and (B) ^{NN}TBS ligand–metal bonding. Dashed lines represent the magnetic axis in the ground, first excited and second excited Kramers doublet (KD) states. Figure and captions are reprinted with permission from the Ref. [186]. Copyright @ 2017, American Chemical Society.

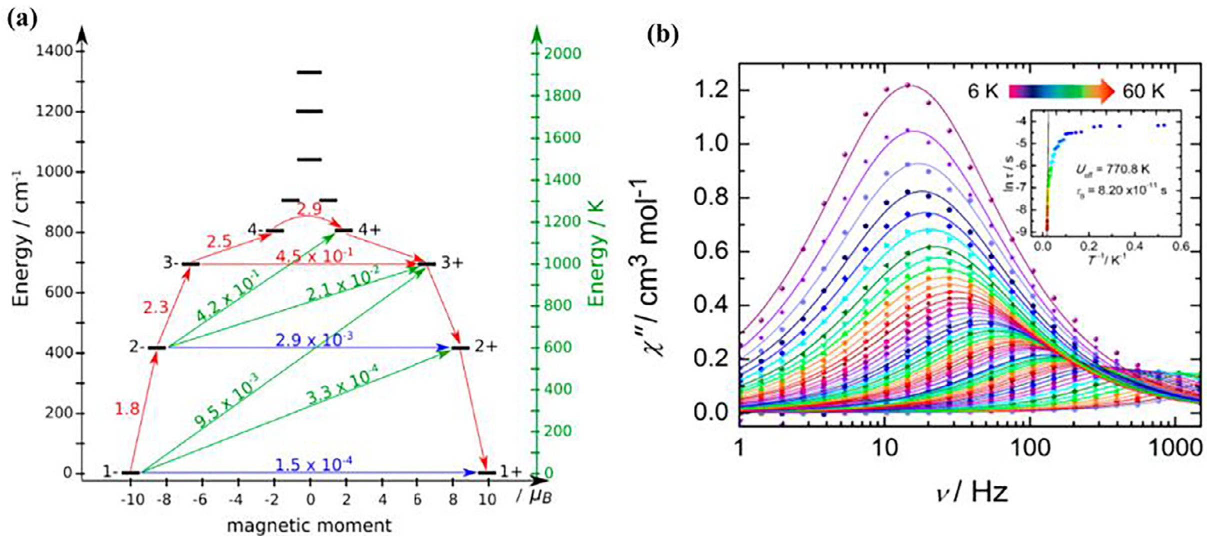

Fig. 29. (a) Frequency dependence of the χ'' magnetic susceptibility for **29** under zero applied dc field from 6 to 60 K. Solid lines represent best fits to the generalized Debye model. Inset: Relaxation time of the magnetization, ln(τ) *vs* T^{-1}; the solid black line represents the linear fit to the Arrhenius equation. (b) Magnetization blocking barrier of (^{NN}TBS)DyI(THF)$_2$. Arrows depict the most probable path for magnetic relaxation (red), QTM (blue) and Orbach relaxation (green). At temperatures where ln(τ) = f(1/T) dependence is linear (see Fig. 29(b) inset), the temperature assisted tunnelling via KD4 is dominant. Figure and captions are reprinted with permission from the Ref. [186]. Copyright @ 2017, American Chemical Society.

presence of significant magnetic anisotropy and/or low-lying excited states is observed in the *M vs H/T* plot at different temperatures.

AC susceptibility measurement reveals that complex **33** is a zero field SIM while complex **32** is a field induced SIM. The strong magnetization blocking behaviour of **33** is indicated in the observed butterfly shaped magnetic hysteresis at 1.9 K (Fig. 33 (right)). In order to get a better understanding of the relaxation mechanisms in such low coordinate lanthanide SMMs, *ab initio* calculations were performed on **32** and **33** [196]. The orientation of

Table 5
Magnetic parameters of the penta-coordinate Ln SIMs.

Complex (No.)	U_{cal}(theo) (cm^{-1})[†]	U_{eff} (exp; cm^{-1} (H_{dc})	Hysteresis	Seep rate (Oe/s)	T_B (K)[‡]	Refs.
Dy(NHPh^{i}Pr$_2$)$_3$(THF)$_2$ (**27**)	199	23 (0)	Yes	*	1.9	[49,185]
Er(NHPh^{i}Pr$_2$)$_3$(THF)$_2$ (**28**)	76	17 (400 Oe)	No	–	–	[49,185]
(^{NN}TBS)DyI(THF)$_2$ (**29**)	692.2	535.7 (0)	Yes	23	5	[186]

[†] The most probable excitation energy for magnetisation reversal.
[‡] The blocking temperature expressed through ZFC susceptibility (a), hysteresis (b) and average life-time (c) study.
[*] Accessible with a conventional magnetometer.

Table 6
Magnetic parameters of the tetra-coordinate Ln SIMs.

Complex (No.)	U_{call}(theo) (cm^{-1})[†]	U_{eff} (exp; cm^{-1} (H_{dc})	Hysteresis	Seep rate (Oe/s)	T_B (K)[‡]	Refs.
[Li(THF)$_4$[Er{N(SiMe$_3$)$_2$}$_3$Cl]·2THF (**30**)	118	44 (0)	Yes	34.6	1.8	[52]
[Er$_{0.1}$Y$_{0.9}${(Me$_3$Si)$_2$N}$_3$(μ-Cl){Li(THF)$_3$}]·pentane (**31**)	28	55.8 (0)	Yes	34.6	3	[52]
Dy[N(SiMe$_3$)$_2$]$_3$ClLi(THF)$_3$ (**32**)	54	12 (600 Oe)	No	–	–	[196]
Er[N(SiMe$_3$)$_2$]$_3$ClLi(THF)$_3$ (**33**)	125	44 (0)	Yes	*	1.9	[196]

[†] The most probable excitation energy for magnetisation reversal.
[‡] The blocking temperature expressed through ZFC susceptibility (a), hysteresis (b) and average life-time (c) study.
[*] Accessible with a conventional magnetometer.

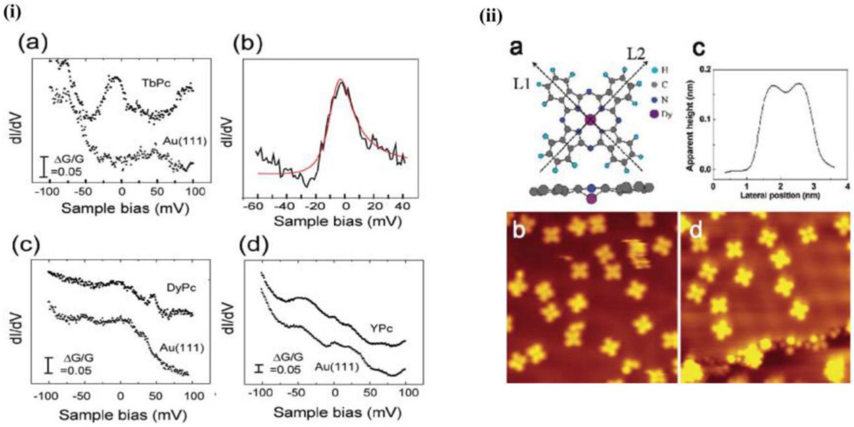

Fig. 30. (i) High resolution STS spectra of (a) TbPc, (c) DyPc, and (d) YPc. The dI/dV data were obtained using the lock-in amplifier with a modulation voltage of 4 mV. (b) Fitting of the spectrum of TbPc with a Fano-shaped function. The smooth red curve is the result of the best fitting (ii) (a) Top and side view structures of a nonplanar DyPc molecule. (b) STM image (15 × 15 nm^2; −0.95 V, 0.4 nA) about the initial molecule adsorption. Individual molecules are imaged as four-leaved structures. (c) Line profile of a single molecule captured along the diagonal direction. (d) Preferential accumulation of DyPc molecules (17.3 × 17.3 nm^2; 0.5 V, 0.4 nA) in the fcc region of Au(111). Figures and captions are reprinted from the Ref. [197] with permission from the Royal Society of Chemistry.

the anisotropy tensors for the Dy(III) and the Er(III) complexes associated with the g_{zz} direction is shown in Fig. 34 (a) and (b). Detailed theoretical studies on tri- and tetra-coordinate lanthanide complexes, **32′**, **32** and **33** revealed that the key role of the entire ligand (and not just the coordinating atom) in influencing the electrostatic potential and hence the magnetic anisotropy of these complexes.

Ab initio calculations performed by some of us on $\{Er(OH)_4\}^-$ and $\{Dy(OH)_4\}^-$ square planar models are worth mentioning here, although no experimental structure of this sort has been reported yet [115]. Calculations performed on these models suggest relaxation via third excited KD for the former with U_{cal} value 390 cm^{-1} whereas extensive QTM for the latter is seen in the ground state (Fig. 35). $\{Er(OH)_4\}^-$ model provides maximum transverse ligand field strength at a given Er-O distance. QTM has been suppressed up to second excited state and relaxation occurs via third excited state in $\{Er(OH)_4\}^-$. Orbach relaxation representing off-diagonal elements are also found to be very small up to third excited state. Ground state KD is purely Ising in nature and first and second excited KDs are strongly axial in nature. Thermally assisted QTM between third excited state is found to be large suggesting relaxation via third excited state through TA-QTM.

2.6. Tri-coordinate lanthanide complexes

Ab initio calculations performed by some of us on $\{Er(OH)_3\}$ and $\{Dy(OH)_3\}$ models suggest relaxation via highest possible excited KD for the former with U_{cal} value 544 cm^{-1}. But, extensive QTM for the latter is seen in the ground state (Fig. 36) [115]. $\{Er(OH)_3\}$ model provides desired strong transverse ligand field at a given Er-O distance. Because of the absence of axial component of the ligand field, QTM has been suppressed up to higher excited state and relaxation occurs via highest possible excited state in $\{Er(OH)_3\}$. Orbach relaxation representing off-diagonal elements are also found to be very small up to higher possible excited state. First, the four KDs are purely Ising in nature and the next three KDs are strongly axial in nature suggesting relaxation via highest possible excited state through TA-QTM.

Some tri-coordinate trivalent lanthanide complexes are known in the literature [187,201–204]. Three-coordinate monomeric Ln (III) complexes containing sterically bulky silylamide ligands have been prepared and characterized. The metal centre and the three bis(trimethylsilyl)amido ligands are arranged in a trigonal pyramidal fashion with the metal centre being slightly above the mean-plane of the molecule (e.g. 0.5782(17) Å for the complex **34**). It

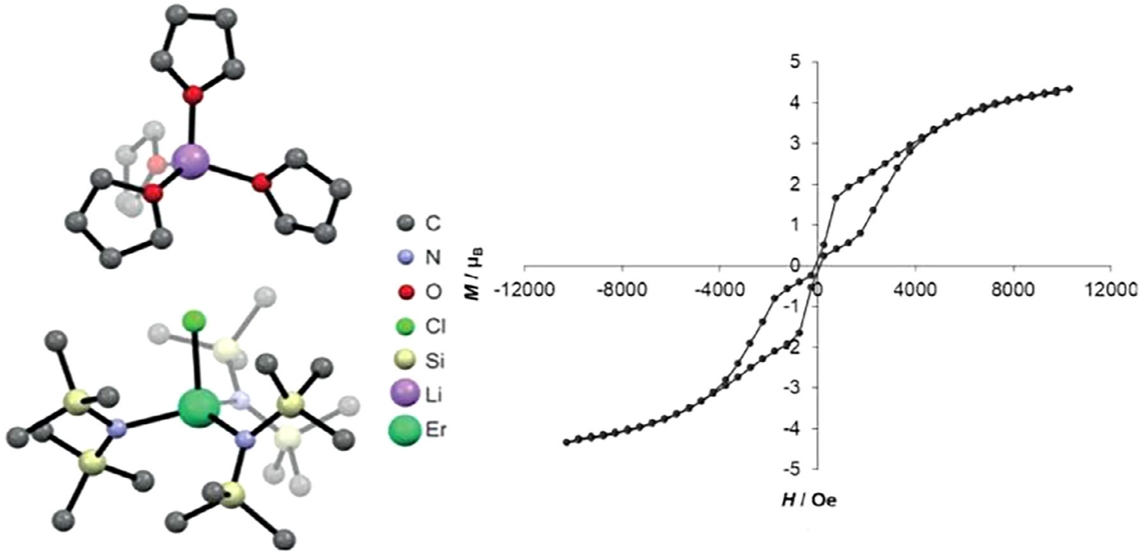

Fig. 31. (a) Molecular structure of **30** (left). Magnetic hysteresis loop for **30** (right) collected at 1.8 K and with 34.6 Oe/s sweep rate. Figure and captions are reprinted from the Ref. [52] with permission from Royal Society of Chemistry.

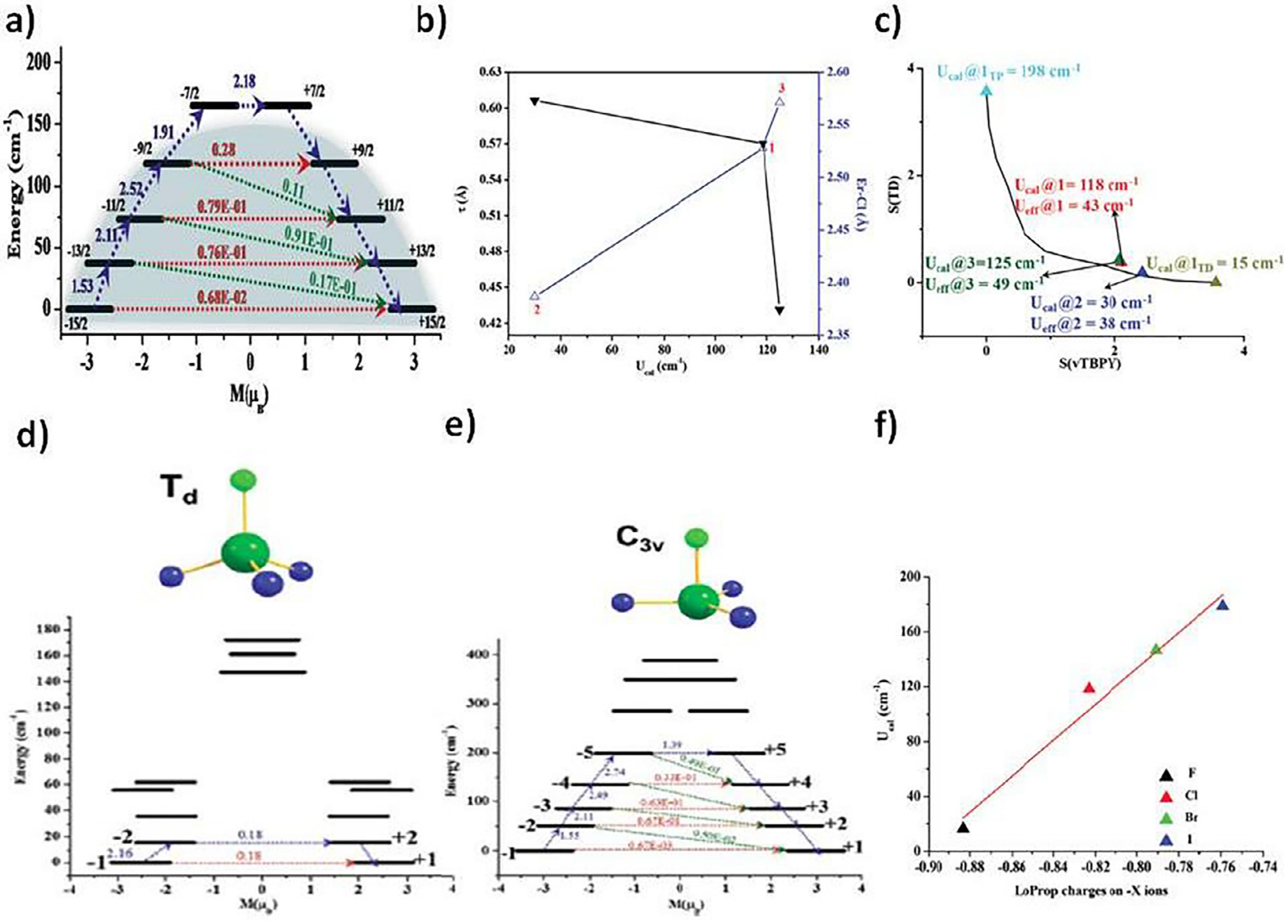

Fig. 32. a) *Ab initio* SINGLE_ANISO computed magnetization blockade barrier for **30** (without solvent); b) two dimensional plot representing the dependency of Ucal value on the Er–Cl bond distance and τ parameter; c) continuous symmetry map representing minimal distortion pathway between tetrahedral (TD) and axially vacant trigonal bipyramid (vTBPY) for studied Er(III) complexes; d–e) *Ab initio* blockade barrier for model complexes $\mathbf{30_{TD}}$ and $\mathbf{30_{TB}}$ respectively and f) The plot of observed U_{cal} values in [Er{N(SiMe3)2}3X]$^-$ (where X = F, Cl, Br, and I) *vs*. LoProp charge on –X ions. Figure and captions are reprinted from the Ref. [200] with permission from Royal Society of Chemistry.

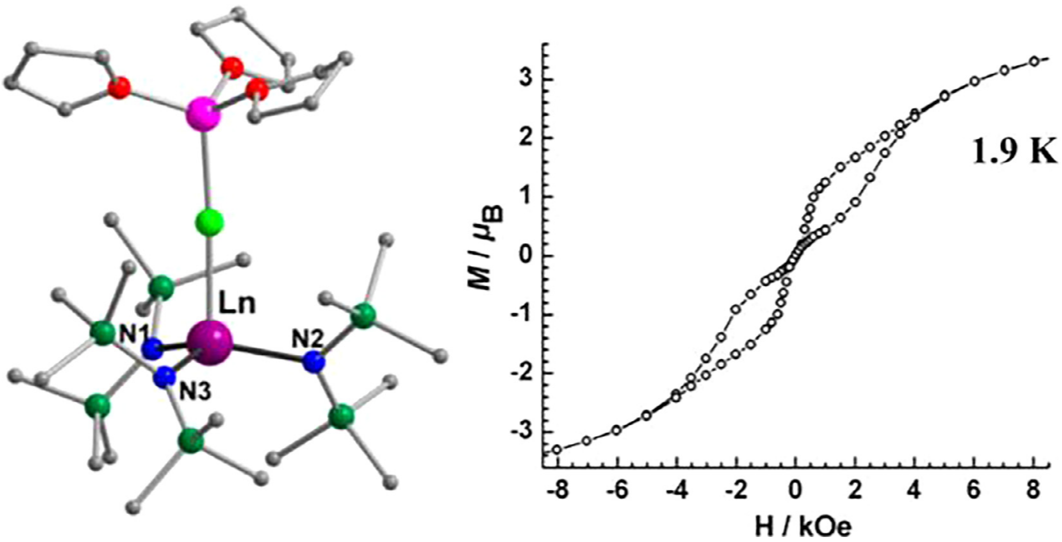

Fig. 33. Molecular structure of complex **32** and **33** with violet, pink, green, blue, red, and grey spheres representing Ln, Li, Cl, N, O, and C atoms, respectively (left). Also, magnetic measurements reveal a butterfly shaped magnetic hysteresis in **33** at 1.9 K (right). Figure and captions are reprinted with permission from the Ref. [196]. Copyright @ 2016, American Chemical Society.

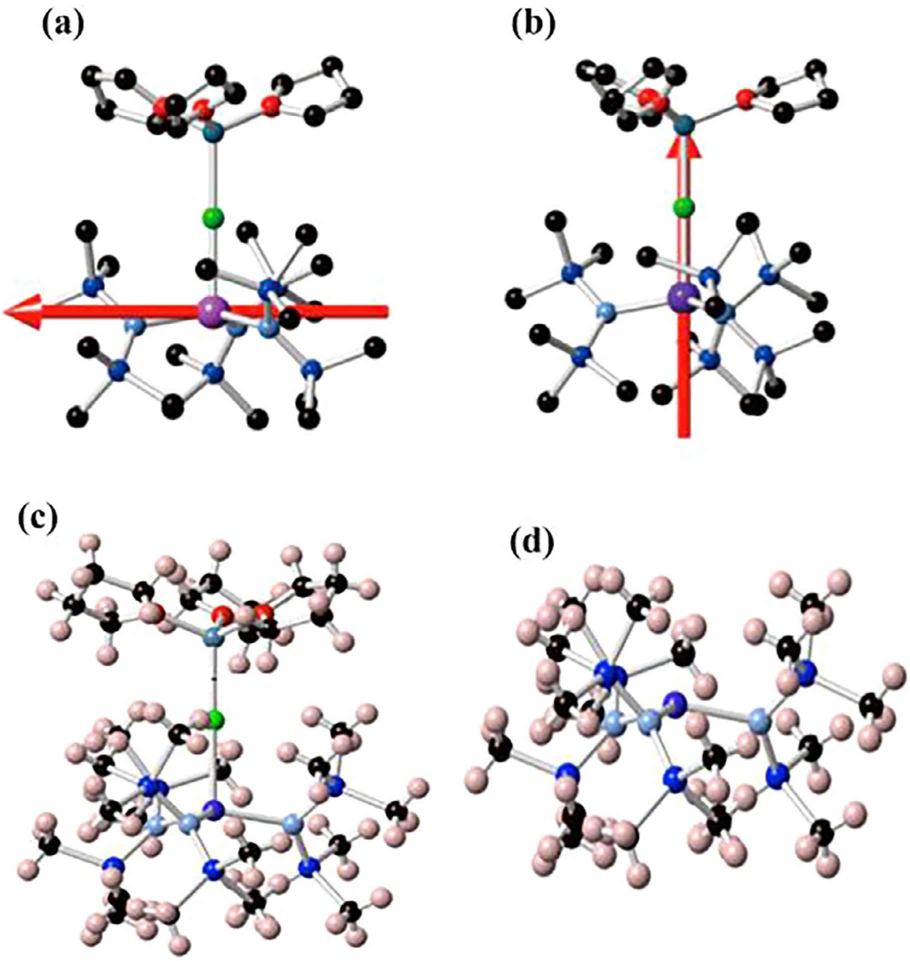

Fig. 34. Orientation of the calculated g_Z direction associated with the ground Kramers doublet for complexes **32**(**a**) and **33**(**b**). (c) Structures of complex **32** and (d) model complex **32**′. Figure and captions are reprinted with permission from the Ref. [196]. Copyright @ 2016, American Chemical Society.

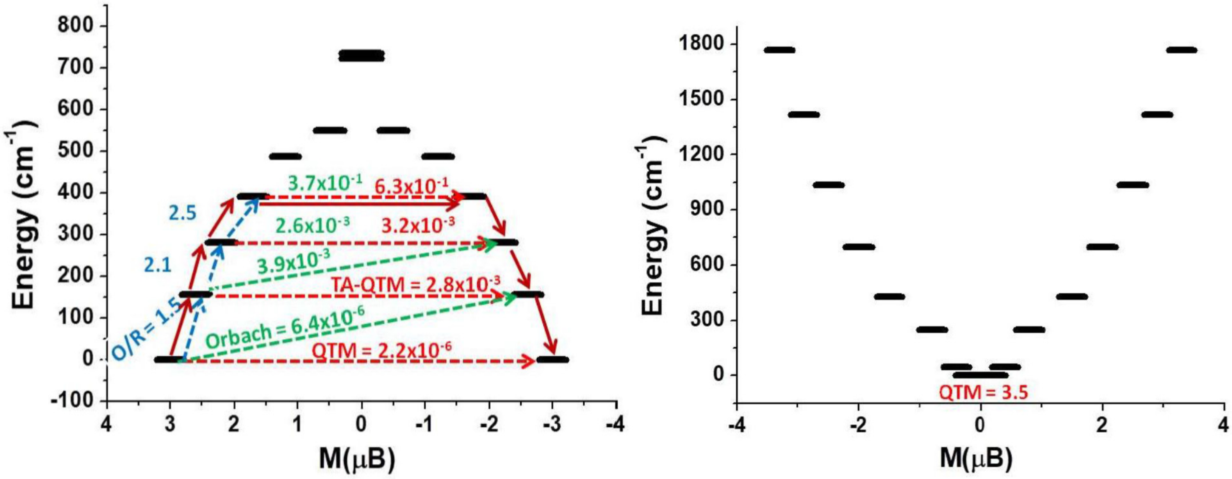

Fig. 35. *Ab initio* SINGLE_ANISO computed magnetization blockade barrier for the $\{Er(OH)_4\}^-$ and $\{Dy(OH)_4\}^-$ models (left and right respectively). For more information see Fig. 46. Plotted from the data given in Ref. [115].

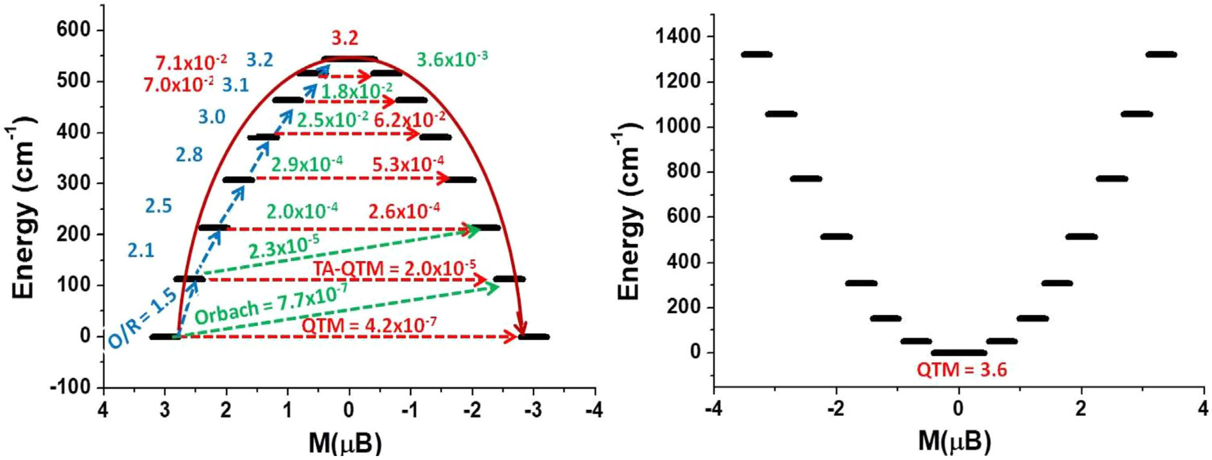

Fig. 36. *Ab initio* SINGLE_ANISO computed magnetization blockade barrier for the $\{Er(OH)_3\}$ and $\{Dy(OH)_3\}$ models (left and right respectively). For more information see Fig. 46. Plotted from the data given in Ref. [115].

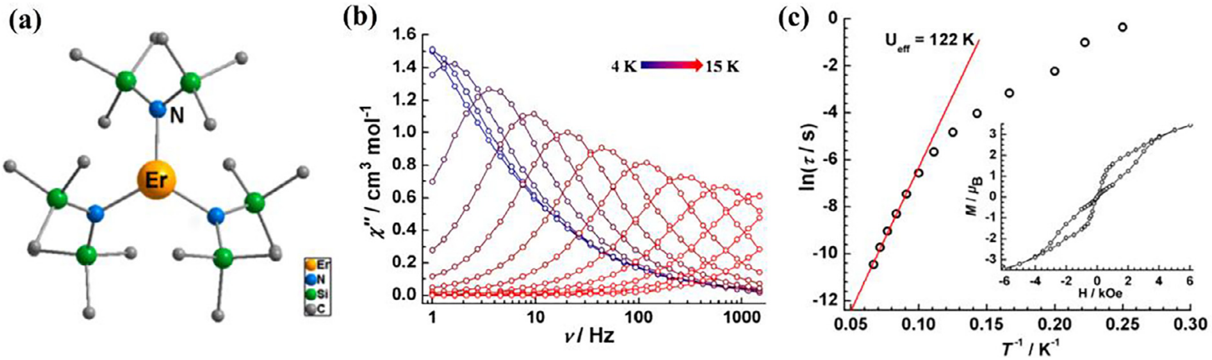

Fig. 37. (a) Molecular structures of $Er[N(SiMe_3)_2]_3$ (**34**). (b) Temperature dependence of χ'' for **34** under a zero applied dc field, with an ac field of 3 Oe. (c) Magnetization relaxation time constant as ln(τ) *vs* T^{-1} for **34**; Inset: Molar magnetization at 1.9 K. Figure and captions are reprinted with permission from the Ref. [49]. Copyright @ 2014, American Chemical Society.

should be pointed out that a carbon atom of each of the amido ligand is in close contact with the metal centre. This results in an effective pseudo trigonal-prismatic geometry about the metal centre. The magnetic properties of 3-coordinate $Ln[N(SiMe_3)_2]_3$ (Ln = Er(III); **34**, Dy(III); **35**) were first studied by Tang and co-workers [49]. They observed that the complexes possess an equatorial triangular geometry with a crystallographically imposed C_3 symmetry around the Er(III) ion (Fig. 37).

The minimized charge contact with the axially located f-element electron density in case of Er[N(SiMe$_3$)$_2$]$_3$ (**34**), stabilizes the high magnitude $M_J = \pm 15/2$ states as the ground state showing an easy axis property. The presence of the C$_3$ symmetry around Er (III) is believed to enhance the uniaxial anisotropy and hence efficiently suppresses the zero-field QTM. An important point here is that C$_3$ symmetric six or seven-coordinate mononuclear Dy(III) or Er(III) SIMs displays fast zero field QTM due to large mixing of different M_J states [50,205,206].

In contrast to **34** discussed above, in the corresponding Dy[N(SiMe$_3$)$_2$]$_3$ (**35**), the ground states are found with the smallest $M_J = \pm 1/2$ component possessing the hard-axis or easy-plane properties. Consequently, detailed magnetic studies reveal that the Er (III) complex behaves as a strong SIM at zero applied magnetic field with effective suppression of QTM, while the Dy(III) analogue does not show any SIM behaviour. An effective barrier of magnetization reversal $U_{\mathrm{eff}} = 85$ cm^{-1} and $\tau_0 = 9.33 \times 10^{-9}$ s is observed for the Er (III) complex. Moreover, a butterfly-shaped magnetic hysteresis loop has been reported for Er[N(SiMe$_3$)$_2$]$_3$ complex confirming its SIM behaviour [49].

To probe the magnetic anisotropy and the magnetic relaxation pathways associated with **34** and **35**, *ab initio* CASSCF + RASSI/SINGLE-ANISO calculations were performed by Rajaraman and co-workers using MOLCAS 7.8 code [185]. Based on the electrostatic potential, the principal magnetization axis of the ground state KD is shown to be oriented along the C$_3$ axis for both **34** and **35** as shown in Fig. 38. Multiple relaxation paths (TA-QTM and Orbach process) were found to be weakly operational in the case of the Er(III) complex that reduces the U_{eff} value over the estimated value of 331 cm^{-1}.

In contrast, for the Dy(III) analogue, the $M_J = \pm 1/2$ is stabilized as the ground state, followed by other higher M_J excited states, resulting in a barrier less potential well. Also, the computed transversal magnetic moments clearly suggest that ground state QTM is the major relaxation pathway for **35**, and this wipes out the SMM behaviour. As mentioned above in the experimental result, the Er (III) is slightly above the mean-plane of the molecule. Theoretical studies suggest that if the Er(III) were to be perfectly in the same plane, the U_{eff} values would be even higher [185]. Table 7 summarizes the magnetic properties of the tri-coordinate Ln(III) complexes.

2.7. Bi-coordinate lanthanide complexes

In this section we will describe compounds that are formally two-coordinate. However, it must be mentioned at the outset, that till date two-coordinate Ln(III) complexes have not been isolated and characterized. There have been theoretical studies on potential two-coordinate cationic complexes. Some bond parameters and the energy barriers for the magnetization reversal obtained from theoretical studies on these complexes are summarized in Table 8. In contrast to the lack of linear two-coordinate Ln(III) complexes, there are examples of two-coordinate Ln(II) complexes that possess near linear geometries. The homoleptic bis(amide) complexes, [(^{i}Pr$_3$Si)$_2$N–Ln–N(Si^{i}Pr$_3$)$_2$] (Ln = Sm(II); **36**, Eu(II); **37**, Tm(II); **38**, Yb (II); **39**) have been isolated and characterized and have been shown

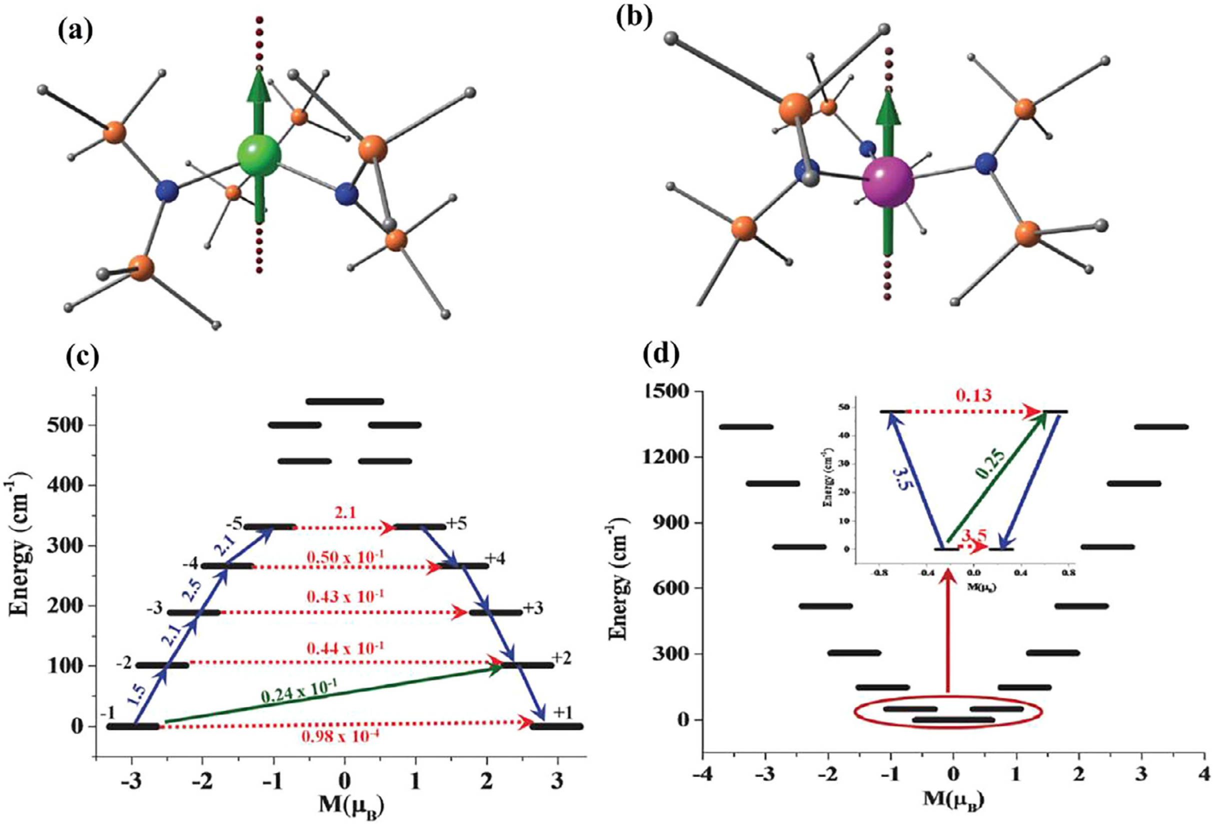

Fig. 38. *Ab initio* computed orientation of the principal magnetization axis of the ground state KDs for complexes (a) **34**, and (b) **35** plotted on top of the X-ray structure. Colour code: green (Er), pink (Dy), blue (N), red (O), orange (Si) and grey (C). The hydrogens are omitted for clarity. (c) The *ab initio* computed magnetization blocking barrier for Er[N(SiMe$_3$)$_2$]$_3$ complex (d) The *ab initio* computed magnetization blocking barrier for Dy[N(SiMe$_3$)$_2$]$_3$ complex. The thick black line indicates the Kramers doublets (KDs) as a function of magnetic moment. The green lines show the possible pathway of the Orbach process. The blue lines show the most probable relaxation pathways for magnetization reversal. The dotted red lines represent the presence of QTM/TA-QTM between the connecting pairs. The numbers provided on each arrow are the mean absolute values for the corresponding matrix elements of the transition magnetic moment. Figure and captions are reprinted from the Ref. [185] with permission from Royal Society of Chemistry.

Table 7
Magnetic parameters of the tri-coordinate Ln SIMs.

Complex (No.)	U_{cal}(theo) (cm^{-1})[†]	U_{eff} (exp; cm^{-1} (H_{dc})	Hysteresis	Seep rate (Oe/s)	T_B (K)[‡]	Refs.
Er[N($SiMe_3$)$_2$]$_3$ (**34**)	331	85	Yes	*	1.9	[49,185]
Dy[N($SiMe_3$)$_2$]$_3$ (**35**)	48	No	No	–	–	[49,185]

[†] The most probable excitation energy for magnetisation reversal.

[‡] The blocking temperature expressed through ZFC susceptibility (a), hysteresis (b) and average life-time (c) study.

[*] Accessible with a conventional magnetometer.

Table 8
Magnetic parameters of the bi-coordinate Ln(III) SIMs.

Complex (No.)	L-Ln-L angle (°)	U_{cal}(theo) (cm^{-1})[†]	Refs.
[(^{i}Pr$_3$Si)$_2$N–Dy–N(Si^{i}Pr$_3$)$_2$]$^+$ (**40**)	175.5	1800	[38]
[Dy{C($SiMe_3$)$_3$}$_2$]$^+$ (**41**)	137.0	1247	[37]
[Dy{C($SiMe_3$)$_3$}$_2$]$^+$ (**42**)	143.4	1484	[37]
[(^{NN}TBS)Dy]$^+$ (**43**)	134.7	1591	[186]

[†] The most probable excitation energy for magnetisation reversal.

to possess L–Ln(II)–L bending angles of >167° (L = N(Si^{i}Pr$_3$)$_2$) [38,207]. However, even in these compounds, secondary interactions between the carbon atoms on the ligand and the lanthanide metal ion suggest that the actual coordination experienced by the central lanthanide ion is greater than two and is probably closer to six (Fig. 39). Other examples of two-coordinate mononuclear Ln(II) complexes with shorter bending angles are also known [183,208,209].

In spite of the fact that there has been no success in the isolation of two-coordinate Ln(III) complexes, many theoreticians have been interested in these systems because these can have uniaxial potential where the stabilization of the largest angular momentum projections of the ground state spin–orbit multiplet can occur. This is expected to lead to SIM behaviour with large energy barriers.

Theoretical calculations (*ab initio* CASSCF/RASSI/SINGLE_ANISO) on [(^{i}Pr$_3$Si)$_2$N–Dy–N(Si^{i}Pr$_3$)$_2$]$^+$ (**40**) reveals that the lowest six Kramers doublets are $M_J = \pm 15/2, \pm 13/2, \pm 11/2, \pm 9/2, \pm 7/2$ and $\pm 5/2$ [38]. These share a common quantization axis. The calculations further indicate that both the probability of QTM within the ground doublet and thermally activated-QTM are extremely small. Orbach relaxation was also found to be strongly disfavoured in the low lying states (Fig. 39 (b)). In view of this it is concluded that efficient magnetic relaxation can only occur via the highest energy doublets. This results in the computation of an energy barrier, U_{eff} = 1800 cm^{-1} for **40** which is far greater than for any other complex reported till date. These studies also indicate that magnetization blocking and hence, magnetic hysteresis can in principle be achieved above 77 K. Theoretical studies further indicate that the two-coordinate Dy(III) compound is stabilized when the Dy–N bond length is shortened and the N–Dy–N angle is closer to 180°. One valid criticism of these theoretical studies is that they do not appear to consider the effects of a counter anion including its role in short contacts and crystal packing. Theory also suggests that Ln (III) complexes with carbon-based dianionic monodentate ligands such as, [(^{i}Pr$_3$Si)$_2$C–Dy–C(Si^{i}Pr$_3$)$_2$]$^-$, could further increase the U_{eff} by a factor of 1.2–1.3.

In order to find out if a rigorous requirement for near linearity (i.e. L–Ln–L bond angle ≅ 180°) is needed in two-coordinate Ln (III) complexes, theoretical studies were carried out on model L–Dy(III)–L systems, (L_1 = N(SiH_3)$_2$, L_2 = C(SiH_3)$_3$, and L_3 = CH(SiH_3)$_2$) by varying the bending angle, θ [37]. As shown in Fig. 40(a) while there is no sharp/sudden decrease in U_{eff} as θ changes, the higher values of the energy barrier are achieved at linear geometries. Even when the bending angle is smaller than near linear angles the presence of a strong axial field prevents the mixing of low lying M_J states with opposing projections which prevents QTM. These

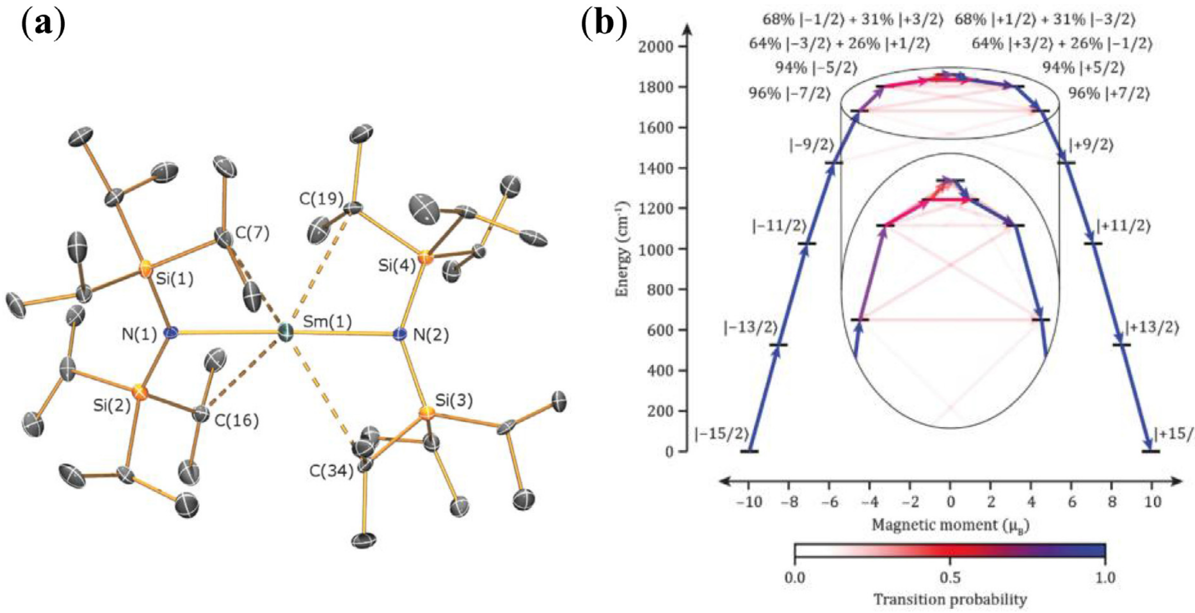

Fig. 39. (a) Molecular structure of near linear two-coordinate complex **36**; Sm1–N1; 2.483(6) Å, Sm1–N2; 2.483(6) Å, N1–Sm1–N2; 175.52(18)°. (b) Electronic states and magnetic transition probabilities for the ground $^6H_{15/2}$multiplet of [(^{i}Pr$_3$Si)$_2$N–Dy–N(Si^{i}Pr$_3$)$_2$]$^+$ (**40**) in zero field. Figure and captions are reprinted from the Ref. [38] with permission from Royal Society of Chemistry.

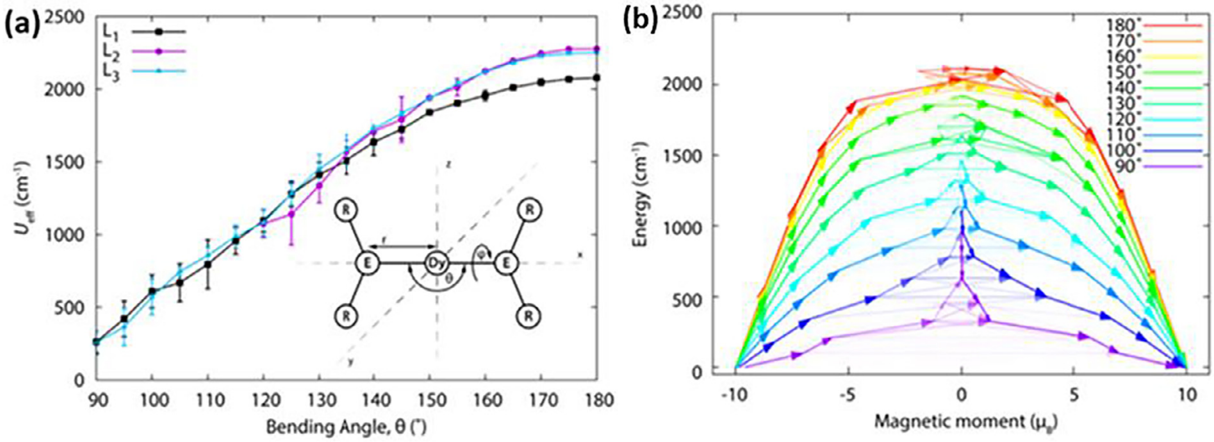

Fig. 40. (a) Relaxation barrier U_{eff} for model complexes as a function of the bending angle θ, averaged for all torsion angles ϕ. Error bars are 1 standard deviation from the mean of the torsion angles ϕ. Inset: Structure of the model complexes. (b) Zero-field magnetic transition probabilities for a complex of **L1** $[\mathrm{Dy}\{\mathrm{N(SiH_3)_2}\}_2]^+$ with ϕ = 90°. The x axis shows the magnetic moment of each state (start and end of each arrow) along the main magnetic axis of the molecule. Relaxation commences from the $|-15/2\rangle$ state and only includes pathways that reverse the magnetization. The transparency of each arrow is proportional to the normalized transition probability. Figure and captions are reprinted with permission from the Ref. [37]. Copyright @ 2015, American Chemical Society.

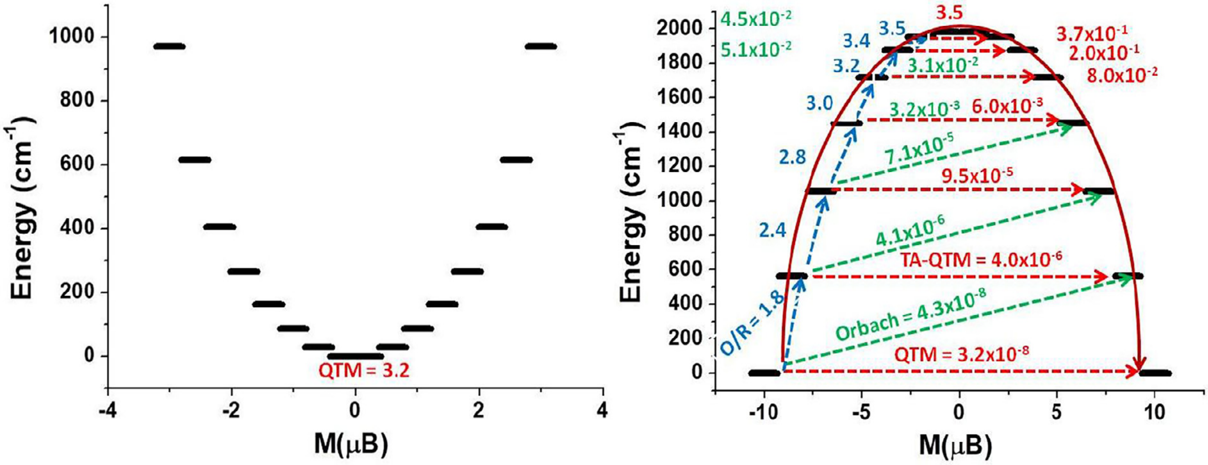

Fig. 41. *Ab initio* SINGLE_ANISO computed magnetization blockade barrier for the $\{\mathrm{Dy(OH)_2}\}^+$ and $\{\mathrm{Er(OH)_2}\}^+$ models (left and right respectively). For more information see Fig. 46. Plotted from the data given in Ref. [115].

results indicate that L–Ln–L angles *need not* be 180° to achieve a large U_{eff} barrier. In order to examine the impact of solvent molecules which increase the coordination number (and afford different geometries), varying numbers of THF ligands were considered. Although, no linear correlation was found, it has been concluded that coordinating solvents such as THF reduces the U_{eff} barrier by 50–70%.

Ab initio calculations performed by some of us on $\{\mathrm{Er(OH)_2}\}^+$ and $\{\mathrm{Dy(OH)_2}\}^+$ models suggest extensive QTM for the former in the ground state, and the relaxation via highest possible excited KD for the latter with U_{cal} value 1983 cm^{-1} (Fig. 41) [115]. The $\{\mathrm{Ln(OH)_2}\}^+$ model provides maximum axial ligand field strength at a given Ln-O distance. In $\{\mathrm{Dy(OH)_2}\}^+$ model, because of the high symmetry and absence of transverse component of the ligand field, QTM has been suppressed up to higher excited state. Orbach relaxation representing off-diagonal elements are also found to be very small up to higher possible excited state. All the excited KDs are co-linear to the ground state KD. First three KDs are purely Ising in nature and next four KDs are strongly axial in nature, suggesting relaxation via highest possible excited state through TA-QTM. Based on this idea, a seven coordinated Dy(III) SIM possessing a blocking temperature of 12 K and which opens hysteresis at 30 K at a 220 Oe/s sweep rate has been reported [210]. Calculations performed on this structure where the equatorially coordinating water molecules are removed leading to two-coordinate Ln(III) yield very high U_{cal} values exceeding 3000 cm^{-1} (Fig. 42). A similar set of conclusions were also arrived by Chibotaru and co-workers on structurally related system [21].

Further, the effect of the L–Ln–L bending angle on the resulting blocking barrier was studied computationally in the model complex $[\mathrm{Dy(cAAc)_2}]^+$ (cAAc = cyclic alkyl amino carbene) (**44**) (Fig. 43(a)) [21]. A high blocking barrier of the resulting model compound was observed at a C–Dy–C bond angle of 180°. However, these studies also indicate that even upon large bending, the magnetic axiality of the resulting two-coordinated structure remains quite high (Fig. 43(b-c)).

2.8. Mono-coordinate lanthanide systems

In principle, the diatomic mono-coordinate complexes, e.g. $[\mathrm{Ln{-}O}]^+$, have the highest possible symmetry, $D_{\infty h}$, among all the coordination complexes. Because of such symmetry, all the B_k^q CF parameters (Eqs. (2) and (4), Section 1.3) with $q \neq 0$ vanishes i.e. the CF perturbation is perfectly uniaxial. If the ligand field is

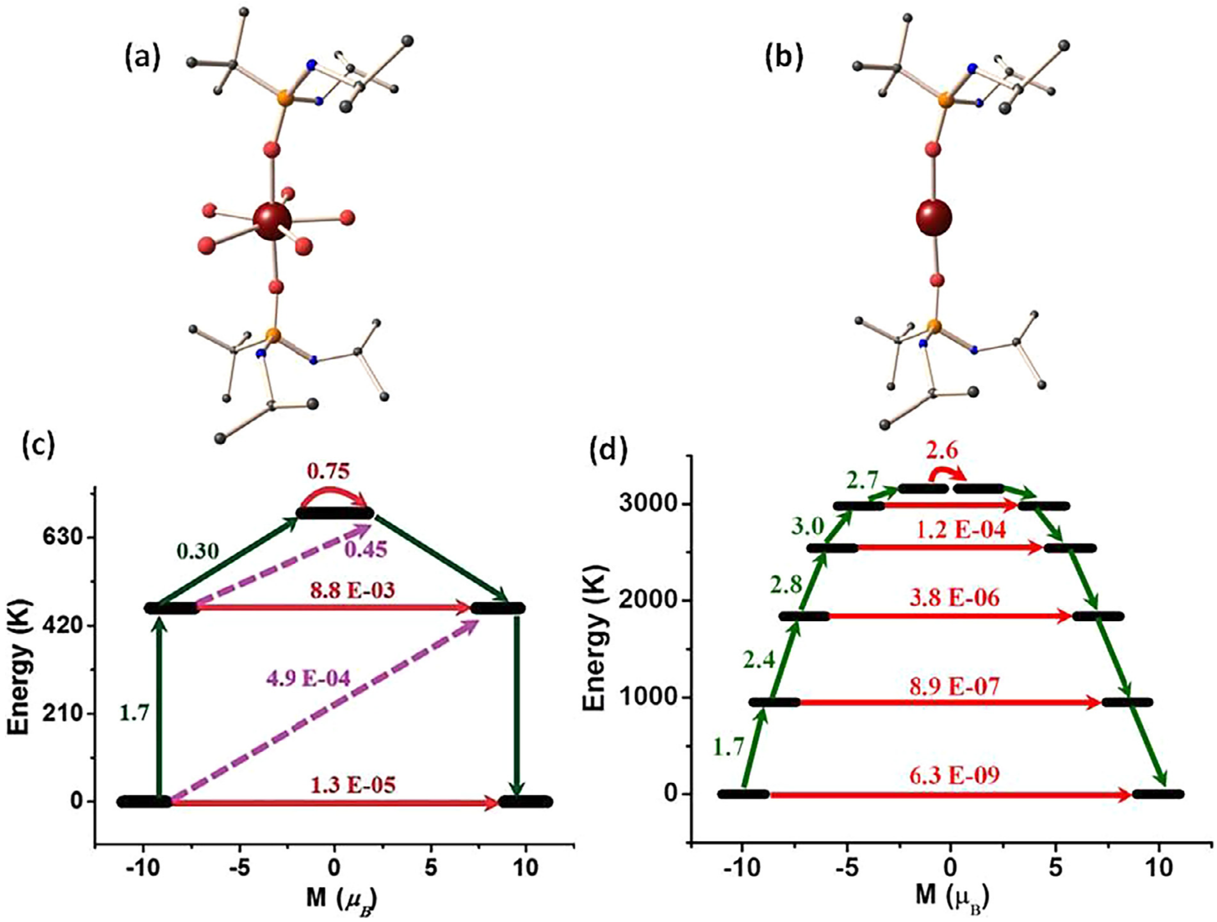

Fig. 42. Molecular structure of a mononuclear Dy-D_{5h} compound with the equatorial water molecules removed (a) and in its initial form (b). The dashed lines show the direction of the main magnetic axis of the corresponding KD. Parts (c) and (d) show the spectrum of CF doublets and the blocking barrier of reversal of magnetization (red arrows) for the corresponding structures. Figure and captions are reprinted from the Ref. [210] with permission from Royal Society of Chemistry.

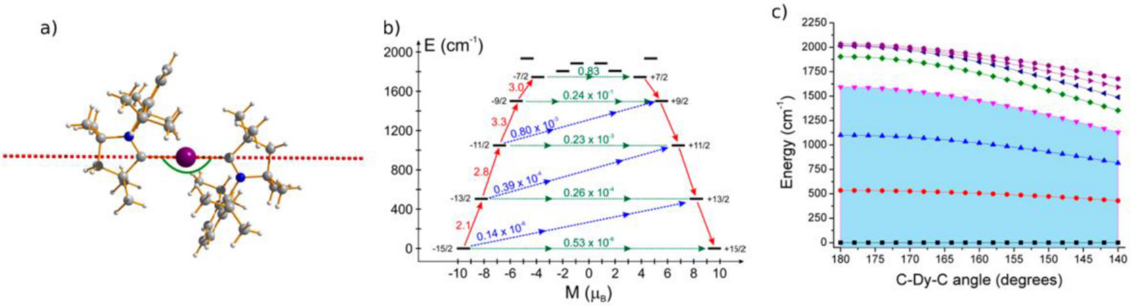

Fig. 43. (a) Structure of the model $[Dy(cAAc)_2]^+$ (**44**) compound. The green arc shows the distortion angle considered here. (b) Magnetization blocking barrier of the undistorted (linear) compound. (c) Evolution of the energy spectrum of the ground-state $M_J = \pm 15/2$ multiplet upon bending of the C–Dy–C angle. The highlighted region defines the blocking barrier. Figure and captions are reprinted with permission from the Ref. [21]. Copyright @ 2016, American Chemical Society.

relatively low and the *Ising* doublets are energetically well separated, all the eigen states could well be described by the total quantum number, *J*, and such axiality holds for all the *Ising* doublets. For such systems, the quantum mechanically allowed transition follows $|\Delta M_J| = 1$. Moreover, the absence of rhombic perturbation eliminates QTM, provided nuclear-spin-biased hyperfine splitting is absent. Therefore, the magnetization relaxation has to take place via climbing through all the possible *Ising* doublet eigen states, which means that the U_{eff} will actually be equal to the height of the double well potential. Therefore, such systems seem to be good targets for realizing very efficient SIMs.

However, the synthetic challenges to stabilize these compounds in the solid-state are significant although such species have been shown to exist in the gaseous phase [211–213]. Ungur and Chibotaru have performed extensive *ab initio* calculations on $[DyX]^{n+}$ species ($n = 1$ for X = O and $n = 2$ for X = F) to investigate their magnetic behaviour [21,159]. These studies revealed that the *Ising* doublet eigen states are arranged following the decreasing order of the M_J values, and the energy spacing, *i.e.*, the higher energy eigen states associate with the lower M_J values, and with the smaller energy spacing between the adjacent eigen states (Figs. 44 and 11). The magnitudes of U_{eff}, which are subject to the bond lengths,

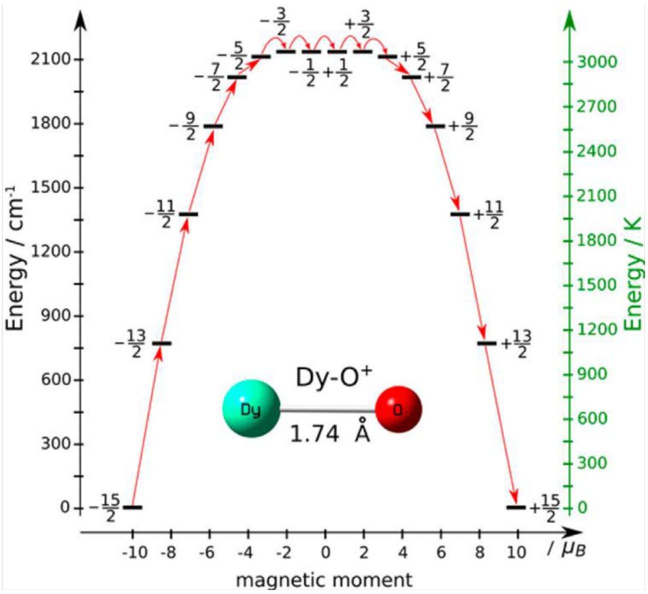

Fig. 44. The energy landscapes of the low-lying *Ising* doublet eigen states for the $[DyO]^+$ complex derived from *ab initio* calculations. Figure and captions are reprinted from the Ref. [159] with permission from Royal Society of Chemistry.

are evaluated to be around 2100 cm^{-1} and 900 cm^{-1} for the $[DyO]^+$ species with Dy–O bond distance = 1.74 Å and for the $[DyF]^{2+}$ species with Dy–F distance = 2.50 Å, respectively.

The same group have further extended their calculations for $[LnO]^+$@MgO ((Ln = Dy and Ho) and $[DyO]^+$@C_{60} in view of the fact that surface-stabilized systems offer the best possibility to prepare practical devices (Fig. 45) [21]. The estimated U_{eff} appears essentially equal to the height of the double well potential for the $[DyO]^+$@MgO system (3600 cm^{-1} at Dy-O bond distance ≈ 2 Å) while the magnetization reversal occurs through excited *Ising* doublet with $M_J = \pm 9/2$ for the $[DyO]^+$@C_{60} system (1900 cm^{-1} at Dy-O bond distance ≈ 2 Å) (Fig. 45). In the case of the Ho analogue, the energy barrier is relatively lower. Detailed *ab initio* calculations on Ln(III)@MgO (Ln = Dy and Ho) exhibited that the doping of $[LnO]^+$ species on metallic surface/clusters/cages endows with more efficient SIM behaviour than the doping of bare Ln atoms [21].

Some of us have performed studies on several lanthanide model complexes with varying coordination number and geometry around Ln(III) ions specifically for Dy(III), Er(III), Ce(III) and other lanthanide ions. Herein, the coordination numbers were varied from 1 to 12 [115,165,214]. In keeping up with the focus of this review, we will discuss results for one oblate (Dy(III)) and one prolate (Er(III)) lanthanide ion models. *Ab initio* calculation on $\{Er(OH)\}^{2+}$ suggests extensive QTM in the ground state while for $\{Dy(OH)\}^{2+}$ model, first four KDs are purely Ising in nature and next

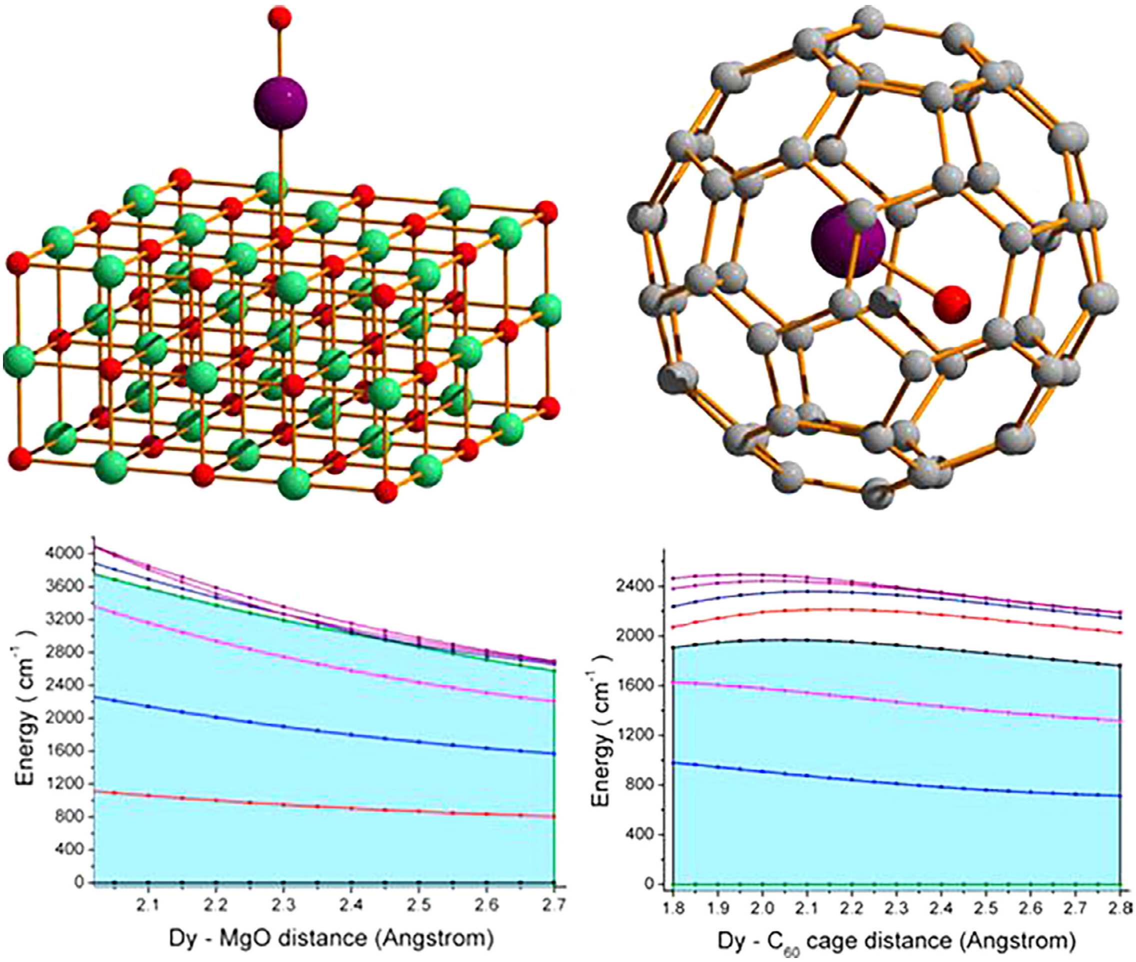

Fig. 45. The *ab initio* optimized geometries of $[DyO]^+$@MgO and $[DyO]^+$@C_{60} (top; colour codes: violet = Dy, green = Mg, red = O and grey = C) and the Dy-O bond length dependent relative energies of the *J* = 15/2 manifolds (bottom). The blue-coloured highlighted area implies effective energy barrier for magnetization reversal. Figure and captions are reprinted with permission from the Ref. [21]. Copyright @ 2016, American Chemical Society.

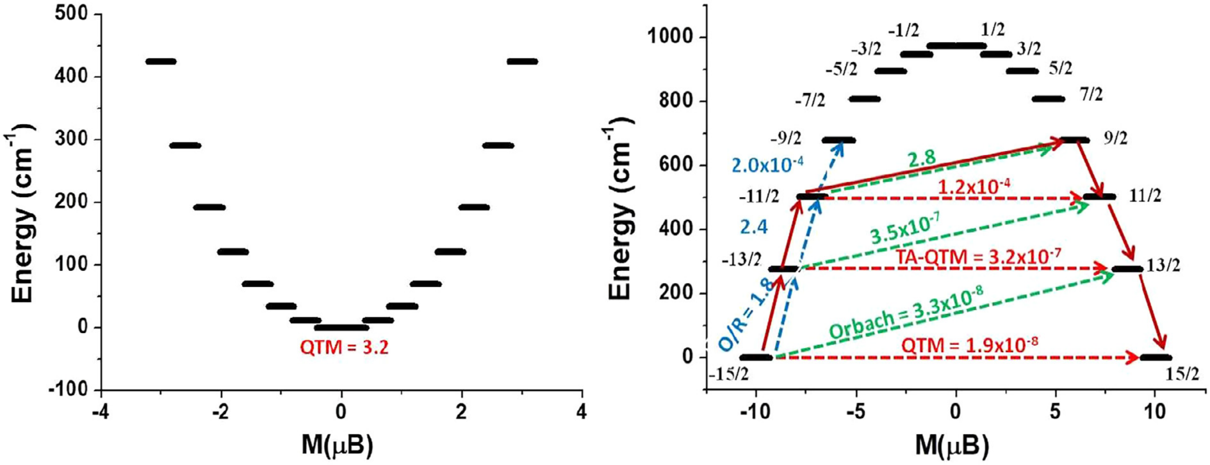

Fig. 46. *Ab initio* SINGLE_ANISO computed magnetization blockade barrier for the $\{Er(OH)\}^{2+}$ and $\{Dy(OH)\}^{2+}$ models (left and right respectively). The x-axis indicates the magnetic moment of each state along the main magnetic axis while the y-axis denotes the energy of the respective states. The thick black lines imply Kramer's doublet as a function of magnetic moment. The dotted green and blue lines indicate the possible pathway of the Orbach/Raman contribution of magnetic relaxation. The brick red arrows indicate the most probable relaxation pathway for the magnetization reorientation. The dotted red lines correspond to the QTM/TA-QTM/tunnelling relaxation contributions between the connecting pairs. The numbers provided at each arrow are the mean value for the corresponding matrix element of the magnetic moment. Plotted from the data given in Ref. [115].

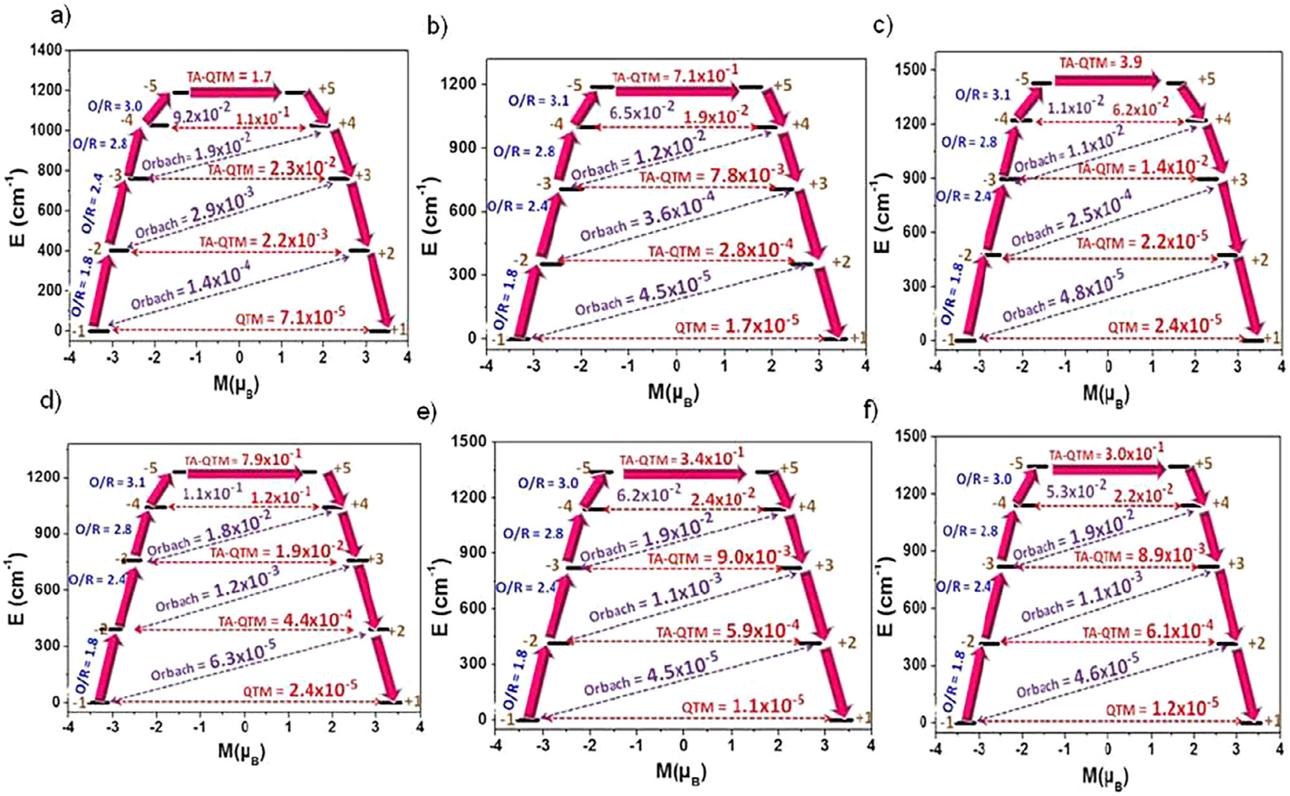

Fig. 47. Qualitative mechanism developed based on *an initio* SINGLE_ANISO calculations for (a) DyOLu@C_{72}; (b) DyOLu@C_{76}-1; (c) DyOLu@C_{76}-2; (d) DyOSc@C_{76}-3; (e) DyOSc@C_{76}-4 and (f) DyOSc@C_{82}. The arrows show the connected energy states, and the numbers represent the matrix element of the transversal magnetic moment (see the text for details). Figure and captions are reprinted from Ref. [215] with permission from Royal Society of Chemistry.

three KDs are strongly axial in nature suggesting relaxation via highest possible excited state. But Orbach relaxation representing off-diagonal elements between $|-11/2\rangle$ $|+9/2\rangle$ state is found to be very large (2.8) causing relaxation via third excited state with U_{cal} value 679 cm^{-1} (Fig. 46). It is important to note that in $\{Dy(OH)\}^{2+}$ models, the Dy-O bond length is larger compared to $(Dy\text{-}O)^+$ reported by Ungur and Chibotaru (2.35 Å *vs.* 1.74 Å respectively). This weakens the strength of axial ligand field in the former and as a consequence the energy separation between ground state KD and excited KDs are found to be smaller with respect to $(Dy\text{-}O)^+$.

Additionally, there are also several one-coordinated Dy(III) ion-based EMFs modelled with various fullerene cages (ranging from C_{72} to C_{82}) and for such species as well the relaxations are found to occur via fourth excited state leading to very large effective energy barriers (Fig. 47) [215]. High symmetry CF environment preserved inside fullerene quenches the QTM till third-excited states, leading to the barrier height as large as 1400 cm^{-1}. In all these EMFs, the ground state g_{zz} axis is found be co-linear to the first three excited states and deviated from collinearity at the fourth excited state. Thermally assisted QTM between fourth excited KD is found to be large enough for relaxation to take place. In $Dy_2O@C_{72}/_{76}/_{82}$, weak exchange coupling between both the lanthanide ions is found to reduce the U_{cal} values. Recently, Popov and co-workers have synthesized two isomers of $Dy_2S@C_{82}$ EMF {$C_{3v}(8)$ and $C_s(6)$} with three ensuing Orbach processes having energy barriers of 7, 33, and 856 cm^{-1} for the former isomer and with two energy barriers of 11 and 364 cm^{-1} for the latter isomer [216]. Oxygen is known to be the stronger ligand compared to sulphur, and the axial ligand field for the former is expected to be stronger. Therefore, Dy_2O@fullerenes are expected to be superior compared to the corresponding sulphur analogues. Besides these examples, other EMF family $LnCN@C_{76/80}$ and $LnSc_2N@C_{80}$ have been reported with very large U_{eff} values. Stronger axial ligand field in these 1-CN EMFs compared to $\{DySc@C_{79}N\}^+$ leads to higher U_{eff} values [151–154]. As the coordinating ligand and the geometry can be easily varied, this area offers a tantalizing possibility to realize higher blocking temperature SIMs.

2.9. Pseudo-sandwich and half-sandwich lanthanide (III) complexes

A sandwich metal complex is referred to the system where the metal ion is accommodated between two multi-dentate (η-type) cyclic ligands, and the centroids of the ligands and the metal ion are almost collinear (Fig. 48). In such complexes, the coordinating atoms of the ligands generally do not involve well-defined classical coordination bonds. Instead, a set of atoms of such a ligand forms altogether an electronic cloud (mostly π-electron cloud) which exerts CF on the metal ion. Consequently, such an η-cyclic ligand with multi-coordination sites can be approximated to a mono-dentate ligand. In view of this analogy, the highly anisotropic ground states of the Ln(III) ions, which are oblate in nature and prefer strongly axial ligand fields, can be stabilized in sandwich complexes. Incidentally, the first discovered Ln-based SIMs were the sandwich complexes where two phthalocyaninates sandwich Ln(III) (Tb/Dy) ions (Fig. 48). Since then, a large number of mono-nuclear double-decker and poly-nuclear multi-decker sandwich complexes have been studied. These studies have been summarized in several review articles [20,23,24,197]. It may not be out of place to point out here that, phthalocyanine/porphyrin type

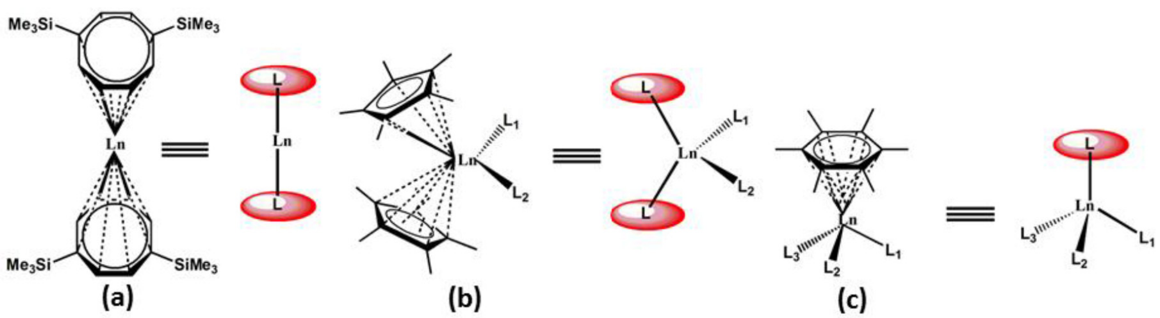

Fig. 48. Schematic structures (left) and their equivalent coordination geometries (right) of the representative examples of sandwich (a; $[Ln(\eta^8\text{-}COT')_2]^-$, (**45**) where COT′ = doubly deprotonated bis(trimethylsylyl)cyclooctatriene), pseudo-sandwich (b; $[(\eta^5\text{-}cp^*)_2Ln(L_1)(L_2)]^+$, (**46**) where cp^* = penta-methyl cyclopentadienyl anion, L_1/L_2 = ligand/solvent/counter anion or their combination) and half-sandwich (c; $[(\eta^6\text{-}C_6Me_6)Ln(L_1)(L_2)(L_3)]^{3+}$, (**47**) where $L_1/L_2/L_3$ = ligand/solvent/counter anion or their combination) complexes.

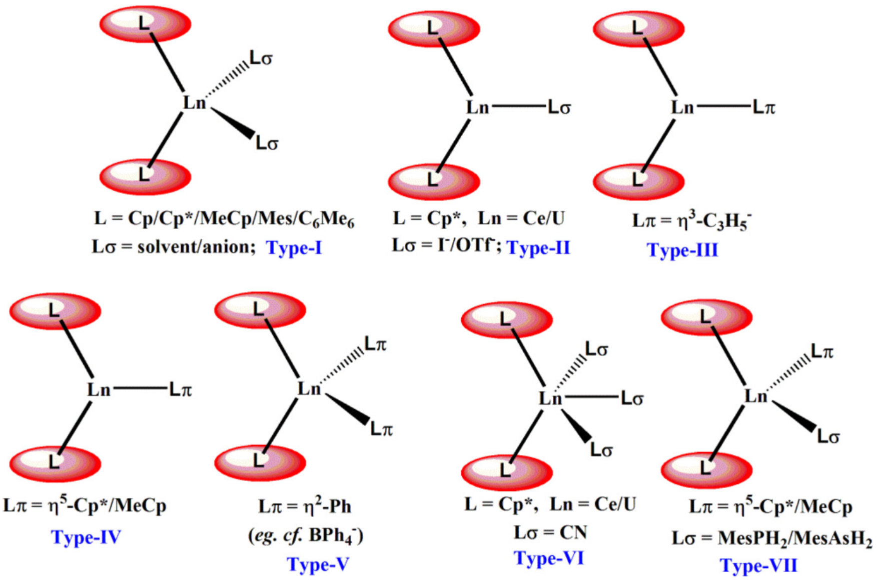

Fig. 49. Schematic structures of the pseudo-sandwich Ln-based complexes (*Types I–VII*) usually employed as building-blocks for the rational synthesis of higher nuclearity systems.

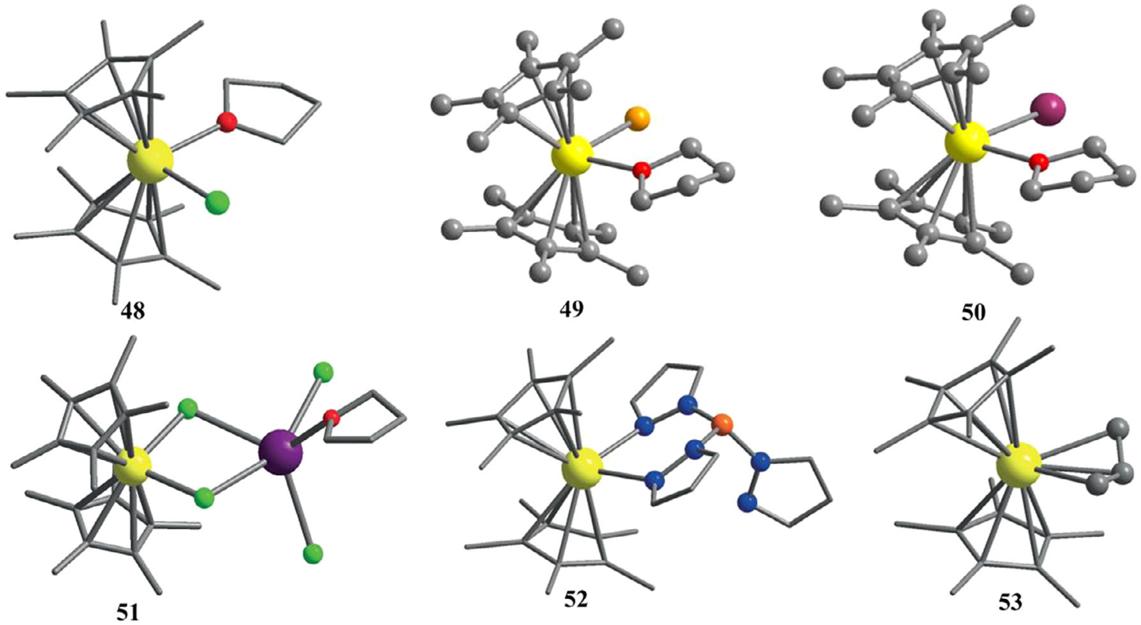

Fig. 50. Single-crystal X-ray structures of the complexes **48**–**53**. For **51**, only the repeat unit of the 1D polymeric chain is shown. For all the complexes, H atoms are omitted for clarity. Figure and captions are reprinted from the Ref. [217] with permission from John Wiley and Sons.

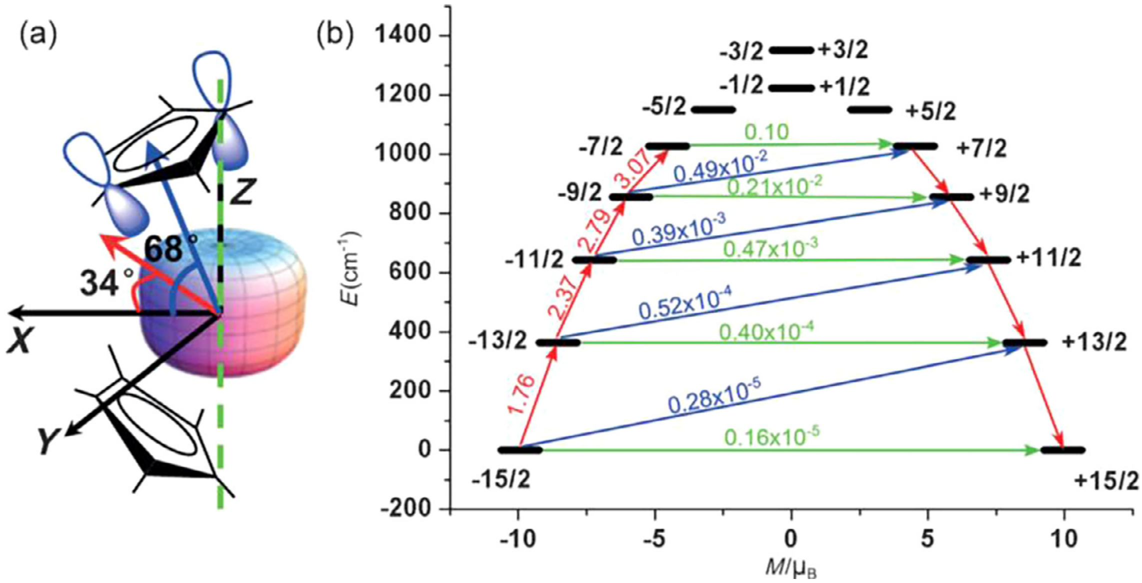

Fig. 51. (a): Schematic representation for the hypothetical species $[\mathrm{Cp}^*_2\mathrm{Dy}]^+$ (**50**). The equatorial plane of the Dy(III) ion is defined by the *XY* plane. The magnetic anisotropic axis (*easy-axis*) of the ground *Ising* doublet eigen states is superimposed with the *Z* axis (the green dashed line), perpendicular to the *XY* plane. The ellipsoid represents the electrostatic potential surface for the ground *Ising* doublet eigen states ($M_J = 15/2$). (b): The energy landscapes of the ground *J* manifold for **54**. The path defined by the red arrows indicates magnetization relaxation *via* Orbach process. The values labelled on the arrows stand for the transition matrix elements corresponding to the respective states connected by the arrows. Figure and captions are reprinted from the Ref. [217] with permission from John Wiley and Sons.

macrocycles are not considered as classical η-type capping ligands because their coordination mode is more σ-type, similar to the multi-dentate chelating ligands. Therefore, the CF symmetry of such a ligand can be regarded as pseudo C_4 symmetric instead of a continuum electronic (π) cloud [32]. On the other hand, magnetic properties of pseudo-sandwich and half-sandwich Ln(III)-based complexes are relatively less explored. Recently, such complexes are attracting a considerable interest in the field of molecule-based magnetism due to their immense potential as magnetic building-blocks (*vide infra*).

2.9.1. Pseudo-sandwich lanthanide (III) complexes

The pseudo-sandwich complexes are similar to the sandwich complexes with an important difference (Fig. 48). In the pseudo-sandwich complexes, additional σ/π-type donors stabilize the complexes (Figs. 48 and 49) [217]. Examples of pseudo-sandwich complexes with one additional σ-type donor (Type-II) [218] or one η-fashioned π-type acyclic donor (Type-III) [217] or one η-fashioned cyclic π-type donor (Type-IV) [219] or two η-fashioned π-type donors (Type-V) [220] or three σ-type donors (Type-VI) [218] or one η-fashioned cyclic π-type donor along with one σ-type donors (Type-VII) [221,222] (Fig. 49) are known. Notably, stabilization of the discrete complexes of Types-II and VI is extremely difficult and therefore, only a few examples are known [218]. However, all of these additional ligands are kinetically labile and thereby enabling these complexes as potential magnetic building-blocks towards the rational synthesis of higher nuclearity systems (*vide infra*).

It is obvious that synthesis of polymetallic systems *via* self-association of building-blocks renders the changes in CF strength and symmetry associated with the accessible coordination sites of the building-blocks. Therefore, in view of molecule-based magnetism, one should be well-aware of the susceptibility of magnetic behaviour (especially, the magnetic anisotropy axis and the low-lying eigen states of the ground *J* manifold of the Ln ions) towards the CF strength and symmetry associated with the accessible coordination sites of the magnetically anisotropic building-blocks. Recently, Gao and co-workers performed extensive investigations, both experimentally and theoretically, on the magnetic properties for a series of complexes of *Type-I* ($[Cp^*_2DyX(THF)]$, X = Cl (**48**); Br (**49**); I (**50**), $[(Cp^*_2DyCl_2KTHF)]_n$ (**51**) and $[Cp^*_2DyTp]$ (Tp = hydrotris(1-pyrazolyl)borate, **52**) and *Type-IV* ($[Cp^*_2Dy(C_3H_5)]$ (**53**)) (Fig. 50) [217]. In addition, they have also investigated theoretically the magnetic property of the complex, $[Cp^*_2Dy]^+$ (**54**; Fig. 51). The principal magnetic parameters of these complexes are summarized in Table 9. For theoretical calculations on the hypothetical species **54**, its geometry was modelled as depicted in Fig. 48. It is predicted that such geometry leads to the stabilization of the highest magnetization eigen states ($M_J = \pm 15/2$) as the ground doublet and they possess oblate electrostatic potential surface (Fig. 51). Moreover, the eigen states are energetically well-separated and almost uniaxial magnetic anisotropy is maintained up to the fourth excited doublet state. Therefore, the magnetization reversal is expected to occur via Orbach process through the fourth excited doublet that is situated at more than 1000 cm^{-1} above the ground doublet. Notably, such a coordination geometry does not exert ideal axial CF perturbation. But interestingly, calculations predict almost complete suppression of QTM for such a scenario. However, introduction of equatorial ligands causes a rhombic CF perturbation which in turn promotes QTM. This, of course, results in the deterioration of the SIM behaviour (Fig. 52). Both the theoretical and experimental U_{eff} values are similar for **50** and **51** and considerably higher than the rest (Table 9). But, the average QTM life times for **51** (70 ms) is found to be significantly larger than that of **50** (6.7 ms), even though the transition matrix elements corresponding to the ground doublets are of same magnitudes (8.3×10^{-4} for **50** and 1.2×10^{-4} for **51**). This can be attributed to the coincidence of higher symmetry and weak CF for **51**. Iodide is a much weaker ligand and thus the overall CF strength is lower for **51**, which accounts for higher U_{eff}. At the same time, presence of two different ancillary ligands, I and THF, lowers the CF symmetry, which contributes to the off-diagonal elements of the matrix representations and thereby promoting QTM. Observation of significantly low U_{eff} values and high QTM for **48**, **49** and **52** follow the same explanation. Slightly slower QTM for **52** (0.6 ms) in comparison with **48** (0.28 ms) can be ascribed to higher CF symmetry for the former. Notably, all but **53** exhibit well-defined slow relaxation of magnetization under zero applied dc field, and magnetic hysteresis loops away from zero-field (Fig. 52 and Table 9). Moreover, there is considerable discrepancy between theoretical and experimental U_{eff} values. Strong interaction between the Ln 4*f* and C_3H_5 π-electrons in the equatorial plane could render such behaviour. This rationale is further supported from the magnetic behaviour of the complexes of *Type-VII*: $[(MeCp)_3Dy(MesAsH_2]^+$

Table 9
Magnetic parameters of the pseudo-sandwich, half-sandwich and sandwich Ln SIMs.

Complex (No.)	U_{cal} (cm^{-1})[†]	U_{eff} (cm^{-1}) (H_{dc}; Oe)[*]	Hysteresis	$T_B(K)$[‡]	Refs.
$[Cp^*_2DyCl(THF)]$ (**48**)	147.2	112 (0)	Yes	2 (19 Oe/s)	[217]
$[Cp^*_2DyBr(THF)]$ (**49**)	165.8	163 (0)	Yes	3 (19 Oe/s)	[217]
$[Cp^*_2DyI(THF)]$ (**50**)	423.1	419 (0)	Yes	4 (19 Oe/s)	[217]
$[(Cp^*_2DyCl_2KTHF)]_n$ (**51**)	414.2	379 (0)	Yes	5 (19 Oe/s)	[217]
$[Cp^*_2DyTp]$ (**52**)	153.8	106 (0)	Yes	2 (19 Oe/s)	[217]
$[Cp^*_2Dy(C_3H_5)]$ (**53**)	91.5	–	No		[217]
$[Cp^*_2Dy]^+$ (**54**)	1027.1				[217]
$[(MeCp)_3Dy(MesAsH_2]^+$ (**55**)	43.9	8 (0; dil.)	Yes	~1.8 (30.6 Oe/s)	[221]
$[(MeCp)_3Dy(MesPH_2]^+$ (**56**)	45.2	undetectable	–	–	[222]
$[(Tp^*)Tm(COT)]$ (**58**)	406.5	32 (2k)	No		[224]
$[(Tp)Tm(COT)]$ (**59**)	394.7	77.1 (2k)30.6 (0; dil.)75.1 (1k; dil.)	No		[224]
$[Cp^*Yb(DAD)(THF)]\cdot C_7H_8$ (**60**)	–	13.85 (1.5 k)	–	–	[225]
$[(C_6Me_6)Dy(AlCl_4)_3]$ (**61**)	80.4	70.2 (0)89 (2k)	Yes	3 (200 Oe/s)	[226]
$[(Cp^*)Dy(COT)]$ (**65b**)	24.3	17.6 (1k)[a]	No	–	[227]
$[(Cp^*)Ho(COT)]$ (**65c**)	80.6	23.5 (6k)[a] 17 (6k)[a]	No	–	[227]
$[(Cp^*)Er(COT)]$ (**65d**)	189.4	224.5 (0)136.9 (0)	Yes	5 (9.2 Oe/s)[a]	[227,228]
$[Dy(COT'')_2Li(THF)(DME)]$ (**66a**)	–	12.5 (0)29.9 (600)	No	–	[229]
$[Li(DME)_3][Dy(COT'')_2]$ (**66b**)	15.6[b]	17.4 (0)	No	–	[230]
$[Li(DME)_3][Er(COT'')_2]$ (**67**)	–	129.9 (0)	Yes	8 (22 Oe/s)	[24]
$[K(18\text{-}crown\text{-}6)][Dy(COT)_2]$ (**68**)	19	7.6 (0)	No	–	[71]
$[K(18\text{-}crown\text{-}6)][Er(COT)_2]$ (**69**)	180.6	198.7 (0)	Yes	12 (35 Oe/s)	[71]
$[K_2Er_2(COT)_4(THF)_4]$ (**70**)	–	212.6 (0)	Yes	12 (18Oe/s)	[24]
$[KEr_2(\eta 7\text{-}C_7H_7)(N(SiMe_3)_2)_4]$ (**71**)	–	40.3 (800)	No	–	[24]
$[(Cp^{ttt})_2Dy][B(C_6F_5)_4]$ (**72**)	1156	1277 (0)	Yes	60 (39 Oe/s)	[67]

[†] The most probable theoretical excitation energy for magnetisation reversal.
[*] Experimentally observed energy barrier for magnetization reversal.
[‡] The blocking temperature expressed through ZFC susceptibility at H_{dc} (kOe), or/and hysteresis at ΔH (Oe/s) or/and average life-time τ (s) study.
[a] The hysteresis measurements are carried out on magnetically diluted sample.
[b] The energy is calculated for the symmetrized $Dy(COT)_2$ Model.

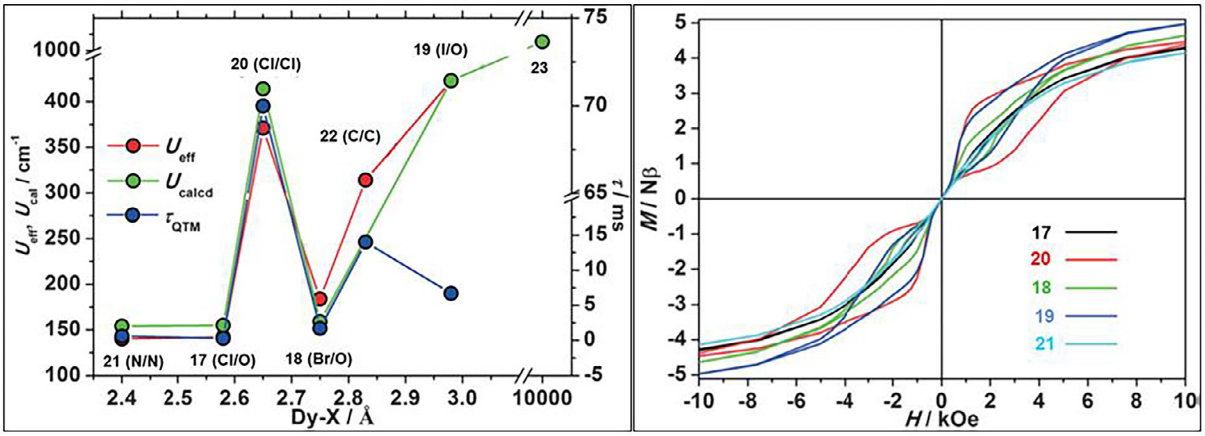

Fig. 52. *Left*: Relative effective energy barriers (experimental, U_{eff}, and theoretical, U_{calcd}) and the average lifetime for magnetization reversal through QTM of the complexes **48**–**54** as a function of Dy-ancillary ligand atom distance. *Right:* Magnetic hysteresis of the complexes at a field sweep rate of 19 Oe/s. Figure and captions are reprinted from the Ref. [217] with permission from John Wiley and Sons.

(**55**)and $[(MeCp)_3Dy(MesPH_2]^+$ (**56**) (Mes = mesitylene) [221,222]. In **55** and **56**, one of the η^5-cyclopentadienyl moieties can be considered as an ancillary π-ligand in conjunction with σ-ligand arsine/phosphine. Therefore, the Ln *4f* electrons in the equatorial plane interact strongly with the ancillary ligand electrons rendering strong CF strength. Moreover, such a structure leads to CF asymmetry. Theoretical calculations revealed very low U_{eff} values ($\approx$40 cm^{-1}, Table 9). While magnetically diluted samples of **55** exhibited zero-field U_{eff} = 8 cm^{-1}, no well-defined magnetization blocking was detected for **56** above 1.8 K. Such a difference can rationally be assigned to stronger σ donating behaviour of $MesPH_2$ in comparison to $MesAsH_2$.

Detailed magnetic investigations on a series of divalent Ln complexes of the general formula $[K(2.2.2\text{-cryptand})][Cp'_3Ln]$ (**57**) (Ln = Y, La, Ce,Pr, Nd, Sm, Eu, Gd, Tb, Dy, Ho, Er, Tm; Cp′ = $C_5H_4SiMe_3$) and on analogous trivalent Ln complexes revealed no detectable slow relaxation of magnetization for any of the above members [223]. It can thus be concluded that pseudo-sandwich complexes with Ln ions whose electrostatic potentials of the ground doublets are oblate in nature and prefer strong axial CF, can be potential building blocks if the accessible coordination sites in the equatorial planes experience low CF strength and high CF symmetry. On the other hand, Ln ions with prolate electrostatic potentials in their ground doublets are not preferable candidates for building-blocks. For such ions, a stationary, strong CF ligand environment in equatorial planes and accessible coordination sites in axial positions seem to be the option [33].

2.9.2. Half-sandwich lanthanide complexes

In half-sandwich complexes, metal ions are capped by one η-type ligand keeping the other side of the metal ions bare for coordination with ancillary ligands (Fig. 48). The versatility of this class of complexes lies in the fact that the stationary, strong ligand (the capping ligand) occupies only one side of the lanthanide ion allowing various types of ligands with a wide range of geometrical needs to access the metal ion and hence depending on the ligand both prolate and oblate Ln(III) ions can be stabilized [225,226]. Half-sandwich lanthanide complexes have already proved to be potential magnetic building-blocks towards the construction of various multi-decker sandwich SMMs [24,231]. Such half-sandwich complexes can be stabilized by three additional (ancillary) σ-type donors. But, in most of the cases, especially when steric bulk of the ligands permits, these exist as dimers as depicted in Fig. 50 [232]. However, the number of examples for such discrete half-sandwich complexes where extensive magnetic properties have been investigated is quite sparse (Fig. 53).

Cyclooctatetraenide (COT)$^{2-}$ and tris-pyrazolylborate derivatives (Tp = hydrotris(1-hyrazolyl)borate; Tp* = hydrotris(3,5-dimethyl-1-pyrazolyl)borate)[(Tp*)Tm(COT)] (**58**) and [(Tp)Tm(COT)] (**59**) are examples of complexes containing one face covered with a π-type ligand and the other side with a different ligand system (Fig. 54) [224]. Surprisingly, **58** exhibits significantly low energy barriers with a fast QTM compared to **59** (Table 9) in spite of similar geometry. Detailed investigations revealed that both the complexes associate with almost degenerate ground eigen states ($\Delta E_{(MJ=\pm6)}$ = 0.023 cm^{-1} for **58** and 0.012 cm^{-1} for **59**) with the largest magnetization moments (M_J = 6) (Fig. 54). Moreover, the electrostatic potentials surfaces for the ground doublets for these complexes are prolate in nature and involve uniaxial magnetic anisotropy (g_{xx} = g_{yy} = 0 and g_{zz} = 13.959 for **58** and 13.964 for **59**). The direction of the magnetic anisotropy axes is also similar as depicted in Fig. 54.

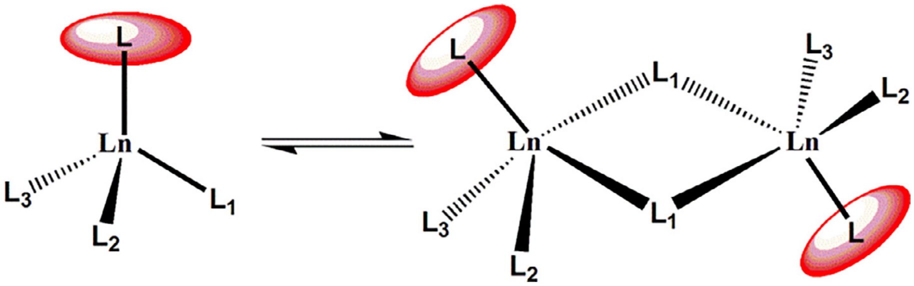

Fig. 53. Schematic representation for the equilibrium between the monomeric and dimeric forms of the half-sandwich complexes.

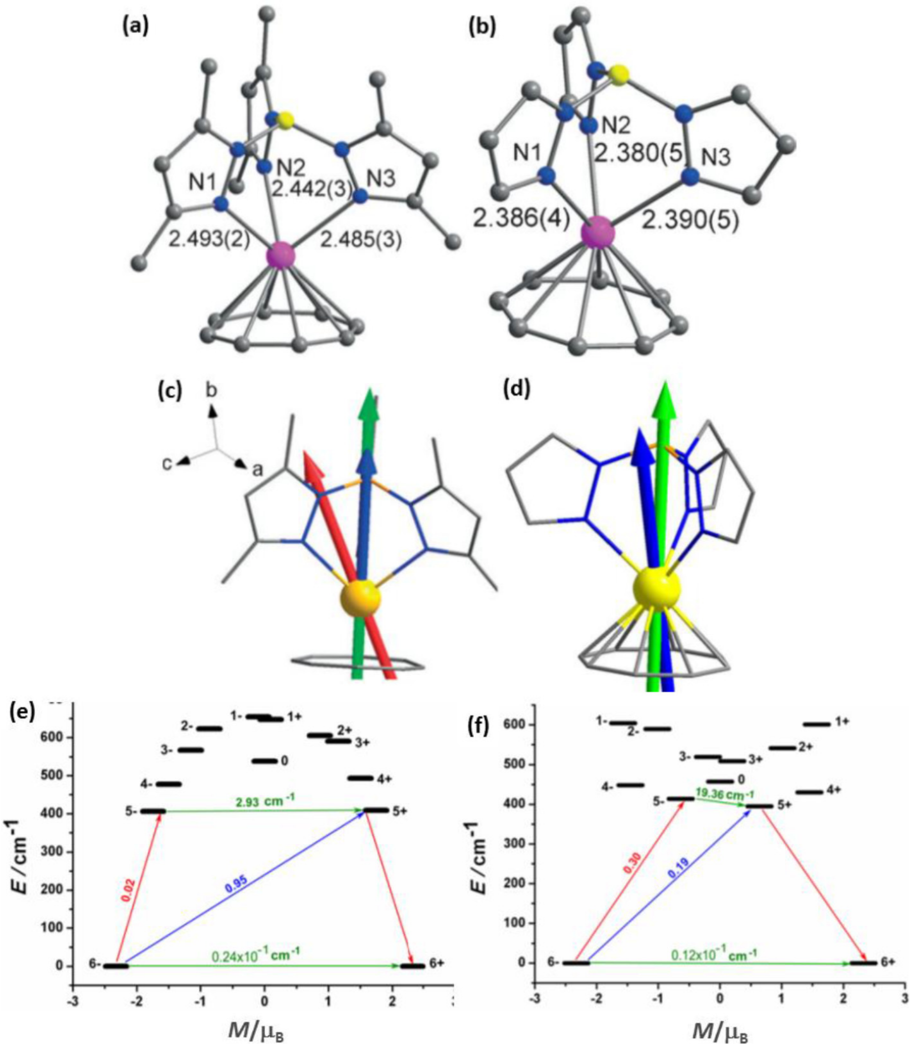

Fig. 54. Single-crystal X-ray structures of **58** (a) and **59** (b); the side views of the magnetic *easy-axes* of the ground doublets of **58** (c) and **59** (d) determined through experiment (red), CACSCF theory (green) and electrostatic model (blue); the calculated energy landscapes of the ground *J* manifolds for **58** (e) and **59** (f). Figure and captions are reprinted from the Ref. [224] with permission from John Wiley and Sons.

Though the topology of energy landscapes for their ground *J* manifolds are completely different, the magnetization reversal via Orbach process is predicted to occur through the first excited states with similar energy barriers (406.5 cm^{-1} for **58** and 394.7 cm^{-1} for **59**) (Fig. 54). The striking difference lies in the transition matrix elements corresponding to the ground and first excited states which are: 0.024 (**58**) and 0.012 (**59**); 0.02 (**58**) and 0.3 (**59**); and 2.93 (**58**) and 19.36 (**59**) corresponding to the ground doublets; ground and first excited Zeeman states; and first excited doublets, respectively. Moreover, the spin lattice relaxation is also one order of magnitude higher for **58** than **59**. Such differences can be attributed to the loss of CF symmetry due to the presence of methyl substituent's in the pyrazolyl moieties in **58**. Stabilization of prolate ions is further evidenced in the half-sandwich complex [Cp*Yb(DAD)(THF)]·C_7H_8 (**60**) (where DAD stands for 2,6-$Me_2C_6H_3N{=}CHCH{=}C_6H_3Me_2$-2,6) [225]. **60** exhibits a field-induced SIM behaviour with $U_{eff} = 13.85\ cm^{-1}$ under $H_{dc} = 1.5$ kOe. On the other hand, stabilization of an oblate ion in half-sandwich complex can be demonstrated with the detailed magnetic investigations for $[(C_6Me_6)Dy(AlCl_4)_3]$ (**61**) (Fig. 55) [226]. Thorough *ab initio* calculations displayed stabilization of eigenstates with $M_J = \pm 15/2$ as the degenerate ground doublet that associates with oblate electrostatic potential surface. Moreover, the ground states are anisotropically almost uniaxial ($g_{xx} = 0.01455$, $g_{yy} = 0.0258$ and $g_{zz} = 19.6985$) and the magnetic *easy-axis* coincides with the centroid of the capping COT ligand (Fig. 55). Detailed ac magnetic susceptibility studies revealed SIM behaviour for **61** complying with the theoretical predictions (Table 9). It is worth pointing out that the isostructural Tb analogue $[(C_6Me_6)Tb(AlCl_4)_3]$ (**62**) does not display SIM behaviour [226]. Theoretical investigation predicts different orientation of the easy-axis (Fig. 55), which is perfectly uniaxial though ($g_{xx} = g_{yy} = 0$, $g_{zz} = 16.4483$). The eigen states are admixed to deviate from double degeneracy ($\Delta E = 0.1$ cm^{-1} for the lowest two eigen states). However, the first excited nearly doublet (($\Delta E = 0.4\ cm^{-1}$) is situated above approximately 23 cm^{-1} from the ground state. Such a difference in energy landscapes and orientation of *easy-axis* can be assigned to the difference in electrostatic potential surfaces of their ground doublets [33]. Gao and co-workers have studied the magnetic behaviour of a series of half-sandwich complexes with the general formula $[(L_{OEt})Ln(TPP)]$ (**63**) and $[(L_{OEt})Ln(Pc)]$ (**64**) (where $L_{OEt} = [(\eta^5\text{-}C_5H_5)Co\{P(=O)(OEt)_2\}_3]^-$, TPP = 5,10,15,20-tetraphenylporphyrinate, Pc = phthalocyaninate and Ln = Gd, Tb, Dy, and Ho) [233]. None of the above members display zero-field SIM behaviour.

However, all the Tb and Dy analogues exhibit field-induced SIM behaviour. In the case of capping TPP complexes **63**, the Tb

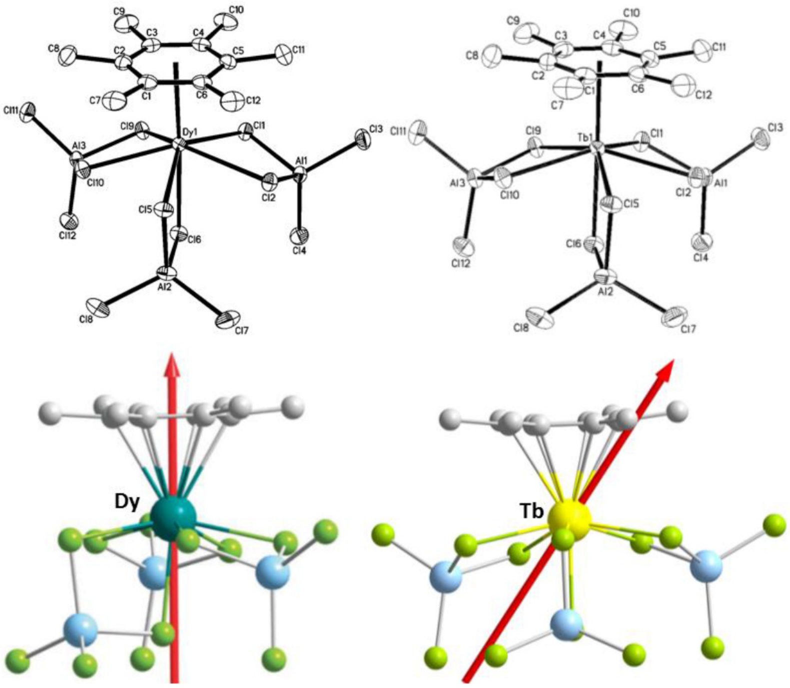

Fig. 55. Single-crystal X-ray structures (top) and relative orientations of the magnetic *easy-axes* (red arrows) (bottom) of the complexes **61**(left) and **62**(right). Colour codes: Dy = magenta; Tb = Yellow; Al = cyan; green = Cl and grey = C. H atoms are omitted for clarity. Figure and captions are reprinted from the Ref. [226] with permission from Royal Society of Chemistry.

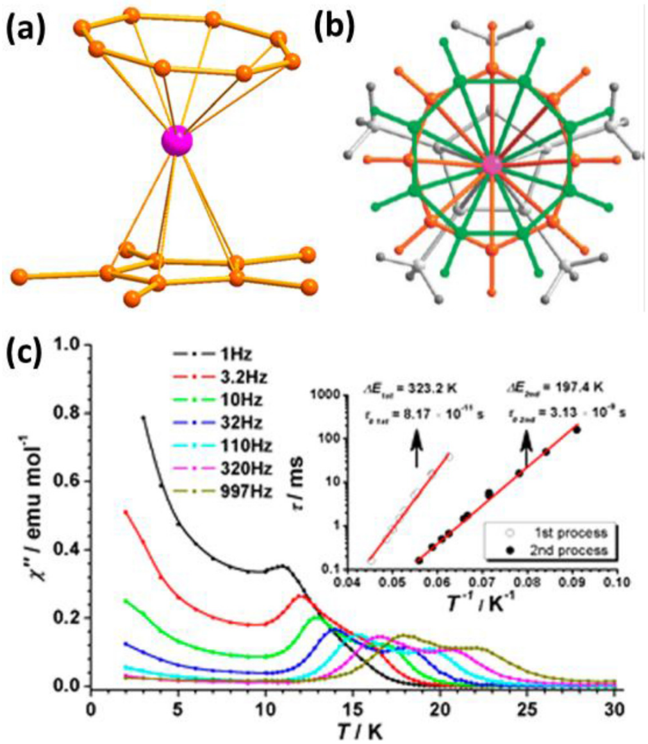

Fig. 56. Single-crystal X-ray structure (a) and relative orientations of the capping Cp* and COT ligands (b) of **65d**, as the representative structural models for the complexes **65a**–**e**. H atoms are omitted in (a) for clarity. Colour codes: Er = pink and orange = C. In (b), the orange and green colourations represent crystallographically two different conformational positions of the COT ligand with respect to the Cp* ligand (grey). In (c), variable temperature variable frequency molar *out-of-phase* ac susceptibility (χ'') under $H_{dc} = 0$ and the Arrhenius plots (*inset*) of **65d**. Figure and captions are reprinted with permission from the Ref. [227]; Copyright @ 2012, American Chemical Society, and the Ref. [228]; Copyright @ 2011, American Chemical Society.

analogue is found to be slightly better candidate than the Dy one (U_{eff} (cm^{-1}) = 11.4 (Tb) and 5.9 (Dy)). On the other hand, for the case of capping Pc complexes **64**, it is found to be otherwise (U_{eff} (cm^{-1}) = 13.2 (Tb) and 16.4 (Dy)). However, in both the cases, the coordinating atoms of the capping ligands (TPP or Pc) are more towards the equatorial plane in comparison to the complex **61**. Therefore, this coordination environment stabilizes the ground states of Tb. On the other hand, due to different orientation of *easy-axis*, it destabilizes the ground states for Dy(III) ion. Moreover, structural distortions also add significantly to QTM for these classes of complexes.

2.9.3. Cycloalkenyl-capped sandwich lanthanide complexes

As mentioned in the earlier sections, slow dynamics of magnetization in Ln(III)-based mononuclear complexes were first reported for a couple of sandwich complexes where the Ln ions are sandwiched between two phthalocyacine (Pc) ligands [36]. Therefore, the initial thrust of research for efficient Ln(III)-based SIMs was directed towards exploring hierarchical phthalocyanine/-porphyrin based sandwich/double-decker complexes of Ln(III) ions and the detailed advances of such complexes are covered in several elaborative review articles [23,24,29,31,197]. Moreover, these phthalocyanine/porphyrin based complexes actually could be considered as coordination complexes with precise coordination numbers, ca. CN = 8 for the $[Pc_2Ln]^-$ complexes [32]. However, this section is devoted to highlight the representative cycloalkenyl-capped Ln(III)-based mononuclear sandwich complexes that exhibit very good SIM behaviour. Gao, Wang and co-workers have investigated extensively the magnetic behaviour of a series of hetero-capped sandwich complexes with the general formula [(Cp*)Ln(COT)] (where Cp* = pentamethylcyclopentadienyl anion; COT = cyclooctatetraenyldianion; Ln(III) = Tb (**65a**); Dy (**65b**); Ho (**65c**); Er (**65d**); Tm (**65e**)) [227,228]. The single-crystal X-ray structural analyses revealed that the COT ligand is thermally disordered over crystallographically two different conformational positions with respect to the Cp* ligand (Fig. 56). Moreover, the centroids of the rings of the capping ligands and the Ln centre are not co-linear. The centroid(COT)-Ln-centroid(Cp*) angles are measured to be 170.4, 171.9, 173.0, 174.0, 173.9 and 173.0° for **65a**–**e**, respectively [227].

Among these complexes, the Dy(III) (**65b**), Ho(III) (**65c**) and Er (III) (**65d**) analogues exhibit SIM behaviour, with strikingly high efficiency for **65d** compared to the other analogues (Table 9). Ac magnetic susceptibility studies for **65d** showed distinct maxima in *out-of-phase* ac susceptibility (χ'') even in the absence of applied dc magnetic field. On the other hand, the Dy(III) and Ho(III) analogues require applied dc magnetic fields to display clear maxima in the corresponding *out-of-phase* ac susceptibility (χ'') plots. The solid samples of both the Ho(III) and Er(III) analogues exhibit two relaxations for magnetization reversal, which could be attributed to crystallographically two different conformational positions of COT ligand (Fig. 56 (b)). However, the effective energy barriers for magnetization reversals for **65d** (224.5 and 136.9 cm^{-1}, $H_{\text{dc}} = 0$) are significantly larger than **65b** (17.6 cm^{-1}, $H_{\text{dc}} = 1$ kOe) and **65c** (23.5 and 17 cm^{-1}, $H_{\text{dc}} = 6$kOe). Moreover, distinct opening of magnetic hysteresis loops near zero dc field is also observed only for the former (Fig. 57 (c)). To understand such magnetic behaviour, detailed *ab initio* calculations were performed considering $C_{\infty v}$ CF symmetry. It is found that such CF symmetry stabilizes *Ising*-ground doublet with the highest possible magnetization moment ($M_J = \pm 15/2$) for the Er(III) analogue (Fig. 57 (b)). Moreover the eigen states of its ground *J* manifold are energetically quite well separated and they are essentially axial in nature. The first excited doublet ($M_J = \pm 13/2$) is situated above around 189 $\text{cm}^{-1}$from the ground doublet. The orientation of the easy axis of magnetization is as shown in Fig. 57 (a). On the other hand, the energy gaps corresponding to the first excitation for the Dy(III) (24.3 cm^{-1}) and Ho (III) (80.6 cm^{-1}) analogues are found to be significantly lower. Moreover, the ground doublet for Dy(III) analogue associates with $M_J = \pm 9/2$ though the energy landscape of the Ho(III) analogue is *Ising*-type stabilizing the highest magnetic ground state ($M_J = \pm 8$). Notably, such CF symmetry stabilizes the singlet ground state for the Tb(III) analogue (Fig. 57 (b)). In the case of the Tm(III) analogue, though the ground eigen-doublet associates with the highest magnetization moment ($M_J = \pm 6$), the first excited doublet is a singlet ($M_J = 0$), and thereby the excitation is quantum mechanically forbidden. Therefore, none of the Tb(III) and Tm(III) analogues display slow relaxation of magnetization. In order to have further insights, Sessoli and co-workers have employed angular-resolved magnetometry to investigate the molecular magnetic behaviour of **65d** [234,235]. Detailed investigation agrees well with the theoretical predictions. Stabilization of the highest magnetic state with axial ionic magnetic anisotropy can well be justified by the effective charge displacement consideration [39]. However, narrow opening of magnetic hysteresis loops for **65d** and the absence of magnetic hysteresis loops for **65b** and **65c** could be attributed to strong QTM. In addition to the lower symmetry due to two different capping ligands, tilting of the caps reduces the CF axiality and thereby enhancing QTM [236].

Sandwiching Ln(III) ions between COT or substituted COT capping ligands induces interesting magnetic behaviour. Murugesu et al. have investigated detailed magnetic behaviour of the

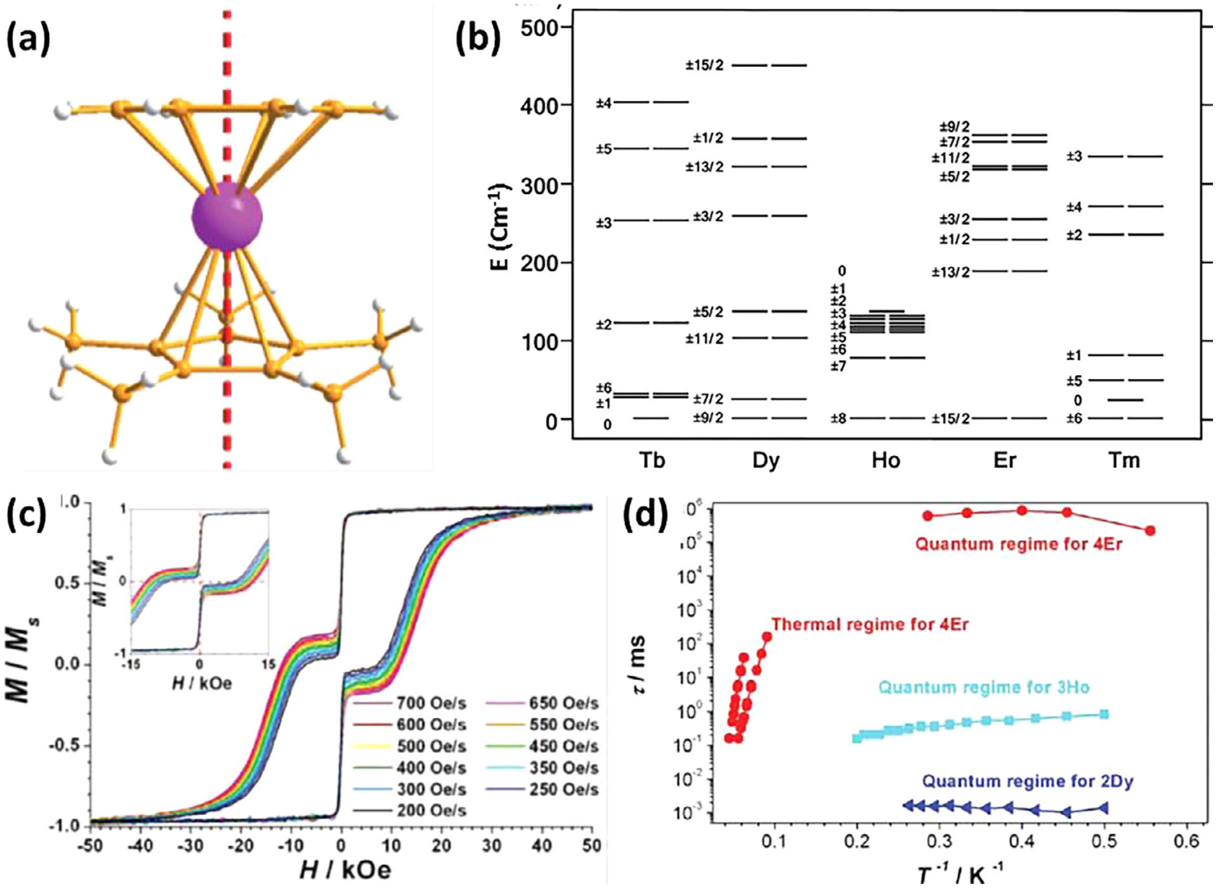

Fig. 57. (a) Relative orientation of the theoretically predicted easy axis of magnetization (red dotted line) with respect to the local axis for **65d**. (b) The energy landscapes of the ground *J* manifolds for **65a**–**e**. (c) Sweep rate dependent hysteresis loops for the magnetically diluted sample of **65d**. (d) Temperature dependent time constants (t) for slow relaxation of magnetizations for **65b** (blue), **65c** (cyan) and **65d** (red). Figure and captions are reprinted with permission from the Ref. [227]; Copyright @ 2012, American Chemical Society, and the Ref. [234] with permission from John Wiley and Sons.

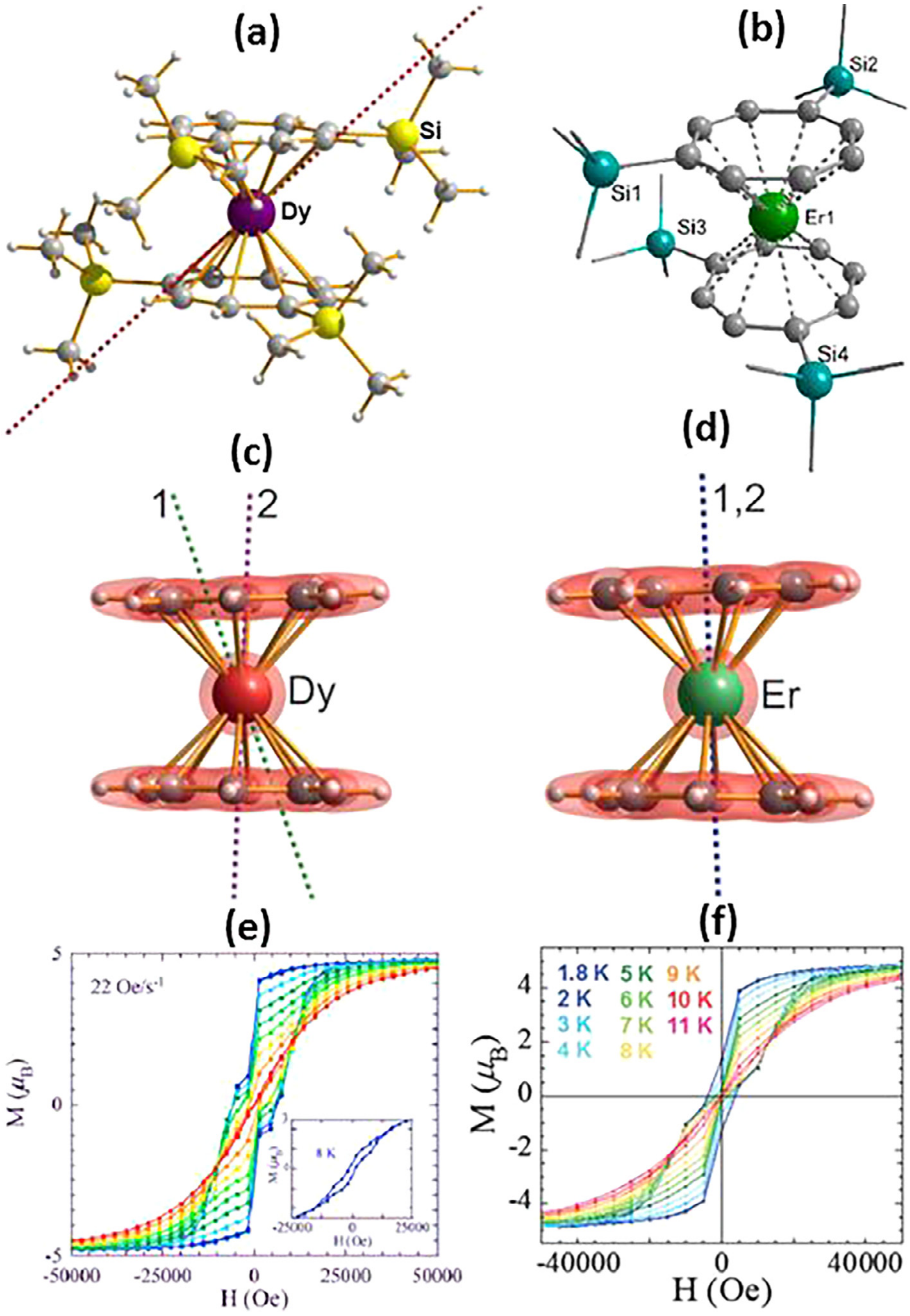

Fig. 58. Single crystal X-ray structures of **66b** with easy-axis (the violet dotted line) of magnetization for the ground doublet (a); **67** (b); **68** with easy-axes (green and violet dotted lines) of magnetization for the ground (1) and first excited (2) doublets (c); **69** with easy-axes (blue dotted lines) of magnetization for the ground (1) and first excited (2) doublets (d). Colour codes for the unlabelled atoms: H = off white and C = grey. The easy-axes of magnetization are calculated with respect to the local ionic coordinates. The magnetic hysteresis loops for **67** (e) and **69** (f). Figure and captions are reprinted with permission from 'the Ref. [230]; Copyright @ 2013, American Chemical Society, and the Ref. [71] with permission from John Wiley and Sons.

complexes [{Dy(COT″)$_2$}{Li(THF)(DME)}] [229] (**66a**), [Li(DME)$_3$][Ln(COT″)$_2$] [230] (where Ln = Dy (**66b**) and Er (**67**); COT″ = 1,4-bis(trimethylsilyl)cyclooctatetraenyldianion) and [K(18-crown-6)][Ln(COT)$_2$] (Ln = Dy (**68**) and Er (**69**)) [71]. The representative molecular structures of these complexes are portrayed in Fig. 58. Single-crystal X-ray analyses revealed that the molecular structure of **66a** is similar to **66b** except that the Li ion of the Li(THF)(DME) moiety coordinates with one of the COT″ rings in the case of the former [229]. However, in all these complexes, the centroids of the capping COT rings and the Ln(III) centre are almost co-linear. Therefore, if one ignores the substituents on the COT″ capping ligands or the Li(THF)(DME) moiety, it is apparent that the Ln(III) experience identical CF. As we saw in the preceding discussion for the [Ln(COT)(Cp*)] systems, the easy-axis for magnetization falls along the pseudo-symmetry axis. Thus, one could intuitively expect a stronger axiality of magnetic anisotropy owing to higher axial CF symmetry in the cases of doubly COT or COT″ capped Ln complexes. Therefore, eigen states with oblate electrostatic potential surfaces are expected to be favoured. But, interestingly, the slow dynamics of magnetization for Dy(COT)$_2$ or Dy(COT″)$_2$ systems are found to be similar to the [Dy(COT)(Cp*)] systems (Table 9). This implies dominating influence of CF strengths over CF symmetry for these systems. On the other hand, the Er(III) analogues **67** and **69** are found to exhibit markedly efficient SIM

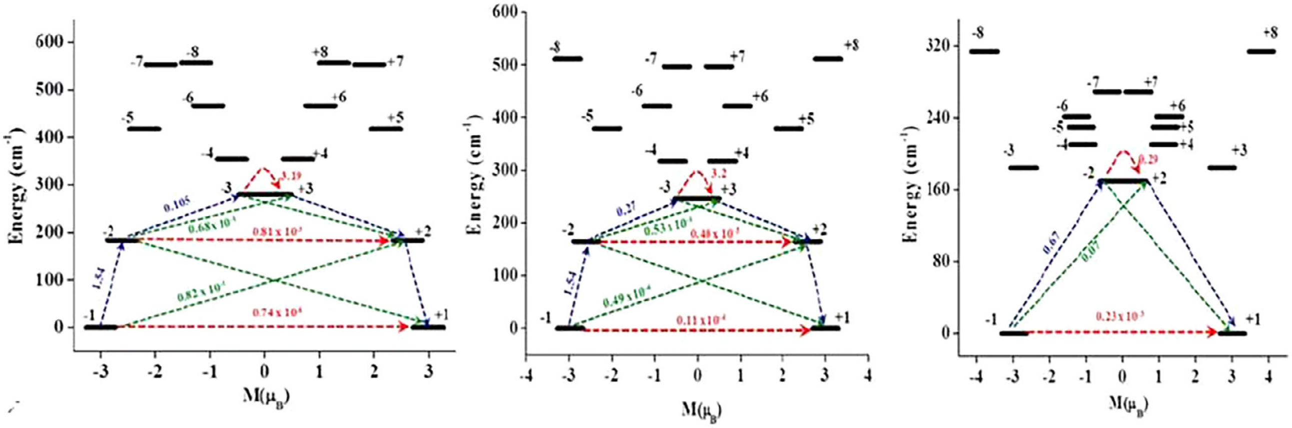

Fig. 59. *Ab initio* computed magnetic blocking barrier for **67**(left), **68**(middle) and {Er(COT)cp*} (right) complexes. The thick black line indicates the Kramers doublets (KDs), as function of magnetic moment. The dotted green lines show the possible pathway of the Orbach process. The dotted blue lines show the most probable relaxation pathways for magnetization reversal. The dotted red lines represent the presence of QTM/TA-QTM between the connecting pairs. The numbers provided at each arrow are the mean absolute value for the corresponding matrix element of transition magnetic moment Figure and captions are reprinted with permission from the Ref. [230]; Copyright @ 2013, American Chemical Society; the Ref. [227]; Copyright @ 2012, American Chemical Society, and the Ref. [71] with permission from John Wiley and Sons.

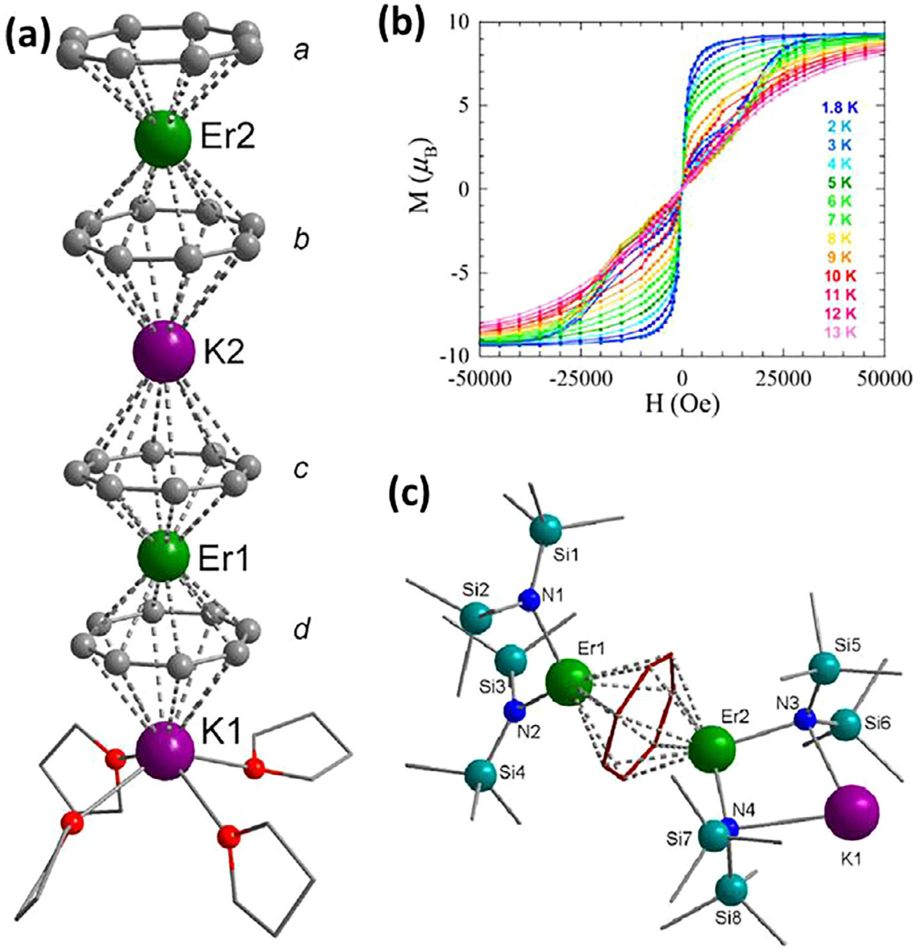

Fig. 60. Single crystal X-ray structures of **70** (a) and **71** (c). H atoms are omitted for clarity. Colour codes: C = grey; N = blue; O = red; Si = magenta; K = violet and Er = green. The magnetic hysteresis loops of **70** (b). Figure and captions are reprinted with permissions from the Ref. [24]. Copyright @ 2016, American Chemical Society.

behaviour with the effective energy barriers for magnetization reversal U_{eff} = 129.9 and 198.7 cm^{-1}, respectively, at H_{dc} = 0, and magnetization blocking temperature T_{B} = 8 K at 22 Oe/s sweep rate and 12 Kat 35Oe/s sweep rate, respectively.

The effective energy barriers for magnetization reversal for the Dy(III) analogues **66a**, **66b** and **68** are measured to be 12.5, 17.4 and 7.6 cm^{-1}, respectively, at zero applied field. However, employment of applied dc fields increases slightly the effective energy

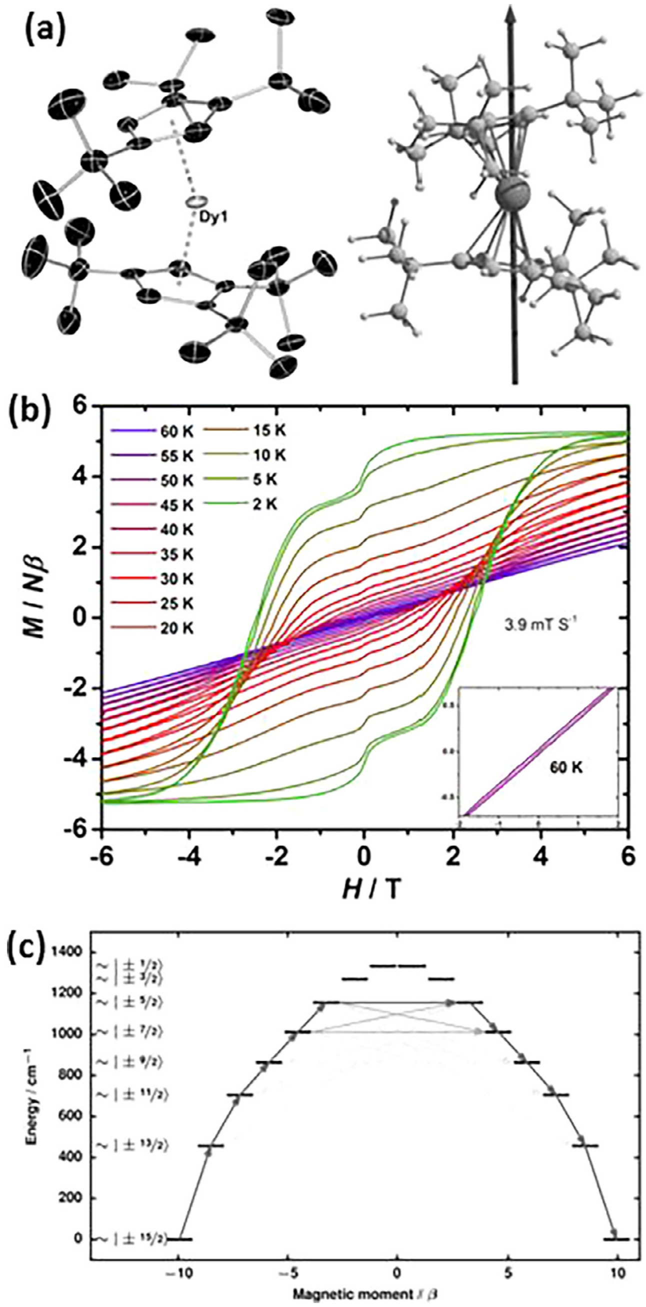

Fig. 61. (a) The ORTEP diagram (with 50% ellipsoid probability) of the single crystal X-ray structure (left) and the model displaying theoretically predicted relative orientation of easy-axis (solid arrow) of magnetization of **72**. H atoms are omitted from the crystal structure for clarity. Colour codes for the crystal structure: Grey = Dy and black = C. (b) Magnetic hysteresis loops measured on the polycrystalline solid samples of **72** with dc field sweep rate = 39 Oe/s. The inset is the magnified hysteresis loop at 60 K. (c) Energy landscapes of the ground J manifold for the Dy (III) ion in **72**. The path defined by the solid dark-grey arrows stands for the magnetization relaxation via Orbach process. Figure and captions are reprinted from the Ref. [67] with permission from John Wiley and Sons.

barriers for these complexes, implying the presence of QTM. To investigate magnetic behaviour of these complexes further, detailed *ab initio* calculations were performed. The representative energy landscapes of the ground J manifolds for **68** and **69** are presented in Fig. 59. Because of the intrinsic ionic magnetic anisotropy characteristics, the ground eigen-doublets associate with $M_J = \pm 9/2$ for **68** and $M_J = \pm 15/2$ for **69**. Moreover, the eigen-doublets are energetically more closely spaced for the former. The energy gaps between the ground and first excited doublets are calculated to be 19 and 180.6 cm^{-1} for **68** and **69**, respectively. The probability for QTM in ground doublet is found to be around five-orders of magnitude higher for the former. For **69**, both the ground and first excited doublets are almost uniaxial ($g_{xx,yy} = 3.5 \times 10^{-6}$ and $g_{zz} = 17.96$ for the ground doublet; and $g_{xx,yy} = 5.4 \times 10^{-4}$ and $g_{zz} = 115.53$ for the first excited doublet) and the easy-axes of magnetizations are projected along the symmetry axis (Fig. 58) [71]. On the other hand, for **68**, the first excited doublet is magnetically more axial ($g_{xx,yy} = 5.8 \times 10^{-2}$ and $g_{zz} = 13.84$) than the ground doublet ($g_{xx,yy} = 1.6 \times 10^{-1}$ and $g_{zz} = 12.64$). The angle between the easy-axes of magnetization (g_{zz}) = 21° for 64 (Fig. 58).

A similar set of conclusions were also arrived by some of us by doing *ab initio* calculations on **67**, **69** and $[Er(COT)Cp^*]^-$ [115]. In both **67** and **69**, relaxation takes place via second excited state, whereas in $\{Er(COT)Cp^*\}^-$ relaxation occurs through the first excited state. The ground state KD is found to be Ising in nature in all these complexes. In the ground and first excited state QTM probabilities are found to be very small in **67** and **69**, causing relaxation via the second excited state. However, for $[Er(COT)Cp^*]^-$, QTM probability at first excited state is significant causing relaxation via first excited state.

However, more efficient SIM behaviour for **69** in comparison to **67** can be attributed to the substituent's on the capping ligands in the latter, which influence both the CF strength and symmetry. Strong influence of the cycloalkenyl anionic capping ligands on the efficiency of Er(III)-based SIMs can be further realized from the magnetic behaviour of the complex $[K_2Er_2(COT)_4(THF)_4]$ (**70**) (Fig. 60) [24]. As the paramagnetic Er(III) centres are intervened by the diamagnetic K ions (or in other words, **70** can be regarded as the association of **69** *via* K^+ bridges through COT ligands), the magnetic behaviour of **70** can be considered as single-ionic. **70** reverts its magnetization under zero field with a high effective energy barrier $U_{eff} = 212.6\ cm^{-1}$, similar to its symmetrized monomeric analogue **69**. But, the blocking temperature is found to be markedly higher ($T_B = 12$ K with 18 Oe/s sweep rate) for the former. Such significant influence stems from the symmetric coordination of K^+ with the capping COT ligands, which enhances the axial CF strength. Though polynuclear complexes are out of the scope of this review article, it is quite interesting to note the structural and magnetic properties of the binuclear complex $[KEr_2(\eta^7\text{-}C_7H_7)(N(SiMe_3)_2)_4]$ (**71**), where two $Er(SiMe_3)_2$ moieties are bridged by η^7-cycloheptatrieneyl trianion ($\eta^7\text{-}C_7H_7^{3-}$) (Fig. 60 (c)). **71** is found to be an SMM ($U_{eff} = 40.3\ cm^{-1}$ under H_{dc} = 800Oe, fitting the data above 3 K temperature) [24]. Below 3 K, **71** display two relaxations, where the *out-of-phase* ac susceptibility maxima for the 2nd relaxation go below 2 K. In comparison to the Er(III)-based cycloalkenyl sandwich complexes, poor magnetic slow dynamics in **71** can be attributed to low CF symmetry, non-axial CF strength and direct mixing of *4f*-orbitals of the intramolecular Er(III) ions. The Er-Er distance in **71** is relatively shorter (3.96 Å) and the Er(III) centres indulge in weak anti-ferromagnetic exchange coupling ($J = -0.134\ cm^{-1}$). However, such complexes are extremely rare in Ln(III) chemistry. Observation of slow dynamics of magnetization in such complexes implies the versatility of Er(III) ion in exhibiting magnetization blocking over a wide range of coordination environments.

In the preceding section, we have indicated that COT-sandwich or COT-Cp mixed sandwich Dy(III) complexes do not bring the highest possible magnetic states ($M_J = \pm 15/2$). In addition to that, the easy-axes of magnetization for the ground doublets are not necessarily uniaxial under such CF environments. In order to access limiting U_{eff} involving the Dy^{III} ion, extremely strong axial ligand field with concomitant high axial CF symmetry is mandatory [21]. However, as discussed in Section 2.9.1 above, *ab initio* calculations predict that stabilization of Dy^{III} ion with two capping

Cp* ligands in a tilted fashion could endow the system with the potential of exhibiting the essential limit of effective energy barrier for magnetization reversal (Fig. 51). But the greatest challenge to stabilize such complexes seems to be to prevent additional coordinating ligand(s) because such complexes are extremely prone to form pseudo-sandwich complexes. One possible way could be to introduce large bulky substituents on the periphery of the capping ligands. Layfield et al. [67] and Mills et al. [68] have employed an interesting synthetic strategy to stabilize such a complex, $[(Cp^{ttt})_2Dy][B(C_6F_5)_4]$ (**72**) (where Cp^{ttt} = 1,2,4-tri(*tert*butyl)-cyclopentadienyl anion, Fig. 61) [67]. Single crystal X-ray structural analysis revealed that the two capping Cp^{ttt} ligands are arranged in a staggered fashion to sandwich the Dy^{III} ion. The centroid (Cp^{ttt})-Dy-centroid(Cp^{ttt}) angle is found to be 152.8°, which is far more towards linearity compared to the hypothetical $[(Cp^*)_2\text{-}Dy]^+$model complex (centroid(Cp*)-Dy-centroid(Cp*) angle = 136°; Fig. 61) [217]. Considering the characteristic oblate electrostatic potential surface of the highest magnetic *Ising*-doublet for the Dy^{III} ion ($M_J = \pm 15/2$), the ligand environment in **72** is expected to exert stronger axial CF and thereby promoting larger effective energy barrier for magnetization reversal with reduced QTM. Dc magnetic susceptibility studies on the polycrystalline sample of **72** indeed indicated the stabilization of the highest magnetic states as the ground doublet. Ac magnetic susceptibility investigations revealed a high SIM-performance for **72** with zero-field $U_{eff} = 1277\ cm^{-1}$, $\tau_0 = 8.12 \times 10^{-12}$ s, and T_B = 60 K at dc field sweep rate = 39 Oe/s [67].

The presence of very weak steps near zero-field in the magnetic hysteresis loops (Fig. 61 (b)) implies that the CF in **72** has suppressed QTM significantly. Notably, the slow relaxation of magnetisation in **72** is observed up to around 100 K. The Orbach process is found to occur only at higher temperature domain (T > 60 K). Due to very high energy barrier, the Orbach process at lower temperature domain is too slow to measure. The relaxation of magnetization at low temperature domain appears to be dominated by Raman process. However, the Raman process is quite inefficient and hence, it is possible to detect the slow relaxation magnetization up to such a high temperature.

Ab initio calculations resulted out *Ising*-type energy landscapes for the ground *J* manifold of Dy(III) ion in **72** (Fig. 61 (c)). Detailed analysis revealed that the most probable path for the magnetization reversal takes place *via* transition through the fifth excited doublet which is situated at 1156 cm^{-1} above the ground doublet. Slightly lower predicted energy than the experimentally evaluated one could be attributed to the simplifications in CASSCF calculations [67]. However, the discovery of the complex **72** is indeed a step forward towards the applications of molecular nanomagnets in the advanced technology. It raises hopes that employment of appropriate cycloalkenyl capping ligands could bring forth potential organometallic Ln(III)-based molecular nanomagnets with promising SMM behaviour.

3. Conclusion and outlook

In view of slow magnetic dynamics, low-coordinate high-symmetric lanthanide complexes are more promising candidates for being investigated as molecular magnets compared to lanthanide complexes with *normal* coordination numbers or in comparison to transition metal-based complexes. QTM, which diminishes or sometimes nullifies the effective energy barrier for magnetization reversal and magnetic hysteresis loops, is an inherent characteristic of lanthanide-based molecular complexes. Crystal-field and point group symmetry consideration could help chemists to design appropriate complexes with significantly suppressed QTM. In spite of the progress made thus far it is clear that rigorous theoretical calculations are required to forecast promising molecular systems that are worth trying experimentally, although promising leads in this direction has already been made.

One of the issues that need to be resolved in this rapidly growing area of molecular magnets is the identification of a common parameter(s) that can be used as a bench mark for validating and evaluating a given system. Because of the variations in reporting the data it becomes difficult to compare, very quickly, the relative pros and cons of various molecular magnets that have been reported. Keeping in mind the requisites of the molecule-based nanomagnets for their applications in practical devices, blocking temperature (T_B) measured under specific experimental conditions could be a potential parameter for uniform assessment of the molecule-based magnets.

Another important challenge is the finding a way to control non-Orbach mechanism in this class of compounds. QTM has been the most important factor that undercut the blocking temperature significantly in this area and over the decades of effort has lead to several significant progresses to quench QTM effects. This includes designing ligands with appropriate symmetry, incorporation of paramagnetic ions/radicals to enhance exchange coupling which quench the QTM effects, controlling intermolecular interactions using bulky counter anions/ligands, utilizing enriched lanthanides to avoid hyperfine couplings *etc*. However other relaxation mechanisms such as spin-phonon are still dominant at higher temperatures leading to faster relaxation mechanism. Although some theoretical efforts already have been made in this regard, rigorous way to control relaxation via all channels is extremely important to take the T_B beyond liquid nitrogen temperatures.

To summarize, among non-molecular low-coordinate systems, doping appropriate lanthanide atoms on non-magnetic surfaces (where the lanthanide atoms can be associated with high CF symmetry and very weak electronic interactions with the surfaces) could result in systems with excellent magnetization blocking temperatures. Lanthanide cluster/ion encapsulated fullerenes are found to provide low coordination around Ln(III) ions. High symmetry and rigidity of these EMFs can help to enhance barrier height and control possibly also other relaxation channels. Although, experimentally still to be realized, based on theoretical calculations, linear bi-coordinate Dy(III) complexes are expected to exhibit the extremely high effective energy barrier for magnetization reversal. Lanthanide complexes with perfectly planar coordination geometry and high point group symmetry are also expected to be promising molecular magnets. Here again, such ideal geometry has been found difficult to realize experimentally. Among, the six-coordinate complexes, oblate lanthanide ions involved in trigonal prism and trigonally distorted octahedron geometries are promising candidates. Similarly, in hepta-coordinate complexes, possessing oblate lanthanide ions in a D_{5h} CF point group symmetry are also good systems that exhibit high effective energy barrier for magnetization reversal. If the ring sizes of the sandwich complexes are chosen aptly, this can lead to a significant breakthrough as has been witnessed with a blocking temperature of 60 K. Thus hierarchical Ln(III)-based sandwich complexes are proving to exhibit efficient slow dynamics of magnetization. However one of the main issues with such systems is the stability under ambient conditions as desired in the next logical step of fabricating devices from these molecules. It is clear that chemists can play a major role in realizing systems that proved elusive thus far by invoking new design paradigms.

In Table 10, we have summarized suitable geometry for prolate and oblate ions as reported in the literature along with maximum value of experimental/theoretical effective energy barrier and blocking temperature achieved till date. This can be utilized to fine tune particular geometry or target particular systems already possessing desired magnetic properties.

Table 10
Various possible Ln(III) SMMs reported in the literature are clubbed based on their coordination number/geometry along with the maximum $U_{eff}/U_{cal}/T_B$ reported within that coordination number. Along with this, suitability of such coordination number/geometry for prolate and oblate ions are given in squares in three different colours (Green -best, Orange -moderate and red-poor). Here green, orange and red indicate best, moderate and poor match between the geometry/coordination number with the nature of electron density.

		Prolate (Er)	Oblate (Dy)	$(U_{eff}/U_{cal})_{max}$ cm^{-1}	$(T_B)_{max}$ K
Ln(III) doped on surface		🟥	🟩		30
Ln(III) ion inside fullerenes		🟥	🟩		18
$\{Ln\text{-}X\}^{3-a}$		🟥	🟩	2100#	
{Ln-X}@EMF/Surface		🟥	🟩		
$\{X\text{-}Ln\text{-}X\}^{3-2a}$		🟥	🟩	3000#	
Trigonal planar		🟩	🟥	85	1.9
Trigonal pyramidal	LnX_4	🟩	🟥		
	LnE_wA_s	🟥	🟩		
	LnE_sA_w	🟩	🟥	55.8	3
Square planar		🟩	🟥	390#	
Tetrahedral				19#	
Square pyramidal	LnX_5	🟩	🟥	157#	
	LnE_wA_s	🟥	🟩	535.7	5
	LnE_sA_w	🟩	🟥		
Trigonal bipyramidal	LnX_5	🟥	🟩		475#
	LnE_wA_s	🟥	🟩	535.7	5
	LnE_sA_w	🟩	🟥		
Octahedral	LnX_6	🟥	🟥	0#	
	LnE_wA_s	🟥	🟩	828	20
	LnE_sA_w	🟩	🟥		22^F
Pentagonal bipyramidal	LnX_7	🟩	🟥		166#
	LnE_wA_s	🟥	🟩	1043	11
	LnE_sA_w	🟩	🟥		
$\{Ln(COT)_2\}^-$		🟩	🟥	224.5	12
$[Ln(COT)Cp^*\}^{1-}$		🟩	🟧	419	5
$[Ln(Cp^*)_2[^-$		🟥	🟩	1277	60

a = formal charge on the anion X, here X is OH^-, O^{2-} and F^- *etc.*
E = Equatorial ligand, A = Axial ligand, s = strong, w = weak, F = field applied, # = U_{cal}.

Acknowledgments

VC is thankful to the Department of Science and Technology, New Delhi, India, for a National J. C. Bose Fellowship. AKB and PK are thankful to the National Institute of Science Education and Research, Bhubaneswar, India for post-doctoral and doctoral fellowships respectively. GR is thankful to INSA, SERB (EMR/2014/000247) and MKS is thankful to UGC India for fellowship.

References

[1] A. Caneschi, D. Gatteschi, R. Sessoli, A.L. Barra, L.C. Brunel, M. Guillot, J. Am. Chem. Soc. 113 (1991) 5873–5874.
[2] R. Sessoli, D. Gatteschi, A. Caneschi, M.A. Novak, Nature 365 (1993) 141–143.
[3] G. Christou, D. Gatteschi, D.N. Hendrickson, R. Sessoli, MRS Bull. 25 (2000) 66–71.
[4] G. Aromí, E.K. Brechin, R.E.P. Winpenny, Single-Molecule Magnets and Related Phenomena, Structure and Bonding, Springer-Verlag Berlin Heidelberg, 2006.
[5] C.B. Dante Gatteschi, Introduction to Molecular Magnetism: From Transition Metals to Lanthanides, Wiley-VCH, 2015.
[6] S. Gao, Molecular Nanomagnets and Related Phenomena, Structure and Bonding, Springer-Verlag Berlin Heidelberg, 2015.
[7] D. Gatteschi, R. Sessoli, J. Villain, Molecular Nanomagnets and Related Phenomena, Mesoscopic Physics and Nanotechnology, 2006.
[8] J.-C. Chambron, C.O. Dietrich-Buchecker, O. Kahn (Eds.), Magnetism: A Supramolecular Function, NATO ASI Series, vol. 484, Springer Netherlands, 1996.
[9] O. Kahn, Molecular Magnetism, Willey VCH, 1993.
[10] R.A. Layfield, M. Murugesu, Lanthanides and Actinides in Molecular Magnetism, Wiley VCH, 2015.
[11] J.S. Miller, Chem. Soc. Rev. 40 (2011) 3266–3296.
[12] F. Palacio, D. Gatteschi, O. Kahn, J.S. Miller, F. Palacio, Magnetic Molecular Materials NATO ASI Series, Springer Netherlands, 1991, Vol. 198.
[13] N.A. Spaldin, Magnetic Materials: Fundamentals and Applications, 2nd. ed., Caambridge Uiniversity Press, 1969.
[14] J. Tejada, J. Bartolomé, F. Luis, J.F. Fernández, Molecular Magnets: Physics and Applications Nano Science and Technology, Springer-Verlag Berlin Heidelberg, 2014.
[15] R.D. Willett, E. Coronado, P. Delhaès, D. Gatteschi, J.S. Miller, Molecular Magnetism-From Molecular Assemblies to the Devices, NATO ASI Series, 1995, Vol. 321.
[16] R.E. Winpenny, Molecular Cluster Magnets, World Scientific Series in Nanoscience and Nanotechnology, 2011.
[17] R. Skomski, Simple Models of Magnetism, Oxford University Press, Oxford, U. K., 2008.
[18] O. Waldmann, Inorg. Chem. 46 (2007) 10035–10037.
[19] M. Fittipaldi, L. Sorace, A.L. Barra, C. Sangregorio, R. Sessoli, D. Gatteschi, Phys. Chem. Chem. Phys. 11 (2009) 6555–6568.
[20] H. Wang, B.-W. Wang, Y. Bian, S. Gao, J. Jiang, Coord. Chem. Rev. 306 (2016) 195–216.
[21] L. Ungur, L.F. Chibotaru, Inorg. Chem. 55 (2016) 10043–10056.
[22] K. Liu, X. Zhang, X. Meng, W. Shi, P. Cheng, A.K. Powell, Chem. Soc. Rev. 45 (2016) 2423–2439.
[23] K. Katoh, T. Komeda, M. Yamashita, Chem. Rec. 16 (2016) 987–1016.
[24] K.L. Harriman, M. Murugesu, Acc. Chem. Res. 49 (2016) 1158–1167.
[25] P. Zhang, L. Zhang, J. Tang, Dalton Trans. 44 (2015) 3923–3929.
[26] S.T. Liddle, J. van Slageren, Chem. Soc. Rev. 44 (2015) 6655–6669.
[27] S. Gómez-Coca, D. Aravena, R. Morales, E. Ruiz, Coord. Chem. Rev. 289–290 (2015) 379–392.
[28] J. Dreiser, J. Phys. Condens. Matter. 27 (2015) 183203–183223.
[29] R.A. Layfield, Organometallics 33 (2014) 1084–1099.
[30] P. Zhang, Y.-N. Guo, J. Tang, Coord. Chem. Rev. 257 (2013) 1728–1763.
[31] D.N. Woodruff, R.E. Winpenny, R.A. Layfield, Chem. Rev. 113 (2013) 5110–5148.
[32] L. Sorace, C. Benelli, D. Gatteschi, Chem. Soc. Rev. 40 (2011) 3092–3104.
[33] J.D. Rinehart, J.R. Long, Chem. Sci. 2 (2011) 2078–2085.

[34] F. Hulliger, M. Landolt, H. Vetsch, J. Solid State Chem. 18 (1976) 283–291.
[35] B.-Q. Ma, S. Gao, G. Su, G.-X. Xu, Angew. Chem. Int. Ed. Engl. 40 (2001) 434–437.
[36] N. Ishikawa, M. Sugita, T. Ishikawa, S.Y. Koshihara, Y. Kaizu, J. Am. Chem. Soc. 125 (2003) 8694–8695.
[37] N.F. Chilton, Inorg. Chem. 54 (2015) 2097–2099.
[38] N.F. Chilton, C.A.P. Goodwin, D.P. Mills, R.E.P. Winpenny, Chem. Commun. 51 (2015) 101–103.
[39] Y.-S. Meng, S.-D. Jiang, B.-W. Wang, S. Gao, Acc. Chem. Res. 49 (2016) 2381–2389.
[40] C. Huang, Z. Bian (Eds.), Rare Earth Coordination Chemistry: Fundamentals and Applications, John, Wiley & Sons (Asia) Pte Ltd, 2010.
[41] S.A. Cotton, J.M. Harrowfield, Encyclopedia of Inorganic and Bioinorganic Chemistry, John Wiley & Sons, Ltd, 2011.
[42] S.A. Cotton, C. R. Chim. 8 (2005) 129–145.
[43] T. Moeller, Werner Centennial, AMERICAN CHEMICAL SOCIETY, 1967, pp. 306–317.
[44] N.J. Yutronkie, I.A. Kuhne, I. Korobkov, J.L. Brusso, M. Murugesu, Chem. Commun. 52 (2016) 677–680.
[45] K.S. Pedersen, A.M. Ariciu, S. McAdams, H. Weihe, J. Bendix, F. Tuna, S. Piligkos, J. Am. Chem. Soc. 138 (2016) 5801–5804.
[46] J. Liu, Y.C. Chen, J.H. Jia, J.L. Liu, V. Vieru, L. Ungur, L.F. Chibotaru, Y. Lan, W. Wernsdorfer, S. Gao, X.M. Chen, M.L. Tong, J. Am. Chem. Soc. 138 (2016) 5441–5450.
[47] S.K. Gupta, T. Rajeshkumar, G. Rajaraman, R. Murugavel, Chem. Commun. 52 (2016) 7168–7171.
[48] Y.C. Chen, J.L. Liu, L. Ungur, J. Liu, Q.W. Li, L.F. Wang, Z.P. Ni, L.F. Chibotaru, X. M. Chen, M.L. Tong, J. Am. Chem. Soc. 138 (2016) 2829–2837.
[49] P. Zhang, L. Zhang, C. Wang, S. Xue, S.Y. Lin, J. Tang, J. Am. Chem. Soc. 136 (2014) 4484–4487.
[50] E. Lucaccini, L. Sorace, M. Perfetti, J.-P. Costes, R. Sessoli, Chem. Commun. 50 (2014) 1648–1651.
[51] T. Miyamachi, T. Schuh, T. Markl, C. Bresch, T. Balashov, A. Stohr, C. Karlewski, S. Andre, M. Marthaler, M. Hoffmann, M. Geilhufe, S. Ostanin, W. Hergert, I. Mertig, G. Schon, A. Ernst, W. Wulfhekel, Nature 503 (2013) 242–246.
[52] A.J. Brown, D. Pinkowicz, M.R. Saber, K.R. Dunbar, Angew. Chem. Int. Ed. Engl. 54 (2015) 5864–58648.
[53] J.D. Rinehart, M. Fang, W.J. Evans, J.R. Long, J. Am. Chem. Soc. 133 (2011) 14236–14239.
[54] J.-L. Liu, Y.-C. Chen, Y.-Z. Zheng, W.-Q. Lin, L. Ungur, W. Wernsdorfer, L.F. Chibotaru, M.-L. Tong, Chem. Sci. 4 (2013) 3310–3316.
[55] M. Gregson, N.F. Chilton, A.-M. Ariciu, F. Tuna, I.F. Crowe, W. Lewis, A.J. Blake, D. Collison, E.J.L. McInnes, R.E.P. Winpenny, S.T. Liddle, Chem. Sci. 7 (2016) 155–165.
[56] R.J. Blagg, L. Ungur, F. Tuna, J. Speak, P. Comar, D. Collison, W. Wernsdorfer, E. J. McInnes, L.F. Chibotaru, R.E. Winpenny, Nat. Chem. 5 (2013) 673–678.
[57] A. Caneschi, D. Gatteschi, N. Lalioti, C. Sangregorio, R. Sessoli, G. Venturi, A. Vindigni, A. Rettori, M.G. Pini, M.A. Novak, Angew. Chem. Int. Ed. Engl. 40 (2001) 1760–1763.
[58] H. Miyasaka, M. Yamashita, Dalton Trans. (2007) 399–406.
[59] W.-X. Zhang, R. Ishikawa, B. Breedlove, M. Yamashita, RSC Adv. 3 (2013) 3772–3798.
[60] S. Dhers, H.L.C. Feltham, S. Brooker, Coord. Chem. Rev. 296 (2015) 24–44.
[61] A.K. Bar, C. Pichon, J.-P. Sutter, Coord. Chem. Rev. 308 (2016) 346–380, and the references therein.
[62] W.H.H.D.E. Freedman, T.D. Harris, G.J. Long, C.J. Chang, J.R. Long, J. Am. Chem. Soc. 132 (2010) 1224–1225.
[63] X.N. Yao, J.Z. Du, Y.Q. Zhang, X.B. Leng, M.W. Yang, S.D. Jiang, Z.X. Wang, Z.W. Ouyang, L. Deng, B.W. Wang, S. Gao, J. Am. Chem. Soc. 139 (2017) 373–380.
[64] J.M. Zadrozny, D.J. Xiao, M. Atanasov, G.J. Long, F. Grandjean, F. Neese, J.R. Long, Nat. Chem. 5 (2013) 577–581.
[65] C.J. Milios, A. Vinslava, W. Wernsdorfer, S. Moggach, S. Parsons, S.P. Perlepes, G. Christou, E.K. Brechin, J. Am. Chem. Soc. 129 (2007) 2754–2755.
[66] N.E. Chakov, S.-C. Lee, A.G. Harter, P.L. Kuhns, A.P. Reyes, S.O. Hill, N.S. Dalal, W. Wernsdorfer, K.A. Abboud, G. Christou, J. Am. Chem. Soc. 128 (2006) 6975–6989.
[67] F.-S. Guo, B. Day, Y.-C. Chen, M.-L. Tong, A. Mansikamäkki, R.A. Layfield, Angew. Chem. Int. Ed. Engl. 56 (2017) 11445–11449.
[68] C.A.P. Goodwin, F. Ortu, D. Reta, N.F. Chilton, D.P. Mills, Nature 548 (2017) 439–442.
[69] Y.-S. Ding, N.F. Chilton, R.E.P. Winpenny, Y.-Z. Zheng, Angew. Chem. Int. Ed. Engl. 55 (2016) 16071–16074.
[70] C.R. Ganivet, B. Ballesteros, G. de la Torre, J.M. Clemente-Juan, E. Coronado, T. Torres, Chemistry 19 (2013) 1457–1465.
[71] L. Ungur, J.J. Le Roy, I. Korobkov, M. Murugesu, L.F. Chibotaru, Angew. Chem. Int. Ed. Engl. 53 (2014) 4413–4417.
[72] R.J. Blagg, C.A. Muryn, E.J. McInnes, F. Tuna, R.E. Winpenny, Angew. Chem. Int. Ed. Eng. 50 (2011) 6530–6533.
[73] P.-H. Lin, T.J. Burchell, L. Ungur, L.F. Chibotaru, W. Wernsdorfer, M. Murugesu, Angew. Chem. Int. Ed. Engl. 48 (2009) 9489–9492.
[74] J.L. Liu, J.Y. Wu, Y.C. Chen, V. Mereacre, A.K. Powell, L. Ungur, L.F. Chibotaru, X. M. Chen, M.L. Tong, Angew. Chem. Int. Ed. Engl. 53 (2014) 12966–12970.
[75] Hinckley, J. Am. Chem. Soc. 91 (1969) 5150–5155.
[76] S. Rondeau, J. Am. Chem. Soc. 93 (1971) 1522–1524.
[77] R.L. Dutta, A. Syamal, Elements of Magnetochemistry, 2nd ed., EWP Pvt. Ltd., New Delhi, 2009, p. 16.
[78] Y.C. Chen, J.L. Liu, W. Wernsdorfer, D. Liu, L.F. Chibotaru, X.M. Chen, M.L. Tong, Angew. Chem. Int. Ed. Engl. 56 (2017) 4996–5000.
[79] Y. Kishi, F. Pointillart, B. Lefeuvre, F. Riobe, B. Le Guennic, S. Golhen, O. Cador, O. Maury, H. Fujiwara, L. Ouahab, Chem. Commun. 53 (2017) 3575–3578.
[80] F. Luis, M.J. Martínez-Pérez, O. Montero, E. Coronado, S. Cardona-Serra, C. Martí-Gastaldo, J.M. Clemente-Juan, J. Sesé, D. Drung, T. Schurig, Phys. Rev. B 82 (2010) 060403–060407.
[81] E. Moreno-Pineda, M. Damjanović, O. Fuhr, W. Wernsdorfer, M. Ruben, Angew. Chem. Int. Ed. Engl. 56 (2017) 9915–9919.
[82] F. Pointillart, K. Bernot, S. Golhen, B. Le Guennic, T. Guizouarn, L. Ouahab, O. Cador, Angew. Chem. Int. Ed. Engl. 54 (2015) 1504–1507.
[83] H. Bethe, Ann. Phys. B 395 (1929) 133–208.
[84] K.W.H. Stevens, Proc. Phys. Soc. London, Sect. A 65 (1952) 209–215.
[85] B.G. Wybourne, Spectroscopic Properties of Rare Earths, John Wiley & Sons, Inc., New York, 1965.
[86] G.S. Ofelt, J. Chem. Phys. 37 (1962) 511–520.
[87] B.R. Judd, Phys. Rev. 127 (1962) 750–761.
[88] A. Abragam, B. Bleaney, Electron Paramagnetic Resonance of Transition Ions, Clarendon Press, Oxford, 1970.
[89] S.A. Altshuler, B.M. Kozyrev, Electron Paramagnetic Resonance in Compounds of Transition Elements, 2nd ed., John Wiley & Sons, Inc., New York, 1974.
[90] C. Rudowicz, C.Y. Chung, J. Phys. Condens. Matter 16 (2004) 1–23.
[91] J.J. Baldoví, S. Cardona-Serra, J.M. Clemente-Juan, E. Coronado, A. Gaita-Ariño, A. Palii, Inorg. Chem. 51 (2012) 12565–12574.
[92] M.A. AlDamen, S. Cardona-Serra, J.M. Clemente-Juan, E. Coronado, A. Gaita-ArinÞo, C. Martiì-Gastaldo, F. Luis, O. Montero, Inorg. Chem. 48 (2009) 3467–3679.
[93] N. Ishikawa, M. Sugita, T. Okubo, N. Tanaka, T. Iino, Y. Kaizu, Inorg. Chem. 42 (2003) 2440–2446.
[94] S.-D. Jiang, S.-X. Qin, Inorg. Chem. Front. 2 (2015) 613–619.
[95] D.J. Newman, B. Ng, Crystal Field Handbook, Cambridge University Press, Cambridge, 2000.
[96] E. Bauer, M. Rotter, Magnetism of Complex Metallic Alloys: Crystalline Electric Field Effects Properties and Applications of Complex Intermetallics Book Series on Complex Metallic Alloys, World Scientific, Singapore, 2009, pp. 183–248.
[97] C.E. Schäffer, C.K. Jørgensen, Mol. Phys. 9 (1965) 401–412.
[98] W. Urland, Chem. Phys. 14 (1976) 393–401.
[99] W. Urland, Chem. Phys. Lett. 46 (1977) 457–460.
[100] A. Abragam, B. Bleaney, Electron Paramagnetic Resonance of Transition Ions Oxford Classic Texts in the Physical Sciences, Oxford University Press, Oxford, 1970.
[101] A. Furrer, Int. J. Mod. Phys. B 24 (2010) 3653–3691.
[102] A. Furrer, O. Waldmann, Rev. Mod. Phys. 85 (2013) 367–420.
[103] I. Bertini, C. Luchinat, G. Parigi, Prog. Nucl. Magn. Reson. Spectrosc. 40 (2002) 249–273.
[104] B.J. Bleaney, Magn. Reson. (1972) 91–100.
[105] J.A. Peters, J. Huskens, D.J. Raber, Prog. Nucl. Magn. Reson. Spectrosc. 28 (1996) 283–350.
[106] E. Terazzi, J.-P. Rivera, N. Ouali, C. Piguet, Magn. Reson. Chem. 44 (2006) 539–552.
[107] T. Funk, A. Deb, S.J. George, H. Wang, S.P. Cramer, Coord. Chem. Rev. 249 (2005) 3–30.
[108] J. Stöhr, J. Magn. Magn. Mater. 200 (1999) 470–497.
[109] G. Van der Laan, A.I. Figueroa, Coord. Chem. Rev. 277–278 (2014) 95–129.
[110] M.P. Hehlen, H.U. Güdel, J. Chem. Phys. 98 (1993) 1768–1775.
[111] W. Urland, R. Kremer, Inorg. Chem. 23 (1984) 1550–1553.
[112] W. Urland, R. Kremer, A. Furrer, Chem. Phys. Lett. 132 (1986) 113–115.
[113] M.-E. Boulon, G. Cucinotta, J. Luzon, C. Degl'Innocenti, M. Perfetti, K. Bernot, G. Calvez, A. Caneschi, R. Sessoli, Angew. Chem. Int. Ed. Engl. 52 (2013) 350–354.
[114] L.F. Chibotaru, L. Ungur, A. Soncini, Angew. Chem. Int. Ed. Engl. 120 (2008) 4194–4197.
[115] S.K. Singh, T. Gupta, G. Rajaraman, Inorg. Chem. 53 (2014) 10835–10845.
[116] H. Schilder, H. Lueken, J. Magn. Magn. Mater. 281 (2004) 17–26.
[117] M. Speldrich, H. Schilder, H. Lueken, P.A. Kögerler, Isr. J. Chem. 51 (2011) 215–227.
[118] J. Van Leusen, M. Speldrich, H. Schilder, P.A. Kögerler, Coord. Chem. Rev. 289–290 (2015) 137–148.
[119] J.J. Baldovi, J.M. Clemente-Juan, E. Coronado, A. Gaita-Arino, Inorg. Chem. 53 (2014) 11323–11327.
[120] N.F. Chilton, D. Collison, E.J. McInnes, R.E. Winpenny, A. Soncini, Nat. Commun. 4 (2013) 2551.
[121] J.J. Baldoví, J.M. Clemente-Juan, E. Coronado, A. Gaita-Ariño, A. Palii, J. Comput. Chem. 35 (2014) 1930–1934.
[122] J.J. Baldovi, J.J. Borras-Almenar, J.M. Clemente-Juan, E. Coronado, A. Gaita-Arino, Dalton Trans. 41 (2012) 13705–13710.
[123] J.J. Baldoví, S. Cardona-Serra, J.M. Clemente-Juan, E. Coronado, A. Gaita-Ariño, A. Palii, J. Comput. Chem. 34 (2013) 1961–1967.
[124] J.J. Baldovi, S. Cardona-Serra, J.M. Clemente-Juan, E. Coronado, A. Gaita-Arino, A. Palii, Inorg. Chem. 51 (2012) 12565–12574.
[125] N. Ishikawa, M. Sugita, T. Ishikawa, S.-Y. Koshihara, Y. Kaizu, J. Phys. Chem. B 108 (2004) 11265–11271.
[126] E. Lucaccini, M. Briganti, M. Perfetti, L. Vendier, J.P. Costes, F. Totti, R. Sessoli, L. Sorace, Chem. Eur. J. 22 (2016) 5552–5562.
[127] Y.-C. Chen, J.-L. Liu, L. Ungur, J. Liu, Q.-W. Li, L.-F. Wang, Z.-P. Ni, L.F. Chibotaru, X.-M. Chen, M.-L. Tong, J. Am. Chem. Soc. (2016).

[128] K.R. Meihaus, J.R. Long, J. Am. Chem. Soc. 135 (2013) 17952–17957.
[129] D. Gatteschi, R. Sessoli, Angew. Chem. Int. Ed. 42 (2003) 268–297.
[130] J.R. Friedman, M.P. Sarachik, Annu. Rev. Condens. Matter Phys. 1 (2010) 109–128.
[131] A.K. Bar, C. Pichon, N. Gogoi, C. Duhayon, S. Ramasesha, J.-P. Sutter, Chem. Commun. 51 (2015) 3616–3619.
[132] A. Amjad, A.M. Madalan, M. Andruh, A. Caneschi, L. Sorace, Chem. Eur. J. 22 (2016) 12849–12858.
[133] R. Orbach, Proc. R. Soc. A 264 (1961) 458–484.
[134] R. Orbach, Proc. Phys. Soc. 77 (1961) 821.
[135] C.B.P. Finn, R. Orbach, W.P. Wolf, Proc. Phys. Soc. 77 (1961) 261.
[136] A. Fetoh, G. Cosquer, M. Morimoto, M. Irie, O. El-Gammal, G. Abu El-Reash, B. K. Breedlove, M. Yamashita, Sci. Rep. 6 (2016) 23785.
[137] R.W. Bierig, M.J. Weber, S.I. Warshaw, Phys. Rev. 134 (1964) A1504–A1516.
[138] R. Orbach, M. Blume, Phys. Rev. Lett. 8 (1962) 478–480.
[139] M. Walker, Can. J. Phys. 46 (1968) 1347–1353.
[140] S. Loth, M. Etzkorn, C.P. Lutz, D.M. Eigler, A.J. Heinrich, Science 329 (2010) 1628–1630.
[141] P. Gambardella, S. Rusponi, M. Veronese, S.S. Dhesi, C. Grazioli, A. Dallmeyer, I. Cabria, R. Zeller, P.H. Dederichs, K. Kern, C. Carbone, H. Brune, Science 300 (2003) 1130–1133.
[142] T. Balashov, T. Schuh, A.F. Takács, A. Ernst, S. Ostanin, J. Henk, I. Mertig, P. Bruno, T. Miyamachi, S. Suga, W. Wulfhekel, Phys. Rev. Lett. 102 (2009) 257203.
[143] A.A. Khajetoorians, S. Lounis, B. Chilian, A.T. Costa, L. Zhou, D.L. Mills, J. Wiebe, R. Wiesendanger, Phys. Rev. Lett. 106 (2011) 037205.
[144] M. Richter, P. Oppeneer, H. Eschrig, B. Johansson, Phys. Rev. B 46 (1992) 13919–13927.
[145] F. Donati, S. Rusponi, S. Stepanow, C. Wäckerlin, A. Singha, L. Persichetti, R. Baltic, K. Diller, F. Patthey, E. Fernandes, J. Dreiser, Ž. Šljivančanin, K. Kummer, C. Nistor, P. Gambardella, H. Brune, Science 352 (2016) 318–321.
[146] F.D. Natterer, K. Yang, W. Paul, P. Willke, T. Choi, T. Greber, A.J. Heinrich, C.P. Lutz, Nature 543 (2017) 226–228.
[147] F. Donati, A. Singha, S. Stepanow, C. Wackerlin, J. Dreiser, P. Gambardella, S. Rusponi, H. Brune, Phys. Rev. Lett. 113 (2014) 237201.
[148] R. Baltic, M. Pivetta, F. Donati, C. Wackerlin, A. Singha, J. Dreiser, S. Rusponi, H. Brune, Nano Lett. 16 (2016) 7610–7615.
[149] F. Allouche, G. Lapadula, G. Siddiqi, W.W. Lukens, O. Maury, B. Le Guennic, F. Pointillart, J. Dreiser, V. Mougel, O. Cador, C. Copéret, ACS Cent. Sci. 3 (2017) 244–249.
[150] F. Bondino, C. Cepek, N. Tagmatarchis, M. Prato, H. Shinohara, A. Goldoni, J. Phys. Chem. B 110 (2006) 7289–7295.
[151] C. De Nadaï, A. Mirone, S.S. Dhesi, P. Bencok, N.B. Brookes, I. Marenne, P. Rudolf, N. Tagmatarchis, H. Shinohara, T.J.S. Dennis, Phys. Rev. B 69 (2004) 184421.
[152] R. Kitaura, H. Okimoto, H. Shinohara, T. Nakamura, H. Osawa, Phys. Rev. B 76 (2007) 172409.
[153] M.K. Singh, N. Yadav, G. Rajaraman, Chem. Commun. 51 (2015) 17732–17735.
[154] F. Liu, D.S. Krylov, L. Spree, S.M. Avdoshenko, N.A. Samoylova, M. Rosenkranz, A. Kostanyan, T. Greber, A.U.B. Wolter, B. Buchner, A.A. Popov, Nat. Commun. 8 (2017) 16098–16107.
[155] Y.N. Guo, L. Ungur, G.E. Granroth, A.K. Powell, C. Wu, S.E. Nagler, J. Tang, L.F. Chibotaru, D. Cui, Sci. Rep. 4 (2014) 5471.
[156] J. Dreiser, G.E. Pacchioni, F. Donati, L. Gragnaniello, A. Cavallin, K.S. Pedersen, J. Bendix, B. Delley, M. Pivetta, S. Rusponi, H. Brune, ACS nano 10 (2016) 2887–2892.
[157] E. Lucaccini, J.J. Baldovi, L. Chelazzi, A.L. Barra, F. Grepioni, J.P. Costes, L. Sorace, Inorg. Chem. 56 (2017) 4728–4738.
[158] Y. Dong, P. Yan, X. Zou, T. Liu, G. Li, J. Mater. Chem. C 3 (2015) 4407–4415.
[159] L. Ungur, L.F. Chibotaru, Phys. Chem. Chem. Phys. 13 (2011) 20086–20090.
[160] P.E. Kazin, M.A. Zykin, V.V. Utochnikova, O.V. Magdysyuk, A.V. Vasiliev, Y.V. Zubavichus, W. Schnelle, C. Felser, M. Jansen, Angew. Chem. Int. Ed. Engl. 56 (2017) 13416–13420.
[161] A.K. Bar, P. Kalita, J.-P. Sutter, V. Chandrasekhar, Inorg. Chem. 57 (2018) 2398–2401.
[162] B.M. Flanagan, P.V. Bernhardt, E.R. Krausz, S.R. Lüthi, M.J. Riley, Inorg. Chem. 41 (2002) 5024–5033.
[163] K.S. Pedersen, J. Dreiser, H. Weihe, R. Sibille, H.V. Johannesen, M.A. Sorensen, B.E. Nielsen, M. Sigrist, H. Mutka, S. Rols, J. Bendix, S. Piligkos, Inorg. Chem. (2015).
[164] J.-L. Liu, K. Yuan, J.-D. Leng, L. Ungur, W. Wernsdorfer, F.-S. Guo, L.F. Chibotaru, M.-L. Tong, Inorg. Chem. 51 (2012) 8538–8544.
[165] S.K. Singh, M.F. Beg, G. Rajaraman, Chem. Eur. J. 22 (2016) 672–680.
[166] J.-P. Costes, L. Vendier, W. Wernsdorfer, Dalton Trans. 39 (2010) 4886–4892.
[167] M.X. Yao, Z.X. Zhu, X.Y. Lu, X.W. Deng, S. Jing, Dalton Trans. 45 (2016) 10689–10695.
[168] W.A. Herrmann, R. Anwander, F.C. Munck, W. Scherer, V. Dufaud, N.W. Huberb, G.R.J. Artus, Z. Naturforsch 49b (1994) 1789–1797.
[169] H. Schumann, D.M.M. Freckmann, S. Schutte, S. Dechert, M. Hummert, Z. Anorg, Allg. Chem. 633 (2007) 888–892.
[170] H.W. Görlitzer, M. Spiegler, R. Anwander, Eur. J. Inorg. Chem. 1998 (1998) 1009–1014.
[171] W.J. Evans, M.A. Ansari, J.W. Ziller, S.I. Khan, Inorg. Chem. 35 (1996) 5435–5444.
[172] Z. Hou, A. Fujita, Y. Zhang, T. Miyano, H. Yamazaki, Y. Wakatsuki, J. Am. Chem. Soc. 120 (1998) 754–766.
[173] G. Lapadula, M.P. Conley, C. Copéret, R.A. Andersen, Organometallics 34 (2015) 2271–2277.
[174] H. Schumann, D.M.M. Freckmann, S. Dechert, Z. Anorg. Allg. Chem. 628 (2002) 2422–2426.
[175] G.W. Rabe, C.D. Bérubé, G.P.A. Yap, K.-C. Lam, T.E. Concolino, A.L. Rheingold, Inorg. Chem. 41 (2002) 1446–1453.
[176] J. Zou, D.J. Berg, D. Stuart, R. McDonald, B. Twamley, Organometallics 30 (2011) 4958–4967.
[177] S.A. Schuetz, V.W. Day, R.D. Sommer, A.L. Rheingold, J.A. Belot, Inorg. Chem. 40 (2001) 5292–5295.
[178] S.A. Schuetz, C.M. Silvernail, C.D. Incarvito, A.L. Rheingold, J.L. Clark, V.W. Day, J.A. Belot, Inorg. Chem. 43 (2004) 6203–6214.
[179] R. Litlabø, K. Saliu, M.J. Ferguson, R. McDonald, J. Takats, R. Anwander, Organometallics 28 (2009) 6750–6754.
[180] F. Yuan, J. Yang, L. Xiong, J. Organomet. Chem. 691 (2006) 2534–2539.
[181] C. Liu, Q. Qian, K. Nie, Y. Wang, Q. Shen, D. Yuan, Y. Yao, Dalton Trans. 43 (2014) 8355–8362.
[182] I. Aillaud, C. Olier, Y. Chapurina, J. Collin, E. Schulz, R. Guillot, J. Hannedouche, A. Trifonov, Organometallics 30 (2011) 3378–3385.
[183] G. Qi, Y. Nitto, A. Saiki, T. Tomohiro, Y. Nakayama, H. Yasuda, Tetrahedron 59 (2003) 10409–10418.
[184] J. Xiong, H.-Y. Ding, Y.-S. Meng, C. Gao, X.-J. Zhang, Z.-S. Meng, Y.-Q. Zhang, W. Shi, B.-W. Wang, S. Gao, Chem. Sci. 8 (2017) 1288–1294.
[185] S.K. Singh, T. Gupta, M. Shanmugam, G. Rajaraman, Chem. Commun. 50 (2014) 15513–15516.
[186] K.L.M. Harriman, J.L. Brosmer, L. Ungur, P.L. Diaconescu, M. Murugesu, J. Am. Chem. Soc. (2017) 1420–1423.
[187] R.A. Andersen, D.H. Templeton, A. Zalkin, Inorg. Chem. 17 (1978) 2317–2319.
[188] A.G. Avent, P.B. Hitchcock, A.V. Khvostov, M.F. Lappert, A.V. Protchenko, Dalton Trans. (2003) 1070–1075.
[189] K.R.D. Johnson, A.P. Côté, P.G. Hayes, J. Organomet. Chem. 695 (2010) 2747–2755.
[190] M. Morissette, S. Haufe, R. McDonald, G.M. Ferrence, J. Takats, Polyhedron 23 (2004) 263–271.
[191] D. Heitmann, C. Jones, D.P. Mills, A. Stasch, Dalton Trans. 39 (2010) 1877–1882.
[192] W.J. Evans, D.K. Drummond, H. Zhang, J.L. Atwood, Inorg. Chem. 27 (1988) 575–579.
[193] T.D. Tilley, R.A. Andersen, A. Zalkin, J. Am. Chem. Soc. 104 (1982) 3725–3727.
[194] Q. Wu, J. Zhou, Z. Yao, F. Xu, Q. Shen, J. Org. Chem. 75 (2010) 7498–7501.
[195] S.-L. Zhou, S.-W. Wang, G.-S. Yang, X.-Y. Liu, E.-H. Sheng, K.-H. Zhang, L. Cheng, Z.-X. Huang, Polyhedron 22 (2003) 1019–1024.
[196] P. Zhang, J. Jung, L. Zhang, J. Tang, B. Le Guennic, Inorg. Chem. 55 (2016) 1905–1911.
[197] K. Katoh, T. Komeda, M. Yamashita, Dalton Trans. 39 (2010) 4708–4723.
[198] J. Kondo, Prog. Theor. Phys. 32 (1964) 37–49.
[199] J.R. Schrieffer, P.A. Wolff, Phys. Rev. 149 (1966) 491–492.
[200] S.K. Singh, B. Pandey, G. Velmurugan, G. Rajaraman, Dalton Trans. 46 (2017) 11913–11924.
[201] J.S. Ghotram, M.B. Hursthouse, A.J. Welch, J. Chem. Soc. Chem. Comm (1973) 669–670.
[202] E.D. Brady, D.L. Clark, J.C. Gordon, P.J. Hay, D.W. Keogh, R. Poli, B.L. Scott, J.G. Watkin, Inorg. Chem. 42 (2003) 6682–6690.
[203] M. Niemeyer, Inorg. Chem. 45 (2006) 9085–9095.
[204] S.O. Hauber, M. Niemeyer, Chem. Commun. (2007) 275–277.
[205] K.R. Meihaus, J.D. Rinehart, J.R. Long, Inorg. Chem. 50 (2011) 8484–8489.
[206] K.S. Pedersen, L. Ungur, M. Sigrist, A. Sundt, M. Schau-Magnussen, V. Vieru, H. Mutka, S. Rols, H. Weihe, O. Waldmann, L.F. Chibotaru, J. Bendix, J. Dreiser, Chem. Sci. 5 (2014) 1650–1660.
[207] C.A.P. Goodwin, N.F. Chilton, G.F. Vettese, E.M. Pineda, I.F. Crowe, J.W. Ziller, R.E.P. Winpenny, W.J. Evans, D.P. Mills, Inorg. Chem. 55 (2016) 10057–10067.
[208] C. Eaborn, P.B. Hitchcock, K. Izod, J.D. Smith, J. Am. Chem. Soc. 116 (1994) 12071–12072.
[209] C. Eaborn, P.B. Hitchcock, K. Izod, Z.-R. Lu, J.D. Smith, Organometallics 15 (1996) 4783–4790.
[210] S.K. Gupta, T. Rajeshkumar, G. Rajaraman, R. Murugavel, Chem. Sci. 7 (2016) 5181–5191.
[211] N. Kulikov, L.A. Kaledin, A.I. Kobyliansky, L.V. Gurvich, Can. J. Phys. 62 (1984) 1855–1870.
[212] C. Linton, D.M. Gaudet, H. Schall, J. Mol. Spectrosc. 115 (1986) 58–73.
[213] Y.C. Liu, C. Linton, H. Schall, R.W. Field, J. Mol. Spectrosc. 104 (1984) 72–88.
[214] T. Gupta, G. Velmurugan, T. Rajeshkumar, G. Rajaraman, J. Chem. Sci. 128 (2016) 1615–1630.
[215] M.K. Singh, G. Rajaraman, Chem. Commun. 52 (2016) 14047–14050.
[216] C.-H. Chen, D.S. Krylov, Stanislav M. Avdoshenko, F. Liu, L. Spree, R. Yadav, A. Alvertis, L. Hozoi, K. Nenkov, A. Kostanyan, T. Greber, A.U.B. Wolter, A.A. Popov, Chem. Sci. 8 (2017) 6451–6465.
[217] Y.S. Meng, Y.Q. Zhang, Z.M. Wang, B.W. Wang, S. Gao, Chem. Eur. J. 22 (2016) 12724–12731.
[218] J. Maynadié, J.-C. Berthet, P. Thuéry, M. Ephritikhine, Organometallics 26 (2007) 2623–2629.
[219] J.C. Berthet, P. Thuery, M. Ephritikhine, Dalton Trans. 44 (2015) 7727–7742.
[220] W.J. Evans, C.A. Seibel, J.W. Ziller, J. Am. Chem. Soc. 120 (1998) 6745–6752.
[221] T. Pugh, V. Vieru, L.F. Chibotaru, R.A. Layfield, Chem. Sci. (2016) 2128–2137.
[222] T. Pugh, F. Tuna, L. Ungur, D. Collison, E.J. McInnes, L.F. Chibotaru, R.A. Layfield, Nat. Commun. 6 (2015) 7492–7500.

[223] K.R. Meihaus, M.E. Fieser, J.F. Corbey, W.J. Evans, J.R. Long, J. Am. Chem. Soc. 137 (2015) 9855–9860.

[224] Y.S. Meng, Y.S. Qiao, Y.Q. Zhang, S.D. Jiang, Z.S. Meng, B.W. Wang, Z.M. Wang, S. Gao, Chem. Eur. J. 22 (2016) 4704–4708.

[225] A.A. Trifonov, B. Shestakov, J. Long, K. Lyssenko, Y. Guari, J. Larionova, Inorg. Chem. 54 (2015) 7667–7669.

[226] S.-S. Liu, J.W. Ziller, Y.-Q. Zhang, B.-W. Wang, W.J. Evans, S. Gao, Chem. Commun. 50 (2014) 11418–11420.

[227] S.-D. Jiang, S.-S. Liu, L.-N. Zhou, B.-W. Wang, Z.-M. Wang, S. Gao, Inorg. Chem. 51 (2012) 3079–3087.

[228] S.D. Jiang, B.W. Wang, H.L. Sun, Z.M. Wang, S. Gao, J. Am. Chem. Soc. 133 (2011) 4730–4733.

[229] M. Jeletic, P.H. Lin, J.J. Le Roy, I. Korobkov, S.I. Gorelsky, M. Murugesu, J. Am. Chem. Soc. 133 (2011) 19286–19289.

[230] J.J. Le Roy, M. Jeletic, S.I. Gorelsky, I. Korobkov, L. Ungur, L.F. Chibotaru, M. Murugesu, J. Am. Chem. Soc. 135 (2013) 3502–3510.

[231] J. Kan, H. Wang, W. Sun, W. Cao, J. Tao, J. Jiang, Inorg. Chem. 52 (2013) 8505–8510.

[232] J. Rausch, C. Apostolidis, O. Walter, V. Lorenz, C.G. Hrib, L. Hilfert, M. Kuhling, S. Busse, F.T. Edelmann, New J. Chem. 39 (2015) 7656–7666.

[233] F. Gao, M.X. Yao, Y.Y. Li, Y.Z. Li, Y. Song, J.L. Zuo, Inorg. Chem. 52 (2013) 6407–6416.

[234] M.-E. Boulon, G. Cucinotta, S.-S. Liu, S.-D. Jiang, L. Ungur, L.F. Chibotaru, S. Gao, R. Sessoli, Chem. Eur. J. 19 (2013) 13726–13731.

[235] M. Perfetti, G. Cucinotta, M.-E. Boulon, F. El Hallak, S. Gao, R. Sessoli, Chem. Eur. J. 20 (2014) 14051–14056.

[236] H.L. Feltham, Y. Lan, F. Klower, L. Ungur, L.F. Chibotaru, A.K. Powell, S. Brooker, Chem. Eur. J. 17 (2011) 4362–4365.